

Ice-ocean coupled computations for the sea ice prediction to support ice navigation in the Arctic Ocean

(北極海での氷中航行支援のための海氷変動予測を目指した海氷／海洋連成計算)

By

De Silva, Liyanarachchi Waruna Arampath

ディシルワー リヤナアラッチ ワルナ アランパツ

A Dissertation

Submitted to the Department of Systems Innovation the Graduate School of
Engineering

The University of Tokyo

In partial fulfillment of the requirements for the degree of

DOCTOR OF ENGINEERING

The University of Tokyo

June 2013

Acknowledgements

First and foremost, I owe my deepest gratitude to Professor Hajime Yamaguchi for being a great and very understanding supervisor for me and this thesis would not have been possible unless his guidance, support and encouragements. Dear Sir, it is an honor for being your student and I am very grateful to you for your warmth assistance which lifted my spirit to go on and finish what I have started.

Also I am glad to show my heartiest gratitude to Dr. Ayumi Fujisaki, her guidance and support enabled me to deepen my understanding on the subject of sea ice. She has made available her support as a well understanding friend in a number of ways to make me successful in my research.

I would like to thank, Dr. Jun Ono, Dr. Eiji Watanabe and Dr. Noriaki Kimura for their tremendous comments for my research studies and sharing their experience and knowledge with me. Those highly influenced me to accomplish my targets.

I am indebted to my laboratory friends, your existence and being a part of you make me feel that I am not alone, although I am far away from home. Also I should thank for your supports for me to face no difficulties of my stay in Japan with my less Japanese knowledge.

Secondly, I would like to express my heartiest thanks for my wife and my son for being the shadow of my life in Japan and to my loving family in Sri Lanka; my father, mother and my sister. Their never ending love, care, support and encouragements make me feel better although they are not here with me.

Finally, my special thanks to the Ministry of Education, Culture, Sports, Science and Technology for providing the financial support for my education, without your support my dream of being a graduate student of The University of Tokyo would have never been fulfilled.

Abstract

Summer sea ice in the Arctic ocean retreating further away from most Arctic landmasses, opening new shipping routes and extending the navigation season in the Arctic Sea Routes (ASR). The passages through the Arctic Ocean are the shortest sea route from North American and European harbors to Southeast Asian harbors. However to navigate in the Arctic prediction of sea ice condition is crucial, especially in marginal sea ice zones. Many numerical models have been used to predict the overall Arctic sea ice conditions successfully. However, the model results have shown high uncertainties in the marginal ice zones. Therefore accurate prediction method for marginal sea ice condition is an urgent need for cruising Arctic sea routes. In this study we have used the high-resolution ice-ocean coupled model with explicitly treating the ice floe collision using ice collision rheology to predict the sea ice condition in marginal ice zones for 1-2 weeks. The configured ice ocean coupled model, ocean part is based on Princeton Ocean Model (POM), while the ice part consist of full thermodynamic and dynamic model, which employs the elastic viscous plastic rheology and also takes account of ice floe collision. First numerical issues accosted with collision rheology in the ice-POM model was discussed and resolved. Then whole Arctic Ocean annual and seasonal sea ice variability and reproducibility limitations of the ice-POM coarser resolution (about 25km) model were discussed. It was found that coarser resolution model reproducibility of seasonal and interannual variations are reasonable with observations but cannot be used to predict the short-term variation like 1-2 weeks. Therefore secondly, the high-resolution (about 2.5km) regional models were setup along the Northeastern Passage of the Arctic sea routes to investigate the short-term sea ice predictions. High-resolution computation was able to predict sea ice extents very reasonably with observations due to the improved expression of the ice-albedo feedback process and reproducibility of meso-scale eddies in the ocean.

Table of Contents

1. Introduction	1
2. Ice-ocean coupled model.....	6
2.1. Ocean model	7
2.1.1. Primitive equations	8
2.1.2. Ice-ocean coupling and boundary conditions	11
2.2. Ice model.....	14
2.2.1. Momentum equation.....	14
2.2.2. Rheological modeling.....	15
2.2.3. Tracer advection	18
2.3. Thermodynamic model	19
2.3.1. Surface heat flux calculation	19
2.3.2. Vertical formation of sea ice.....	22
2.3.3. Lateral growth and melt of sea ice.....	26
3. Numerical issues associated with ice-POM model	28
3.1. Numerical instability in a high resolution ice-pom model.....	28
3.1.1. Instability explained by an one-dimensional test setup	29
3.1.2. Remedies for instability issue	33
3.2. Effect of implicit correction in ice-POM model	37
4. Whole Arctic model simulation	40
4.1. Comparison of sea ice concentration and extent reproducibility with satellite derived observations	42
4.2. Comparison of sea ice thickness between model computations and observations	45
4.3. Sea ice drift variability in the Arctic Ocean model and observation	51
4.4. Evaluation of fresh water distribution in the Arctic Ocean	58
5. Simulation BY high-resolution regional models	61
5.1. Sea ice extents and concentrations comparison with observations.....	63
5.2. Sensitivity of ice-ocean coupling in high-resolution modeling	76
5.3. Sensitivity study of ice collision rheology	79
6. General conclusions and future works	84
7. References	88

List of Tables

Table 2-1 Constants used in ice-ocean coupled model.....	6
Table 2-2 Vertical sigma levels	8

List of Figures

Figure 1-1 Northern hemisphere sea ice extent in August 1979-2012 (extracted from the National Snow and Ice Data Center; http://nsidc.org)	1
Figure 1-2 Arctic sea routes and conventional routes (a) The solid lines indicate possible connections of Northern Europe and Southeast Asia via the Northeast Passage (approx. 7000nm) and Northwest Passage (approx. 7600nm). The dash-dotted line shows the conventional track through the Mediterranean, the Gulf of Suez, and the Indian Ocean (approx. 11100nm). (b) The solid line indicates possible connection of Northern America and Southeast Asia via the Northwest Passage (approx. 7000nm). The dash-dotted line shows the conventional track through the Pacific Ocean (approx. 10000nm).	2
Figure 2-1 Ice strength as a function of ice concentration and strain rate parameter Δ . (a) Hibler's formulation, (b) Sagawa's formulation (reproduced from Sagawa 2007).....	17
Figure 2-2 Schematic diagram of the energy fluxes at the snow free sea ice.....	23
Figure 2-3 Schematic diagram of the energy fluxes at the snow covered sea ice	25
Figure 3-1 Simulated sea ice thickness [m] and sea ice velocity field [m/s] near the New Siberian Islands.	28
Figure 3-2 Schematic diagram of one dimensional test setup	30
Figure 3-3 Ice strength as a function of ice concentration and strain rate parameter Δ . Old formulation.....	31
Figure 3-4 Ice strength as a function of ice concentration and strain rate parameter Δ . New formulation	34
Figure 3-5 Schematic diagram of two-dimensional test setup.....	35
Figure 3-6 Sea ice thickness [m] and associated ice velocity [m/s] variation in two-dimensional test model. (a-d) left-hand side shows the old formulation of ice-POM model ice variation 1 st week to 4 th week. (e-h) right hand side shows the new formulation of ice-POM model ice variation in the same time duration	36

Figure 3-7 Sea ice concentration on 2000-August-01 (a) old explicit time integral formulation (b) new implicit correction formulation (c) satellite derived SSM/I observational	38
Figure 3-8 Meridional sea ice velocity (v) and sea ice velocity vector on 2000-August-01 (a) old explicit time integral formulation (b) new implicit correction formulation (c) satellite derived Pathfinder observational	39
Figure 4-1 Whole arctic model bathymetry in meters	40
Figure 4-2 Daily time series of model and satellite observation ice extent from year 2001 to 2012.....	42
Figure 4-3 September mean sea ice concentration from year 2002 to 2007. (a) HadISST observational concentration. (b) Numerical model predicted concentration.....	44
Figure 4-4 Observed ice draft locations Lindsay (2010) from year 2001 to 2011	45
Figure 4-5 Inter-annual and seasonal comparisons between observed Lindsay (2010) mean ice draft and computed model ice draft in all four seasons; Winter (JFM), Spring (AMJ), Summer (JAS), Fall (OND) of year 2001-2011.	46
Figure 4-6 Overall comparisons between observed mean ice draft Lindsay (2010) and computed mean ice draft in all four seasons Winter (JFM), Spring (AMJ), Summer (JAS), Fall (OND) of year 2001-2011.....	47
Figure 4-7 Mean 2003-2008 (a,b) ICESat and (c,d) Model thickness for February-March (a,c) and October-November (b,d). (e,f) Differences of thickness maps are shown. The scale is given in [m].	50
Figure 4-8 Seasonal histograms (a) January – March, (b) April – June, (c) July -September, and (d) October–December of sea ice drift speed of the Arctic for the period 2004–2010. Corresponding distribution of observation drift speed computed from daily AMSR-E satellite products and IABP program have been included. Bin width is 1cms^{-1} . Bin start from 0.5cms^{-1}	52

Figure 4-9 Some of the IABP buoy trajectories from 2004 January 01 to 2004 December 31. Yellow arrows show the buoy trajectories that used in scatterplots comparison.....	54
Figure 4-10 Comparison of drifting buoy motion and model derived ice motion. Left figures show scatterplot of zonal (U) velocity component and right side shows the meridional (V) component of velocities. The black line denotes the linear fit of data set	57
Figure 4-11 Liquid freshwater content 2001-2012 in summer (JAS).....	59
Figure 4-12 Average liquid freshwater content from 2006-2008 (JAS) (a) observational data from Rabe et al. (2011) (b) model derived	60
Figure 5-1 Model bathymetries. (a) Whole Arctic model and red rectangles denote the corresponding high resolution domains (b) high resolution regional model consist of part of East Siberian sea Kara sea and Laptev sea (LS) (c) high resolution regional model consisting of part of east Siberian sea and Chukchi sea (CS).....	62
Figure 5-2 Comparison of sea ice extents between coarse grid computation (Whole Arctic model), fine grid regional computation (LS) and satellite observation (AMSR-E) (a) during 2004-Jul-20 to 2004-Aug-17 (b) during 2005-Jul-20 to 2005-Aug-17. Area covered with more than 15% ice concentration is taken into comparison.....	64
Figure 5-3 Comparison of sea ice extents between coarse grid computation (Whole Arctic model), fine grid regional computation (CS) and satellite observation (AMSR-E) (a) during 2004-Jul-20 to 2004-Aug-17 (b) during 2005-Jul-20 to 2005-Aug-17. Area covered with more than 15% ice concentration is taken into comparison.....	65
Figure 5-4 Sea ice concentration distribution from 2004-Jul-20 to 2004-Aug-17; upper figures have shown the model derived concentration and lower figures have shown the satellite observation AMSR-E sea ice concentration in the LS region	66
Figure 5-5 Snapshots of ocean surface temperature in LS region on 2004-Aug-03. Color bar denotes the sea ice temperate [$^{\circ}\text{C}$] and black contour denotes the 15% sea ice concentration.....	67

Figure 5-6 Snapshots of ice-eddy interaction: 2005-Oct-01. Color bar denotes the sea ice concentration and vectors denote the surface ocean current, location-North of Sevelnaya Zemlya Islands. (a) Whole arctic coarser grid model (b) High-resolution regional model.....	68
Figure 5-7 Energy conversion rates from (a) MKE T_{bt} and (b) APE T_{bc} to EKE in August and September. Root mean square value is shown in the bottom of each figure. Vectors denote the surface ocean current average in the top 100m, Average ice edge location (at 15% concentration) shown in black contour, Region North of Sevelnaya Zemlya Islands.	69
Figure 5-8 Comparison of sea ice extents between coarse grid computation (Whole Arctic model), fine grid regional computation (LS) and satellite observation (AMSR-E) (a) during 2004-Jul-20 to 2004-Nov-23 (b) during 2005-Jul-20 to 2005-Nov-23. Area covered with more than 15% ice concentration is taken into comparison.....	71
Figure 5-9 Comparison of sea ice extents between coarse grid computation (Whole Arctic model), fine grid regional computation (CS) and satellite observation (AMSR-E) (a) during 2004-Jul-20 to 2004-Nov-23 (b) during 2005-Jul-20 to 2005-Nov-23. Area covered with more than 15% ice concentration is taken into comparison.....	72
Figure 5-10 A schematic diagram of process near river mouth (fall and winter), strong stratification and suppression of convective mixing under the ice cover	73
Figure 5-11 Snapshots of sea ice concentration and vertical salinity profile across the Lena River mouth (A-B) in LS region: 2004-Nov-12. (a) Satellite observation AMSR-E concentration, (b) Model derived sea ice concentration, (c) PHC3.0 observational vertical salinity profile under the line A-B and (d) Model derived vertical salinity profile under the line A-B.	74
Figure 5-12 Schematic diagrams of (a) ice-ocean coupled model (fully ice and ocean dynamics are included) (b) uncoupled model (ocean variables are given to the ice model as a boundary conditions).....	76

Figure 5-13 Comparison of sea ice extents between finer grid ice-ocean coupled model, fine grid uncoupled and satellite observation (AMSR-E) during 2005-Jul-20 to 2005-Aug-17. Area covered with more than 10% ice concentration is taken into comparison.....	77
Figure 5-14 Sea ice concentration distribution from 2004-Jul-20 to 2004-Aug-17; upper figures have shown the ice-ocean coupled model derived concentrations, middle figures have shown the satellite observation AMSR-E sea ice concentration and lower figures have shown the uncoupled model sea ice concentrations in the region of LS.....	78
Figure 5-15 Comparison of regional model (area LS) derived sea ice extent with and without collision rheology. Area covered with more than 15% concentration is taken into comparison.	80
Figure 5-16 Comparison of regional model (area LS) derived sea ice area with and without collision rheology. Area covered with more than 15% concentration is taken into comparison.....	80
Figure 5-17 Upper figures show sea ice concentration, middle figures sea ice thickness [m], lower figures sea ice strength in logarithmic scale [N/m ²] (a) with ice collision rheology (b) without ice collision rheology and (c) difference between with and without collision rheology. All variables are average over the period of 2004-Oct-01 to 2004-Oct-07	81
Figure 5-18 Strain rate parameter Δ in the ice collision rheology and wind velocity. All variables are averaged over the period of 2004-Oct-01 to 2004-Oct-07	82
Figure 5-19 Satellite observation (MODIS) sea surface temperature distribution at South of Sevelnaya Zemlya Islands on 2004-Oct-01	83

1. INTRODUCTION

Satellite observations have shown the rapid decrease of sea ice in the Arctic Ocean Figure 1-1. Many evidence and hypothesis are given to explain the dramatic reductions in recent years. Some researchers have claimed that increase of wind stress field and atmospheric warming Köberle and Gerdes (2003); Rothrock (2005); Stroeve (2005), ice-albedo and ice-cloud feedback processes Ikeda et al. (2003); Curry et al. (1995) and intensification of Arctic Dipole Mode (ADM) as the second EOF(Empirical Orthogonal Function) of sea level pressure with dipoles over Siberia and Canada at opposite signs Ikeda (2009) enhance the recent decrease of sea ice in the Arctic Ocean. Changes of wind stress directly influence the sea ice circulation and could increase the sea ice export from the Arctic Ocean to the Greenland Sea due to the strong meridionality. On the other hand changes of wind stress and wind pattern enhance the upward heat flux from ocean surface due to the upwelling and increase the further melt of sea ice in the Arctic costal regions Watanabe (2013).

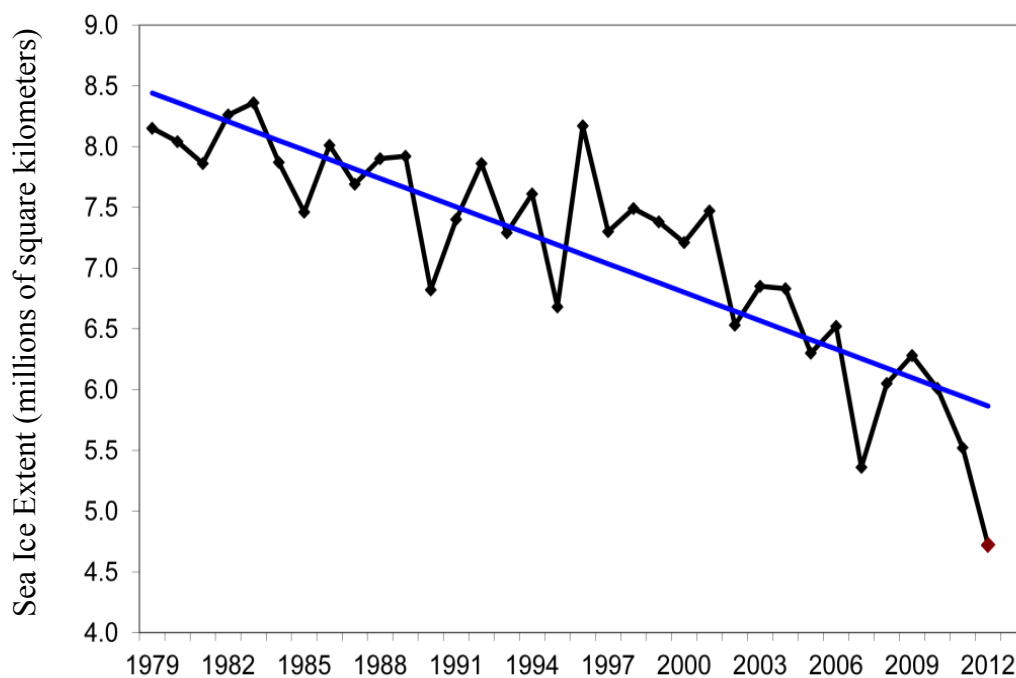
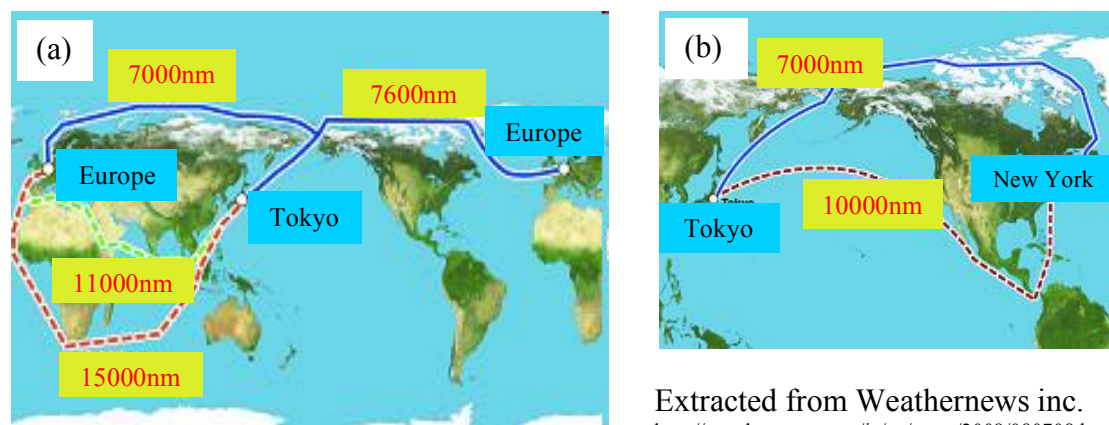


Figure 1-1 Northern hemisphere sea ice extent in August 1979-2012 (extracted from the National Snow and Ice Data Center; <http://nsidc.org>)

Some researchers have claimed that increase of heat transport from the Pacific Ocean to the Arctic Ocean through Bering Strait Shimada et al. (2006) and increase of Atlantic Ocean heat transport to the Arctic Ocean Steele et al. (2008); Zhang et al. (1998) also enhanced the ice melting in recent years.

However, retreat of summer sea ice in the Arctic Ocean attracts the interest of exploring the Arctic areas. Such as natural resource exploitation and commercial shipment through the Arctic sea routes (abbreviated as ASR hereafter). ASR consists of two main paths, the Northeastern Passage called the Northern Sea Route (NSR) and the Northwestern Passage. The Northeastern Passage connects the Bering Strait and Kara Strait along the Russian Federation coastline as shown in Figure 1-2 (a). On the other hand, the Northwestern Passage lies through the Alaskan coastline, Canadian archipelago and Baffin Bay (Figure 1-2 (b)).



Extracted from Weathernews inc.
<http://weathernews.com/ja/nc/press/2008/080708.html>

Figure 1-2 Arctic sea routes and conventional routes (a) The solid lines indicate possible connections of Northern Europe and Southeast Asia via the Northeast Passage (approx. 7000nm) and Northwest Passage (approx. 7600nm). The dash-dotted line shows the conventional track through the Mediterranean, the Gulf of Suez, and the Indian Ocean (approx. 11100nm). (b) The solid line indicates possible connection of Northern America and Southeast Asia via the Northwest Passage (approx. 7000nm). The dash-dotted line shows the conventional track through the Pacific Ocean (approx. 10000nm).

As shown in Figure 1-2 the Southeast Asia can be connected to the Northern Europe and the North American continent via ASRs. The solid line has denoted the ASR travel distance and dash dotted line has shown the conventional southern routes. According to the surveys, Arctic sea routes can shorten the travel distance 40% from

the existing southern sea routes. The existence of two routes instead of the one sole southern route will represent the tremendous boost to the security of international shipping. Therefore ASRs are considered to be efficient, economical, and safe passages for transportation.

First time of the history, collaboration research between Japan, Norway, and Russia advanced the International Northern Sea Route Programme (INSROP) to examine the possibilities of utilizing the NSR as an international commercial sea route from 1993 to 1999 Kitagawa et al. (2001). INSROP has abled to develop and demonstrate the technical, ecological, environmental, economic, political, and strategic aspects of NSR. But unfortunately INSROP project has not focused on developing a rigorous sea ice prediction method along the NSR; instead sea ice prediction was depending on the simple numerical predictions and satellite information.

However, monitoring of Arctic sea ice is important for managing offshore activities and utilizing ASRs. In ice-covered areas detecting sea ice conditions is needed to protect ships and minimize the damages to coastal facilities. There are three kinds of sea ice predictions needed for safe navigation in ASRs called long-term, medium-term, and short-term. The long-term (about 20-30 year predictions) predictions are useful to make decisions like new ice breaker vessel constructions and new port constructions (long-term planning). Medium-term predictions (about 3-6months) are useful to make the decision of utilizing the paths of ASRs or conventional southern sea routes in coming summer seasons. And finally, short-term predictions (about 1-2 weeks) are useful to understand the sea ice condition and to choose the safest and shortest path in the Arctic Ocean once the ship enters the ice covered areas.

Numerical modeling of sea ice has become one of the important instruments for ice monitoring, understanding past conditions and explaining recently observed changes and future predictions in the Arctic Ocean. In early days, Arctic Ice Dynamics Joint Experiment (AIDEX) project advanced the understanding and modeling of sea ice dynamics Coon et al. (1974); Hibler (1979); Hopkins et al. (1991); Lu et al. (1989). And later, since 2001, the International Arctic Ocean Model Inter comparison Project (AOMIP) has focused on improving Arctic regional models and investigated many aspects of the Arctic Ocean structure and sea ice changes Holloway et al. (2007). However in general, most AOMIP numerical model results are not very comparable

with observations. For an example AOMIP models underestimate the amount of ice thicker than 2m (or thick ice ($>2\text{m}$)) and overestimate the amount of ice thinner than 2m (or thin ice ($<2\text{m}$)) Proshutinsky et al. (2011) in the Arctic Oceans. Most of these early researchers have focused on simulating large-scale sea ice dynamics with coarser resolution models. Most previous studies e.g., Shen et al. (1986); Leppäranta and Hibler III (1985); Lu et al. (1989); Sagawa (2007) have focused on the meso-scale sea ice dynamics. On the other hand, some researchers focused on reproducing and understanding of Arctic Ocean structures. Wang et al. (2005) evaluated the seasonal cycle of Pan-Arctic and North-Atlantic Ocean using a coupled ice-ocean model with a 27.5km resolution. Watanabe and Hasumi (2009) evaluated the Pacific water transport across the Beaufort shelf break using an eddy-resolving coupled sea ice-ocean model, whose horizontal resolution is about 2.5km.

However, there was no any workable model, which is capable of resolving both meso and large-scale sea ice dynamics in the Arctic Ocean. Applications like prediction of Arctic sea routes need a compromise model to resolve the complex small scale and large-scale sea ice dynamics together. Almost all-existing sea ice forecast models are based on the continuum approach in ice dynamic processes. On scale much larger than floe size, continuum approximation is commonly assumed. Advantages of the continuum model are simplicity, low computational cost, and good description of large-scale sea-ice behavior. However, when dealing with an ice prediction in small regions, which consist of sea ice margin such as the ASRs, it is not realistic to treat sea ice extent as a continuum body because the sea ice consists of discrete ice floes. Therefore, a model that takes account of the ice discrete characteristics is needed for higher resolution forecasting. In this situation, we introduce the floe collision rheology of Sagawa (2007) into the conventional elastic-viscous-plastic rheology of Hunke (2001). To further minimize the sea ice diffusion and improve the accuracy of ice edge locations, we incorporate the subgrid-scale ice motion (Lagrangian movements) into the sea ice dynamics to minimize the sea ice diffusion and to improve the accuracy of ice edge locations. Therefore in this study we aim to predict the short-term sea ice condition in Arctic sea routes using modified sea ice dynamics, meso-scale eddy resolving high-resolution ice-ocean coupled model.

The thesis is organized as follows: First, Brief descriptions of the basics of the numerical methods used in the ice-ocean coupled model are given in Chapter 2. Numerical difficulties in the old version of coupled ice-ocean model and modifications and improved set-up are introduced in Chapter 3. Then, reproducibility and interannual variations of large-scale sea ice dynamics and ocean structures are evaluated by using a medium-resolution (about 25km) model, which covers the entire Arctic Ocean and the northern part of Atlantic Ocean, in Chapter 4. Then, detailed processes of the large scale and meso-scale sea ice dynamics are clarified by using an eddy-resolving high-resolution (about 2.5km) regional model in Chapter 5. In Chapter 5 also discussed the sensitivity of ice collision rheology and importance of ice ocean interaction in high-resolution regional models. Finally, general conclusion and future works are presented in Chapter 6.

2. ICE-OCEAN COUPLED MODEL

The numerical model (ice-POM) developed in this study is based on a three dimensional high-resolution regional model on the Sea of Okhotsk Fujisaki et al. (2010) in which ocean part is based on general coordinate version of the Princeton Ocean Model (POM) Mellor et al. (2002). In subsections of chapter 2 ocean, sea ice and thermodynamic parts of ice-POM model are described in details. The model variables, constants, and namelist parameters used in ice-POM model are summarized in Table 2-1.

Please note that throughout this paper subscript a , i , s , and w denote atmosphere, sea ice, snow, and seawater respectively.

Table 2-1 Constants used in ice-ocean coupled model

Symbol	Description	Values	Units
C	compaction hardening	20	
C_{Dai}	air to ice drag coefficient	1.2×10^{-3}	
C_{Dwi}	water to ice drag coefficient	5.0×10^{-3}	
C_{hio}	turbulence ice ocean heat transfer coef.	5.0×10^{-3}	
C_{lat}	latent heat bulk transfer coef.	1.75×10^{-3}	
c_{pa}	specific heat of air	1004.0	$\text{J kg}^{-1} \text{K}^{-1}$
c_{pw}	specific heat of seawater	4000.0	$\text{J kg}^{-1} \text{K}^{-1}$
C_{sen}	sensible heat bulk transfer coef.	1.75×10^{-3}	
d	constant in floe collision rheology	0.01	
g	gravitational acceleration	9.81	m s^{-2}
h_0	demarcation ice thickness	0.1	m
h_{min}	minimum ice thickness	0.1	m
k_i	thermal conductivity of ice	2.04	$\text{W m}^{-1} \text{K}^{-1}$
k_s	thermal conductivity of snow	0.31	$\text{W m}^{-1} \text{K}^{-1}$
L_{melt}	latent heat of fusion	3.3×10^5	J kg^{-1}
L_{subl}	latent heat of sublimation	2.8×10^6	J kg^{-1}
L_{vap}	latent heat of vaporization	2.5×10^6	J kg^{-1}

n_{sub}	number of elastic sub-cycles	120	
P^*	ice compressive strength	3.0×10^4	Pa
P_{col}^*	floe collision parameter	10^{12}	Pa s ²
R	radius of Earth	6371×10^3	m
S	solar constant	1353	W m ⁻²
S_I	sea ice salinity	5.0	g kg ⁻¹
T_i^{melt}	melting point of sea ice	273.05	K
T_s^{melt}	melting point of snow	273.15	K
α_i	albedo of sea ice	0.7	
α_s	albedo of snow	0.9	
α_w	albedo of seawater	0.1	
ε_i	sea ice emissivity	0.97	
ε_s	snow emissivity	0.99	
ε_w	seawater emissivity	0.97	
κ	von Karman constant	0.4	
ρ_a	air density	1.247	kg m ⁻³
ρ_i	sea ice density	910	kg m ⁻³
ρ_s	snow density	330	kg m ⁻³
ρ_w	seawater density	1025.9	kg m ⁻³
σ_b	Stefan-Boltzman constant	5.67×10^{-8}	

2.1. Ocean model

The ocean part of the coupled ice-ocean model is a parallelized version of Princeton Ocean Model based on the technique of Message Passing Interface (MPI), which is formulated on a three-dimensional spherical coordinate system. Zonal and meridional grid spacing is approximately 25×25 km and 2.5×2.5 km for the whole Arctic Ocean and high-resolution regional models, respectively. To avoid the singularity at the North Pole, the model's coordinate system is rotated to the equator. The vertical grid uses sigma coordinate systems with 33 levels for both the whole Arctic and regional models. The sigma coordinate is calculated as

$$\sigma = \frac{z - \eta}{H + \eta} \quad (2-1)$$

where, H is bottom topography and, η is surface elevation. Thus, σ ranges from $\sigma = 0$ at $z = \eta$ to $\sigma = -1$ at $z = H$. To better resolve the surface and bottom ocean dynamics, we have adopted the logarithmic distribution of vertical sigma layers near top and bottom surfaces (Table 2-2). To further reduce the pressure gradient error Haney (1991) Mellor et al. (1994) associated with sigma coordinate, the bottom topography is smoothed so that the bottom slope between adjacent two grid points,

$$\frac{|H_1| - |H_2|}{|H_1| + |H_2|} \leq 0.175 \quad (2-2)$$

(where H_1 and H_2 are the depths of the adjacent two grid points) is not beyond 0.175.

Table 2-2 Vertical sigma levels

0	-0.0005	-0.00125	-0.0025	-0.00375	-0.005	-0.0075	-0.01	-0.0125	-0.015	-0.02
-0.025	-0.03125	-0.0375	-0.04375	-0.05	-0.0625	-0.075	-0.0875	-0.1	-0.125	-0.175
-0.25	-0.325	-0.4	-0.475	-0.55	-0.625	-0.7	-0.775	-0.85	-0.925	-1

2.1.1. Primitive equations

The continuity and momentum equations are written in the sigma coordinate system and spatially discretized using the Arakawa C grid. Note that through this thesis λ represents the zonal (longitude) direction and ϕ represents the meridional (latitude) direction. The continuity equation in curvilinear coordinate system is written as:

$$\frac{\partial \eta}{\partial t} + \frac{1}{h_\lambda h_\phi} \left[\frac{\partial DU h_\phi}{\partial \lambda} + \frac{\partial DV h_\lambda}{\partial \phi} \right] + \frac{\partial \omega}{\partial \sigma} = 0 \quad (2-3)$$

where, ω is the transformed vertical velocity; physically, ω is the velocity component normal to sigma surfaces. $D = H + \eta$ and U, V are zonal and meridional direction ocean velocities. And h_λ and h_ϕ are coordinate matrices in zonal and meridional directions.

The conservation of momentum equations are written in curvilinear coordinates as

$$\begin{aligned} & \frac{\partial UD}{\partial t} + \frac{1}{h_\lambda h_\phi} \left[\frac{\partial U^2 D h_\phi}{\partial \lambda} + \frac{\partial UVD h_\lambda}{\partial \phi} \right] + \frac{\partial U\omega}{\partial \sigma} + \frac{UVD}{h_\lambda h_\phi} \frac{\partial h_\lambda}{\partial \phi} - \frac{U^2 D}{h_\lambda h_\phi} \frac{\partial h_\phi}{\partial \lambda} \\ & - fVD + gD \frac{\partial \eta}{\partial \lambda} + \frac{gD^2}{\rho_\circ} \int_\sigma^0 \left[\frac{\partial \rho'}{\partial \lambda} - \frac{\sigma'}{D} \frac{\partial D}{\partial \lambda} \frac{\partial \rho'}{\partial \sigma'} \right] d\sigma' = \frac{\partial}{\partial \sigma} \left[\frac{K_M}{D} \frac{\partial U}{\partial \sigma} \right] + F_\lambda \end{aligned} \quad (2-4)$$

$$\begin{aligned} & \frac{\partial VD}{\partial t} + \frac{1}{h_\lambda h_\phi} \left[\frac{\partial UVD h_\phi}{\partial \lambda} + \frac{\partial V^2 D h_\lambda}{\partial \phi} \right] + \frac{\partial V\omega}{\partial \sigma} + \frac{UVD}{h_\lambda h_\phi} \frac{\partial h_\phi}{\partial \lambda} - \frac{U^2 D}{h_\lambda h_\phi} \frac{\partial h_\lambda}{\partial \phi} \\ & + fUD + gD \frac{\partial \eta}{\partial \phi} + \frac{gD^2}{\rho_\circ} \int_\sigma^0 \left[\frac{\partial \rho'}{\partial \phi} - \frac{\sigma'}{D} \frac{\partial D}{\partial \phi} \frac{\partial \rho'}{\partial \sigma'} \right] d\sigma' = \frac{\partial}{\partial \sigma} \left[\frac{K_M}{D} \frac{\partial V}{\partial \sigma} \right] + F_\phi \end{aligned} \quad (2-5)$$

For the definition of the variables, see the users guide for POM Mellor (2003a)

The transport equations for temperate (T) and salinity (S) are represented by

$$\begin{aligned} & \frac{\partial TD}{\partial t} + \frac{1}{h_\lambda h_\phi} \left[\frac{\partial TUD h_\phi}{\partial \lambda} + \frac{\partial TVD h_\lambda}{\partial \phi} \right] + \frac{\partial T\omega}{\partial \sigma} \\ & = \frac{\partial}{\partial \sigma} \left[\frac{K_H}{D} \frac{\partial T}{\partial \sigma} \right] + F_T - \frac{\partial R}{\partial z} - R_t (T - T_0) \end{aligned} \quad (2-6)$$

$$\begin{aligned} & \frac{\partial SD}{\partial t} + \frac{1}{h_\lambda h_\phi} \left[\frac{\partial SUD h_\phi}{\partial \lambda} + \frac{\partial SVD h_\lambda}{\partial \phi} \right] + \frac{\partial S\omega}{\partial \sigma} \\ & = \frac{\partial}{\partial \sigma} \left[\frac{K_H}{D} \frac{\partial S}{\partial \sigma} \right] + F_S - R_s (S - S_0) \end{aligned} \quad (2-7)$$

where R_t and R_s are restoring constants, and T_0 and S_0 are climatological temperature and salinity as which the Polar Science Center Hydrographic Climatology (PHC3.0) dataset Steele et al. (2001) is used. Note that restoring constants are only used in spin-up run with 30days time scale and otherwise set to zero. Turbulence kinetic energy (q^2), and Turbulence length scale ($q^2 l$) are calculated by

$$\begin{aligned} & \frac{\partial q^2 D}{\partial t} + \frac{1}{h_\lambda h_\phi} \left[\frac{\partial q^2 UD h_\phi}{\partial \lambda} + \frac{\partial q^2 VD h_\lambda}{\partial \phi} \right] + \frac{\partial q^2 \omega}{\partial \sigma} = \frac{\partial}{\partial \sigma} \left[\frac{K_q}{D} \frac{\partial q^2}{\partial \sigma} \right] \\ & + \frac{2K_M}{D} \left[\left(\frac{\partial U}{\partial \sigma} \right)^2 + \left(\frac{\partial V}{\partial \sigma} \right)^2 \right] + \frac{2g}{\rho_\circ} K_H \frac{\partial \tilde{\rho}}{\partial \sigma} - \frac{2Dq^3}{B_1 l} + F_q \end{aligned} \quad (2-8)$$

$$\begin{aligned} & \frac{\partial q^2 l D}{\partial t} + \frac{1}{h_\lambda h_\phi} \left[\frac{\partial q^2 l UD h_\phi}{\partial \lambda} + \frac{\partial q^2 l VD h_\lambda}{\partial \phi} \right] + \frac{\partial q^2 l \omega}{\partial \sigma} = \frac{\partial}{\partial \sigma} \left[\frac{K_q}{D} \frac{\partial q^2 l}{\partial \sigma} \right] \\ & + E_1 l \left(\frac{K_M}{D} \left[\left(\frac{\partial U}{\partial \sigma} \right)^2 + \left(\frac{\partial V}{\partial \sigma} \right)^2 \right] + E_3 \frac{g}{\rho_\circ} K_H \frac{\partial \tilde{\rho}}{\partial \sigma} \right) - \frac{Dq^3}{B_1} \tilde{W} + F_l \end{aligned} \quad (2-9)$$

The level-2.5 turbulence closure scheme Mellor and Yamada (1982) is used to calculate the vertical eddy viscosities and diffusivities.

Horizontal eddy viscosities F_λ and F_ϕ are defined as,

$$F_\lambda = \frac{1}{h_\lambda h_\phi} \left[\frac{\partial}{\partial \lambda} (h_\phi H \tau_{\lambda\lambda}) + \frac{\partial}{\partial \phi} (h_\lambda H \tau_{\lambda\phi}) \right] \quad (2-10)$$

$$F_\phi = \frac{1}{h_\lambda h_\phi} \left[\frac{\partial}{\partial \lambda} (h_\phi H \tau_{\lambda\phi}) + \frac{\partial}{\partial \phi} (h_\lambda H \tau_{\phi\phi}) \right] \quad (2-11)$$

where,

$$\tau_{\lambda\lambda} = 2A_M \frac{1}{h_\lambda} \frac{\partial U}{\partial \lambda} \quad (2-12)$$

$$\tau_{\lambda\phi} = \tau_{\phi\lambda} = A_M \left[\frac{h_\lambda}{h_\phi} \frac{\partial}{\partial \phi} \left(\frac{U}{h_\lambda} \right) + \frac{h_\phi}{h_\lambda} \frac{\partial}{\partial \lambda} \left(\frac{V}{h_\phi} \right) \right] \quad (2-13)$$

$$\tau_{\phi\phi} = 2A_M \frac{1}{h_\phi} \frac{\partial V}{\partial \phi} \quad (2-14)$$

Horizontal eddy diffusivities of T , S , q^2 and $q^2 l$ are represented in the symbol β and defined in equation 2-15.

$$F_\beta = \frac{1}{h_\lambda h_\phi} \left[\frac{\partial}{\partial \lambda} (h_\phi H q_\lambda) + \frac{\partial}{\partial \phi} (h_\lambda H q_\phi) \right] \quad (2-15)$$

where,

$$q_\lambda = A_H \frac{1}{h_\lambda} \frac{\partial \beta}{\partial \lambda} \quad (2-16)$$

$$q_\phi = A_H \frac{1}{h_\phi} \frac{\partial \beta}{\partial \phi} \quad (2-17)$$

The horizontal eddy viscosity coefficient A_M and diffusivity coefficient A_H are calculated using a formula proportional to the horizontal grid size and velocity gradients SMAGORINSKY (1963). The proportionality coefficient C is chosen to be 0.2.

$$A_M = C \Delta x \Delta y \frac{1}{2} \left[\left(\frac{\partial U}{\partial x} \right)^2 + \frac{1}{2} \left(\frac{\partial V}{\partial x} + \frac{\partial U}{\partial y} \right)^2 + \left(\frac{\partial V}{\partial y} \right)^2 \right]^{1/2} \quad (2-18)$$

$$A_H = 0.1 A_M \quad (2-19)$$

In the above equations 2-10 to 2-17 are the approximations for horizontal eddy viscosities and diffusivities. Therefore the justification for the present formulation is required and can be found in the Mellor and Blumberg (1985).

To solve the above primitive equations, POM has adopted the mode splitting technique. Mode splitting is the method separating the fast moving external gravity waves and slowly moving internal gravity waves. This mode splitting method is desirable in terms of computer economy to separate the vertically integrated equations (external mode) from the vertical structure equations (internal mode). In terms of time steps the external mode uses relatively short time step and the internal mode uses larger time step. In the whole Arctic model, the external and internal time steps are set to 16 and 480 s, respectively. The more details about POM solution techniques can be seen in the POM user guide Mellor (2003b).

2.1.2. Ice-ocean coupling and boundary conditions

The vertical boundary conditions for continuity equation (2-3) are obtained from mass balance at the ocean surface and bottom. At the surface:

$$\omega(0) = W(0) - U \left(\sigma \frac{\partial D}{\partial x} + \frac{\partial \eta}{\partial x} \right) - V \left(\sigma \frac{\partial D}{\partial y} + \frac{\partial \eta}{\partial y} \right) - \sigma \frac{\partial D}{\partial t} - \frac{\partial \eta}{\partial t} \quad (2-20)$$

$$\rho_w W(0) = (1 - A)(\dot{E} - \dot{P}) + \rho_i \frac{dV_i}{dt} \quad (2-21)$$

where, $W(0)$ and $\omega(0)$ are vertical velocities at the surface in Cartesian coordinate systems and sigma coordinate systems respectively. At the bottom:

$$\omega(-1) = 0 \quad (2-22)$$

where, ρ_w , ρ_i , A , \dot{E} , \dot{P} , and V_i are sea water density, sea ice density, sea ice concentration, evaporation flux, precipitation flux, and net melt sea ice volume, respectively.

The surface boundary conditions for momentum equations 2-4 and 2-5 are given by

$$\frac{K_M}{D} \left(\frac{\partial U}{\partial \sigma}, \frac{\partial V}{\partial \sigma} \right) = -(\langle wu(0) \rangle, \langle wv(0) \rangle), \quad \sigma \rightarrow 0 \quad (2-23)$$

where, the right hand sides are surface turbulence momentum fluxes. These momentum fluxes are calculated from the wind stress over the ocean τ_{aw} and ice to ocean stress τ_{iw} weighting with sea ice concentrations as follows

$$-(\langle wu(0) \rangle, \langle wv(0) \rangle) = \frac{1}{\rho_w} (\tau_x, \tau_y) \quad (2-24)$$

$$(\tau_x, \tau_y) = (1-A)\bar{\tau}_{aw} + A\bar{\tau}_{iw} \quad (2-25)$$

$$(\tau_x, \tau_y) = (1-A) \times \rho_a C_{Daw} |\bar{U}_a| \bar{U}_a + A \times \rho_w C_{Diw} |\bar{U}_w - \bar{U}_i| (\bar{U}_w - \bar{U}_i) \quad (2-26)$$

where U_w is the ocean velocity, U_i is the sea ice velocity, C_{Daw} is the drag coefficient between air and ice (the air-ice drag coefficient), and C_{Diw} is the drag coefficient between ice and ocean (the ice-ocean drag coefficient). C_{Daw} is derived from the formulation of Large and Pond (1981) as follows:

$$C_{Daw} = \begin{cases} (0.49 + 0.065|\bar{U}_a|) \times 10^{-3} & |\bar{U}_a| > 11 \\ 1.2 \times 10^{-3} & |\bar{U}_a| \leq 11 \end{cases} \quad (2-27)$$

C_{Diw} is set to be a constant value of 5.0×10^{-3} . On the other hand, bottom boundary conditions for the momentum equations are defined according to the numerical solution of “law of the wall” as

$$\begin{aligned} \frac{K_M}{D} \left(\frac{\partial U}{\partial \sigma}, \frac{\partial V}{\partial \sigma} \right) &= -C_z [U^2 + V^2]^{1/2} (U, V), \quad \sigma \rightarrow -1 \\ C_z &= \text{MAX} \left[\frac{\kappa^2}{[\ln(1 + \sigma_{kb-1} H/z_0)]^2}, 0.0025 \right] \end{aligned} \quad (2-28)$$

where κ is von Karman constant and z_0 is the roughness parameter being set to 0.01m in this study. σ_{kb-1} is the first grid point nearest to the bottom.

The vertical boundary conditions for transport equations of temperature and salinity (equation 2-6 and 2-7) are given by

$$\frac{K_H}{D} \left(\frac{\partial T}{\partial \sigma}, \frac{\partial S}{\partial \sigma} \right) = -(\langle wT' \rangle, \langle wS' \rangle), \quad \sigma \rightarrow 0 \quad (2-29)$$

$$\frac{K_H}{D} \left(\frac{\partial T}{\partial \sigma}, \frac{\partial S}{\partial \sigma} \right) = 0, \quad \sigma \rightarrow -1 \quad (2-30)$$

The turbulent heat and salt fluxes at the surface are given by

$$\langle wT' \rangle = F_{aw} \times (1 - A) - F_{wi} \times A + \rho_i L_i \frac{dV_i}{dt} \quad (2-31)$$

$$\langle wS' \rangle = s_w (\dot{E} - \dot{P})(1 - A) + (s_w - s_I) \rho_i \frac{\partial V_i}{\partial t} \quad (2-32)$$

where F_{aw} is the net heat input into the ocean, F_{wi} is the net heat transfer to ice bottom from the ocean, L_i is the latent heat of sea ice, S_w is the salinity in the surface layer, and S_I is the salinity of sea ice. More details on the heat fluxes may be found in section 2.3.

The vertical boundary conditions for turbulence kinetic energy and length scale can be defined as follows:

$$(q^2(0), q^2 l(0)) = (B_1^{2/3} u^{*2}(0), q^2(\sigma_1) \kappa D \sigma_1) \quad (2-33)$$

$$(q^2(-1), q^2 l(-1)) = (B_1^{2/3} u^{*2}(-1), 0) \quad (2-34)$$

where, u^* is friction velocity, σ_1 is the value of σ coordinate corresponding to second sigma level ($k=1$), B_l is set to 1580, and the other constants are defined according to Mellor and Blumberg (2004). A gravity-wave radiation condition is applied for open lateral boundaries and a no slip condition is applied for coastlines and islands.

2.2. Ice model

Ice-ocean coupled model ice part is based on Fujisaki et al. (2010). However in present model the original version of the ice part was modified due to the stability issues (see section 3). In this section three main parts of sea ice model is described (momentum equation, rheological modeling and tracer advection modeling).

2.2.1. Momentum equation

In the sea ice dynamic model, two dimensional momentum equations are solved in a curvilinear coordinate system as follows:

$$\rho_i h A \frac{\partial u_i}{\partial t} = F_\lambda + \tau_{ai} + \tau_{wi} + \rho_i h A f v_i - \rho_i h g \frac{1}{R \cos \phi} \frac{\partial H_o}{\partial \lambda} \quad (2-35a)$$

$$\rho_i h A \frac{\partial v_i}{\partial t} = F_\phi + \tau_{ai} + \tau_{wi} - \rho_i h A f u_i - \rho_i h g \frac{1}{R} \frac{\partial H_o}{\partial \phi} \quad (2-35b)$$

where, ρ_i , h , A , u_i , v_i , f , R and H_o are ice density, thickness, concentration and zonal and meridional velocities, Coriolis parameter, Earth radius and sea surface height respectively. Note that through this thesis λ represents the zonal (longitude) direction and ϕ represents the meridional (latitude) direction. Air to ice τ_{ai} and ocean to ice τ_{wi} stresses are calculated according to the quadratic relation as follows:

$$\tau_{ai} = \rho_a C_{Dai} |\vec{u}_i| \vec{u}_i \quad (2-36)$$

$$\tau_{wi} = \rho_w C_{Dwi} |\vec{u}_w - \vec{u}_i| (\vec{u}_w - \vec{u}_i) \quad (2-37)$$

where ρ_a , ρ_w , u_w , C_{Dai} and C_{Dwi} are air density, sea water density, upper surface ocean velocity, air to ice drag coefficient and ocean to ice drag coefficient, respectively. Note that over arrow represent the vector fields. Please note that we have used the first layer ocean velocity to calculate the ocean to ice stress (τ_{wi}), because the vertical resolution in the ice-POM model is enough to calculate the surface velocities accurately. On the other hand, many researches (Hibler 1979; E. Hunke and Dukowicz 1997) have used the geostrophic approximation with 25 degree turning angle instead.

Internal ice stress gradient $\mathbf{F} = (F_\lambda, F_\phi)$ is calculated as the divergence of stress tensor $\boldsymbol{\sigma}$ Zhang and Hibler (1997).

$$F_\lambda = \frac{1}{R \cos \phi} \frac{\partial \sigma_{\lambda\lambda}}{\partial \lambda} + \frac{1}{R} \frac{\partial \sigma_{\lambda\phi}}{\partial \phi} - \frac{2\sigma_{\lambda\phi} \tan \phi}{R} \quad (2-38)$$

$$F_\phi = \frac{1}{R \cos \phi} \frac{\partial \sigma_{\lambda\phi}}{\partial \lambda} + \frac{1}{R} \frac{\partial \sigma_{\phi\phi}}{\partial \phi} + \frac{(\sigma_{\lambda\lambda} - \sigma_{\phi\phi}) \tan \phi}{R} \quad (2-39)$$

where R is earth radius. The stress tensor is related to strain rate $\dot{\epsilon}$ and ice strength parameter P via a constitutive relationship, which depends on the sea ice rheology (see subsection 2.2.2)

2.2.2. Rheological modeling

Most of sea ice numerical models are based on the continuum approach in ice dynamic processes Hibler (1979); Hunke and Dukowicz (1997); Coon et al. (1974). On scale much larger than floe size, continuum approximation is commonly assumed. The advantages of a continuum model are its simplicity, low computational cost and good description of large-scale sea ice behaviors. On the other hand there are some researchers who modeled the small-scale sea ice behaviors using discrete elements techniques Shen et al. (1986); Lu et al. (1989); Leppäranta and Hibler III (1985). However, the practical application with discrete element technic was limited because of the high computational cost. However, when dealing with an ice forecast in a marginal ice zones such as the Arctic sea routes, it is not realistic to treat sea ice as a continuum body because the sea ice consists of both continuum and discrete ice floes. Therefore, a model that takes account of the ice discrete characteristics is needed for sea ice predictions using higher-resolution computations. To answer this problem, we have introduced the floe collision rheology Sagawa (2007) into the conventional Elastic-viscous-plastic rheology Hunke and Dukowicz (1997) as follows. In the elastic-viscous-plastic rheology, the constitutive equations are represented by

$$\frac{1}{E} \frac{\partial \sigma_{\lambda\lambda}}{\partial t} + \frac{\eta + \xi}{4\eta\xi} \sigma_{\lambda\lambda} + \frac{\eta - \xi}{4\eta\xi} \sigma_{\phi\phi} + \frac{P}{4\xi} = \dot{\epsilon}_{\lambda\lambda} \quad (2-40a)$$

$$\frac{1}{E} \frac{\partial \sigma_{\phi\phi}}{\partial t} + \frac{\eta - \xi}{4\eta\xi} \sigma_{\lambda\lambda} + \frac{\eta + \xi}{4\eta\xi} \sigma_{\phi\phi} + \frac{P}{4\xi} = \dot{\epsilon}_{\phi\phi} \quad (2-40b)$$

$$\frac{1}{E} \frac{\partial \sigma_{\lambda\phi}}{\partial t} + \frac{1}{2\eta} \sigma_{\lambda\phi} = \dot{\epsilon}_{\lambda\phi} \quad (2-40c)$$

Strain rate tensor $\dot{\epsilon}$ is expressed by means of sea ice velocities as follows

$$\dot{\epsilon}_{\lambda\lambda} = \frac{1}{R \cos \phi} \frac{\partial u_i}{\partial \lambda} - \frac{v_i \tan \phi}{R} \quad (2-41)$$

$$\dot{\epsilon}_{\phi\phi} = \frac{1}{R} \frac{\partial v_i}{\partial \phi} \quad (2-42)$$

$$\dot{\epsilon}_{\lambda\phi} = \frac{1}{2} \left(\frac{1}{R} \frac{\partial u_i}{\partial \phi} + \frac{u_i \tan \phi}{R} + \frac{1}{R \cos \phi} \frac{\partial v_i}{\partial \lambda} \right) \quad (2-43)$$

Non-linear shear viscosity η and bulk viscosity ζ are parameterized as

$$\zeta = \frac{P}{2\Delta} \quad (2-44)$$

$$\eta = \frac{P}{2\Delta e^2} = \frac{\zeta}{e^2} \quad (2-45)$$

where strain rate parameter Δ is defined as

$$\Delta = \left[\left(\dot{\epsilon}_{\lambda\lambda}^2 + \dot{\epsilon}_{\phi\phi}^2 \right) (1 + e^{-2}) + 4e^{-2} \dot{\epsilon}_{\lambda\phi}^2 + 2\dot{\epsilon}_{\lambda\lambda} \dot{\epsilon}_{\phi\phi} (1 + e^{-2}) \right]^{1/2} \quad (2-46)$$

and e is the ratio of principal axes of the elliptical yield curve and the value is equal to 2. In order to avoid the viscosities become infinite in the limit of zero strain rates, we have set the upper and lower boundaries to the bulk viscosity as follows.

$$4 \times 10^{11} \leq \zeta \leq (2.5 \times 10^8) P \quad (2-47)$$

The elastic parameter E is now defined in terms of damping timescale (T) for elastic waves. T is a tunable parameter and in present study we choose 0.36 times the ice dynamics time step (Δt).

$$E = \frac{\zeta}{T} \quad (2-48)$$

According to Hibler (1979), parameterization for ice strength is a function of ice thickness and exponential function of ice concentration as follows:

$$P = P^* h A \exp(-C(1-A)) \quad (2-49)$$

here P^* is a parameter for the maximum sea ice strength and C is the strength reduction coefficient for lead opening.

As shown in Figure 2-1(a), the ice strength (derived from Hibler's formulation) is independent of strain rates and only a function of the concentration. Hibler's formulation is reasonable when the ice concentrations are greater than 90% where the

ice behaves in compact condition and concentrations are smaller than 50% where the ice behaves in free drift conditions. But in between those concentrations there should be a region where the ice floe collision should dominant Leppäranta (2005). But in Hibler's ice strength parameterization, this ice floe collision has not been taken into account. Therefore to introduce the floe collision into the ice model we have customized the Hibler's ice strength equation 2-49 using the Sagawa's method as follows.

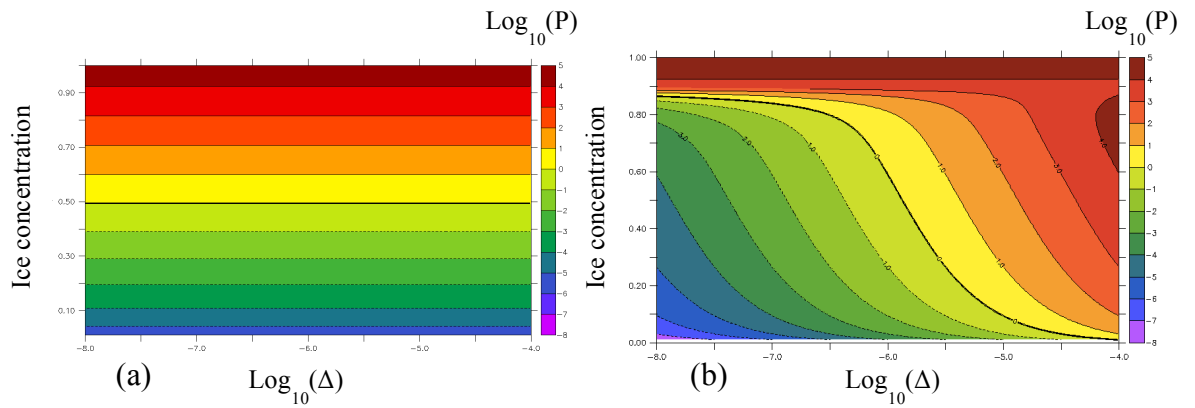


Figure 2-1 Ice strength as a function of ice concentration and strain rate parameter Δ . (a) Hibler's formulation, (b) Sagawa's formulation (reproduced from Sagawa 2007)

Sagawa's floe collision theory is based on the following assumptions. In the case of two floe groups, which consist of uniform floes, collide each other and coalesce into one bunch. Momentum transfer is assumed to be proportional to velocity difference. Stress can be parameterized as proportional to the square of strain rates. Therefore, we introduce the new set of equations for strength parameter P as follows:

$$P = \frac{P_{col}^* \alpha^{(1-x)} h A}{\max\left(A^{-1} - \frac{2\sqrt{3}}{\pi} \gamma^{-1}, d\right)} \Delta^{2x} \quad (2-50)$$

$$x = 1 - \exp\left(-C_{col} \left(\frac{\pi}{2\sqrt{3}} \gamma - A\right)\right) \quad (2-51)$$

$$\alpha = \frac{P^*}{P_{col}^*} d A_{\max} \exp(-C(1 - A_{\max})) \quad (2-52)$$

where P_{col}^* is a collision strength parameter, C_{col} is a switching ratio to floe collision mode, and γ is maximum compactness of the ice floes. The comparison of ice strength

equation by Hibler (1979) with that by Sagawa (2007) can be seen in the Figure 2-1. Note that if the concentrations are higher than A_{\max} (=90%), Sagawa's parameterization is equal to Hibler's formulation.

2.2.3. Tracer advection

Prognostic equations for sea ice concentration and ice thickness are given by

$$\frac{\partial A}{\partial t} + \frac{1}{R \cos \phi} \left[\frac{\partial}{\partial \lambda} (A u_i) + \frac{\partial}{\partial \phi} (A v_i \cos \phi) \right] = F_A \quad (2-53)$$

$$\frac{\partial A h_i}{\partial t} + \frac{1}{R \cos \phi} \left[\frac{\partial}{\partial \lambda} (A h_i u_i) + \frac{\partial}{\partial \phi} (A h_i v_i \cos \phi) \right] = F_{iv} \quad (2-54)$$

where F_A and F_{iv} are thermodynamic source terms described in section 2.3 and h_0 is demarcation sea ice thickness being set to 0.1m in this study.

Instead of the floe collision rheology, to improve the ice edge locations we have implemented the Eulerian-Lagrangian method for advection of the sea ice variables. First, we have solved the momentum equation in Eulerian grid and then solved the ice conservation law in a Lagrangian grid. The ice field is represented by a large number of particles with given thickness and size. In each Eulerian grid cell, particles are summed for compactness and mean thickness, and then momentum equation can be solved for velocities. Using the above Eulerian grid velocities, each Eulerian cell ice particle bunch is advected in space for new configurations. Finally, the new ice state is obtained for Eulerian grid by summing and redistributing the advected configurations.

2.3. Thermodynamic model

In the ice-ocean coupled model sea ice is assumed to be horizontally homogeneous slab floating on seawater. In the thermodynamics model vertical ice growth and attenuation (ice thickness change) and lateral growth and melting (ice concentration change) are modeled independently according to Parkinson and Washington (1979) which is based on Semtner (1976), zero layer model. Temperature and thickness of sea ice are controlled by the conduction of heat through the ice slab and balance of fluxes at its upper and lower surfaces.

2.3.1. Surface heat flux calculation

The components of surface heat fluxes, the shortwave solar radiation F_{sw} , incoming longwave radiation F_{LE} , sensible heat flux F_{sen} , latent heat flux F_{lat} , and outgoing longwave radiation F_{LO} , and heat input from ocean to ice bottom F_{wi} are calculated by following equations. The outgoing longwave radiation, sensible heat and latent heat fluxes are function of surface temperature T_{sfc} and surface (snow, sea ice or water) properties.

2.3.1.1. Shortwave radiations

Empirical equations of clear sky shortwave radiation F_{swo} was introduced by Zillman (1972). Same method has been adopted in the present study

$$F_{swo} = \frac{S \cos^2 Z}{(\cos Z + 2.7)vp \times 10^{-5} + 1.085 \cos Z + 0.1} \quad (2-55)$$

$$\cos Z = \sin \phi \sin \delta + \cos \phi \cos \delta \cos HA \quad (2-56)$$

$$\delta = 23.44^\circ \frac{\pi}{180} \cos \left[(172 - J) \frac{\pi}{180} \right] \quad (2-57)$$

$$HA = (12 - H) \frac{\pi}{12} \quad (2-58)$$

where, S solar constant, Z zenith angle, vp vapor pressure, ϕ latitude, δ sun declination angle, J days in year, HA sun hour angle, and H local time. The values of the constants are defined in Table 2-1. The clear sky shortwave radiation is modified by introducing the effect of cloud cover Laevastu (1960) as follows:

$$F_{sw} = F_{swo} (1 - 0.6c^3) \quad (2-59)$$

where c is total cloud cover, which is defined in the range of 0 to 1.

2.3.1.2. Incoming longwave radiation

Clear skies longwave radiation F_{LEo} is modeled using the theories by Efimova (1961)

$$F_{LEo} = \sigma_b T_a^4 \left(0.746 + 6.6 \times 10^{-5} vp \right) \quad (2-60)$$

where, σ_b is Stefan-Boltzmann constant and T_a is atmospheric temperature. The above equation is further modified to introduce the cloud effect by the Parkinson and Washington (1979) method in ice-POM model as follows.

$$F_{LE} = F_{LEo} (1 + 0.275c) \quad (2-61)$$

2.3.1.3. Outgoing longwave radiation

The outgoing longwave radiation depends on the surface temperature T_{sfc} , and surface emissivity (snow, ice or water) ε_{sfc}

$$F_{LO} = \varepsilon_{sfc} \sigma T_{sfc}^4 \quad (2-62)$$

2.3.1.4. Sensible heat flux

The sensible heat is calculated by using the bulk aerodynamics formula (upward flux is considered as positive)

$$F_{sen} = \rho_a c_{pa} C_{sen} |U_a| (T_{sfc} - T_a) \quad (2-63)$$

$$|U_a| = \sqrt{u_a^2 + v_a^2} \quad (2-64)$$

where U_a is absolute wind speed, ρ_a is air density, T_a is air temperature, T_{sfc} is the surface temperature, C_{sen} is the turbulence heat transfer coefficient C_{sen} is set as a constant in ice-POM model and c_{pa} is specific heat of air

2.3.1.5. Latent heat flux

The latent heat is also calculated by using the aerodynamics bulk formula.

$$F_{lat} = \rho_a L_{sfc} C_{lat} |U_a| (q_{sfc} - q_a) \quad (2-65)$$

where C_{lat} is defined as latent heat bulk transfer coefficients, L_{sfc} is the surface latent heat of vaporization or sublimation, depending on the surface conditions explained in Haltiner and Martin (1957). q_{sfc} and q_a are specific humidities at surface and atmosphere which are defined as,

$$q_{sfc} = \frac{0.622 \times vps}{P_a - 0.378 \times vps} \quad (2-66)$$

$$q_a = \frac{0.622 \times vp}{P_a - 0.378 \times vp} \quad (2-67)$$

Saturated vapor pressure vps is determined from an empirical formula proposed by Murray (1967)

$$vps = 611 \times 10^{\frac{a(T_{sfc} - 273.16)}{(T_{sfc} - b)}} \quad (2-68)$$

where, $(a,b) = (9.5, 7.66)$ if ice cover exists and $(7.5, 35.86)$ if no ice cover exists.

2.3.1.6. Heat flux from ocean to ice bottom

The turbulence heat flux from ocean to ice bottom is parameterized as,

$$F_{wi} = \rho_w c_{pw} C_{hio} u^* (T_w - T_w^{fz}) \quad (2-69)$$

Here ρ_w and c_{pw} denote the density and the specific heat of seawater, respectively. T_w and T_w^{fz} are the ocean uppermost layer temperature and associated freezing temperature. Please note that ice bottom temperature T_{bim} has been set equal to the ocean freezing temperature T_w^{fz} , being a function of salinity S_w given by:

$$T_w^{fz} = 273.15 - 0.0575 \times S_w + 1.710523 \times S_w^{3/2} - 2.154996 \times S_w^2 \quad (2-70)$$

where u^* denotes the friction velocity, which is the square root of the sea surface stress divided by the density of sea water.

$$u^* = \sqrt{\frac{\tau_w}{\rho_w}} \quad (2-71)$$

Here, the sea surface stress τ_w is calculated from equation 2-26. C_{hio} is a turbulence heat transfer coefficient. We have set the value of C_{hio} based on McPhee et al. (2008).

2.3.2. Vertical formation of sea ice

Atmosphere to sea ice surface heat fluxes are changed according to the sea ice surface conditions like surface albedo, emissivity etc. Therefore in our computations snow covered sea ice surface flux F_{as} and bare (without snow) sea ice surface flux F_{ai} are calculated according to the surface temperature and surface properties. There are three kinds of surfaces considered in the ice-POM model snow covered ice, snow free ice and open ocean. For each surface condition ice formation and melt are considered in this section.

2.3.2.1. Snow free sea ice cover

The variation of ice thickness can be formulated as a system of one dimensional heat equation as follows

$$c_i \rho_i \frac{\partial T}{\partial t} = \frac{\partial}{\partial z} \left(k_i \frac{\partial T}{\partial z} \right) \quad (2-72)$$

By applying the boundary conditions at upper and lower surface to the above equation, total variation of ice thickness at upper and lower surfaces are calculated:

Upper surface,

$$-L_{melt} \rho_i \frac{\partial h}{\partial t} = F_i - k_i \frac{\partial T}{\partial z} \Big|_{z=h_i} \quad \text{when } T_{z=h_i} = T_i^{melt} \quad (2-73)$$

$$0 = F_i - k_i \frac{\partial T}{\partial z} \Big|_{z=h_i} \quad \text{when } T_{z=h_i} < T_i^{melt} \quad (2-74)$$

Lower surface,

$$-L_{melt} \rho_i \frac{\partial h}{\partial t} = k_i \frac{\partial T}{\partial z} \Big|_{z=0} + F_{wi} \quad (2-75)$$

where c_i and k_i denote the specific heat and thermal conductivity respectively. It is assumed that the vertical profile of temperature is linear. Although the thermal conductivity k_i of ice is a function of salinity and temperature, the range is relatively small and we employed the value obtained under 273.15 [K] and 34 [psu]; that is 2.04 [W/m/K].

When the sea ice is not covered by the snow, as shown in Figure 2-2, the surface heat fluxes are calculated by

$$F_{ai} = (1 - \alpha_i)F_{SW} + F_{LE} - F_{LO} - F_{sen} - F_{lat} \quad (2-76)$$

Then the conductive heat flux G_i is calculated by

$$G_i = \frac{k_i}{h_i} (T_{btm} - T_{sfc}) \quad (2-77)$$

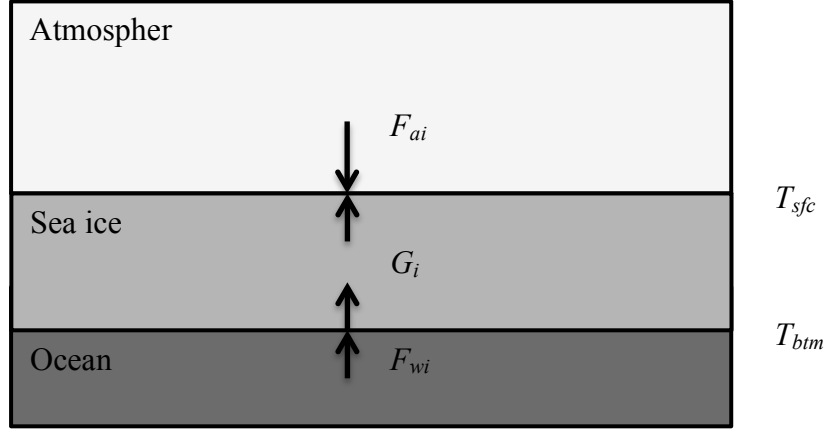


Figure 2-2 Schematic diagram of the energy fluxes at the snow free sea ice

The outgoing longwave radiation, F_{LO} , sensible heat flux F_{sen} and latent heat flux F_{lat} are nonlinear functions of surface temperature. Therefore, a new surface temperature is calculated using the iterative method while maintaining the energy balance at the upper surface:

$$T_{sfc} = T_p + \Delta T \quad (2-78)$$

where, T_p is the surface temperature at the pervious time step and ΔT is the variation.

Energy balance at the upper surface

$$F_{ai} + G_i = \Delta Q \quad (2-79)$$

by applying the net surface heat flux derived from equation 2-76 and assuming zero net heat accumulation at the upper surface in equation 2-79 we have obtained the following equation

$$(1 - \alpha_i)F_{SW} + F_{LE} - F_{LO} - F_{sen} - F_{lat} + \frac{k_i}{h_i} (T_{btm} - T_{sfc}) = 0 \quad (2-80)$$

Variation in the surface temperature is then updated by,

$$\Delta T = \frac{(1 - \alpha_i)F_{SW} + F_{LE} - F_{LO} - F_{sen} - F_{lat} + \frac{k_i}{h_i}(T_{btm} - T_p)}{4\varepsilon_i \sigma T_p^3 + \frac{k_i}{h_i} + \rho_a c_{pa} C_{sen} |U_a|} \quad (2-81)$$

The right hand side of the equation is evaluated using previous time step surface temperature value T_p . If the updated temperature is greater than ice melting temperature T_i^{melt} , then surface temperature is set the T_i^{melt} and excess heat is used to melt the sea ice at the surface according to the equation 2-82.

$$-\Delta h_i^{sfc} = \frac{\Delta t \left((1 - \alpha_i)F_{SW} + F_{LE} - F_{LO} - F_{sen} - F_{lat} + \frac{k_i}{h_i}(T_{btm} - T_i^{melt}) \right)}{L_{melt} \rho_i} \quad (2-82)$$

Finally, applying the energy balance at the bottom surface (according to the equation 2-75) can update the bottom thickness variation as follows:

$$-\Delta h_i^{btm} = \frac{\Delta t \left(F_{wi} - \frac{k_i}{h_i}(T_{btm} - T_{sfc}) \right)}{L_{melt} \rho_i} \quad (2-83)$$

2.3.2.2. Snow covered sea ice

If the sea ice is covered with snow as shown in Figure 2-3 in addition to the above snow free computation we have to calculate the snow ice interface temperature T_{si} . Note that F_{as} and F_{wi} are the total heat fluxes on the snow surface and the heat flux from ocean to ice bottom.

Conductive heat fluxes through snow and sea ice is defined as

$$G_s = \frac{k_s}{h_s}(T_{si} - T_{sfc}) \quad (2-84)$$

$$G_i = \frac{k_i}{h_i}(T_{btm} - T_{si}) \quad (2-85)$$

where k_s is thermal conductivity of snow. Interface energy balance is used to calculate the interface temperature. We have assumed no accumulation of heat at the interface

$$G_s = G_i \quad (2-86)$$

$$T_{si} = \frac{k_s h_i T_{sfc} + k_i h_s T_{btm}}{h_i k_s + h_s k_i} \quad (2-87)$$

Then new surface temperature is calculated using the same method as described in snow free section equation 2-78.

The snow surface temperature is updated by,

$$\Delta T = \frac{(1 - \alpha_s) F_{SW} + F_{LE} - F_{LO} - F_{sen} - F_{lat} + \frac{k_i k_s (T_{btm} - T_p)}{k_s h_i + k_i h_s}}{4 \varepsilon_s \sigma T_p^3 + \frac{k_i k_s}{k_s h_i + k_i h_s} + \rho_a c_{pa} C_{sen} |U_a|} \quad (2-88)$$

if the snow surface temperature is greater than melting point temperature of snow T_s^{melt} , the excess heat is used to melt the snow rather than increase the temperature.

The depth of melting snow is calculated by

$$-\Delta h_s^{sfc} = \frac{\Delta t \left((1 - \alpha_s) F_{SW} + F_{LE} - F_{LO} - F_{sen} - F_{lat} + \frac{k_s}{h_s} (T_{si} - T_s^{melt}) \right)}{L_{melt} \rho_s} \quad (2-89)$$

The bottom surface sea ice melt is calculated using the same equation (equation 2-83) as in snow free calculation.

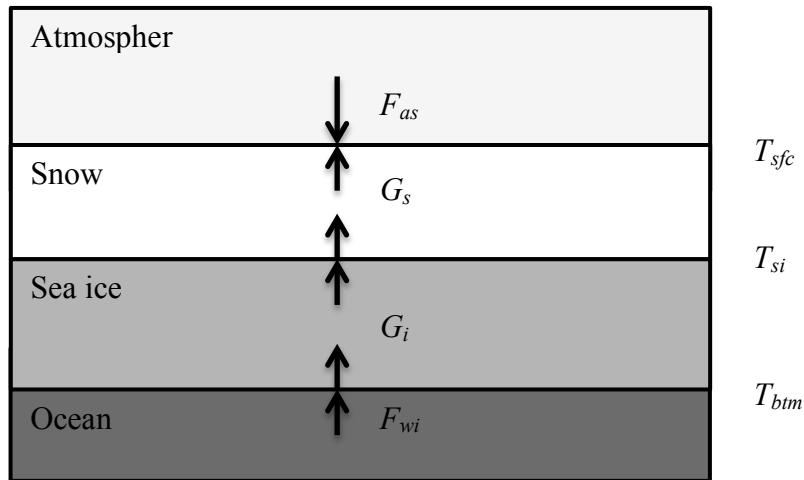


Figure 2-3 Schematic diagram of the energy fluxes at the snow covered sea ice

2.3.3. Lateral growth and melt of sea ice

In ice-POM model if the ocean mixed layer temperature drop below the freezing point temperature (super cooling) part of the water column (Δz_w) is frozen within the time step. Total frozen volume within the time step is defined as,

$$V_i^{frz} = \frac{\rho_w c_{pw} \Delta z_w (T_w^{frz} - T_w)}{\rho_i L_{melt}} \quad (2-90)$$

Meantime, the net heat flux from atmosphere to ocean can be led to melt the existing sea ice and snow. The net heat flux from atmosphere to ocean F_{aw} is defined as follows:

$$F_{aw} = (1 - \alpha_w) F_{SW} + F_{LE} - F_{LO} - F_{sen} - F_{lat} \quad (2-91)$$

where, α_w is seawater albedo. In the above equation total heat available into the lead $F_{aw} (1 - A)$ is used to melt the sea ice laterally and warm the underneath ocean water. The fraction of $F_{aw} A (1 - A)$ is used to melt the sea ice laterally according to Parkinson and Washington (1979).

In ice-POM model we also assumed that the ocean surface heat flux only changes the lateral concentration and does not affect the ice or snow thicknesses. The lateral melts of sea ice and snow concentration due to ocean heat flux is then defined as,

$$A^{melt} = \frac{F_{aw} A (1 - A) dt}{(\rho_i h_i L_{melt} + \rho_s h_s L_{melt})} \quad (2-92)$$

Finally, new ice concentration and thickness due to the lateral melting and formation are formulated in following equations

The new total volume of sea ice and snow defined in equation 2-91 and 2-92 respectively

$$V_i = A h_i + V_i^{frz} - h_i A^{melt} \quad (2-93)$$

$$V_s = (A_i - A^{melt}) h_s \quad (2-94)$$

New concentration of ice and snow is defined as,

$$A^{new} = A - A^{melt} + \min\left(\frac{V_i}{h_{min}}, 1 - A\right) \quad (2-95)$$

Note that equation 2-93 guarantees that sea ice concentrations will not exceed the 100%. Finally, new ice thickness and new snow thickness are calculated using the following equations

$$h_i^{new} = \frac{V_i}{A^{new}} \quad (2-96)$$

$$h_s^{new} = \frac{V_s}{A^{new}} \quad (2-97)$$

As we introduced earlier source terms of advection equations 2-53 and 2-54, F_A and F_{iv} are calculated by following equations

$$F_A = A^{new} - A \quad (2-98)$$

$$F_{iv} = A^{new} h_i^{new} - Ah_i \quad (2-99)$$

3. NUMERICAL ISSUES ASSOCIATED WITH ICE-POM MODEL

In this section two kinds of numerical issues have been discussed. Those are the numerical instability issue associated with collision rheology and effect of implicit correction scheme on time integral formulation.

3.1. Numerical instability in a high resolution ice-pom model

For several years ice-POM model has been used to study the sea ice behavior in a high-resolution regional model of the Sea of Okhotsk Fujisaki et al. (2010). The ice-POM simulations have given better sea ice behavior and ice edge locations than the other basic models (Simizu and Ohshima 2006; Uchimoto et al. 2007) due to the more sophisticated treatment of ice strength parameterization and subgrid-scale ice motions. However when we applied ice-POM model into the Arctic Ocean simulations, undesirable and sometimes fatal numerical instabilities occurred. The instabilities usually occurred near land, where strain rates are the largest. It is often triggered by strong winds that drive ice towards or along the coastline. Instabilities are characterized by unphysical values in the ice thickness, strength, velocity, and shear fields. In some cases the model crashes because the velocities violate the advective CFL (Courant-Friedrichs-Lewy) limit. In other cases the model stabilizes within a few days or weeks after wind or ice conditions change, leaving behind a region of un-physically thick ice as shown in Figure 3-1.

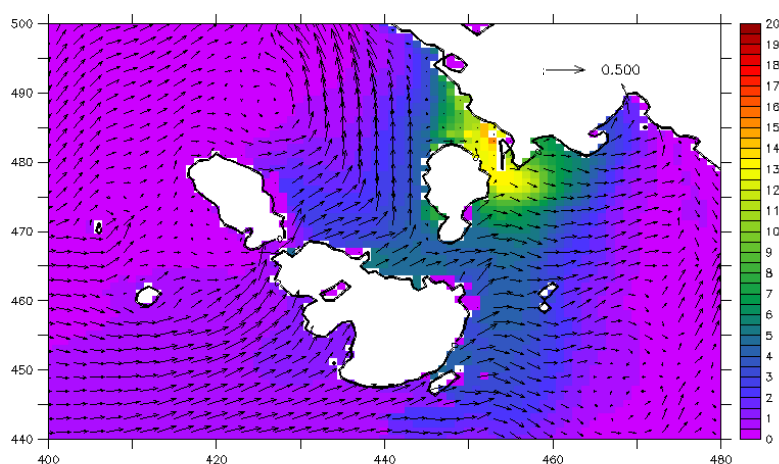


Figure 3-1 Simulated sea ice thickness [m] and sea ice velocity field [m/s] near the New Siberian Islands.

The whole Arctic simulation sea ice thickness and associated sea ice velocities are shown in Figure 3-1. Grid resolution is about 10km and surface winds are from the ERA-interim reanalysis Dee et al. (2011) dataset. The ice flow is well behaved until late March, when instability develops near the New Siberian Islands in the Siberian coast. Figure 3-1 shows snapshots of ice mean thickness in the unstable region on 1st April. In the unstable region sea ice mean thickness ranges from 0 m to 20 m and ice velocity field oscillates with grate varying magnitudes about 0 m/s to 1m/s. This behavior is unacceptable for Arctic sea route simulations. In some years model was crashed and some other years it gave excessive ice thickness near islands and coastlines. Because the instability is not always fatal, it may go undetected in long simulations. As previously mentioned; the Sea of Okhotsk simulations have not shown this unphysical behavior in old version of ice-POM model. There could be lot of reasons for this strange behavior of Okhotsk simulations and Arctic simulations; most dominant one would be that the average wind field in the Sea of Okhotsk is not against the coastlines unlike Arctic Ocean. Next one would be underneath warm ocean structure in the Sea of Okhotsk area, which speedups the ice melting before the numerical instabilities propagation.

3.1.1. Instability explained by an one-dimensional test setup

The numerical instabilities discussed in previous section can be explained in terms of a simple benchmark 1D test problem. Lipscomb et al. (2007) also described the similar numerical instability issues using 1D test setup. Their numerical model has the multi ice thickness categories and uses the ridging schemes and strength parameterization based on Rothrock (1975) and Thorndike et al. (1975). They explained the instability results from unstable feedback between their ridging scheme and the dynamics, which is triggered by large increases in ice strength between one time step and the next. However, it seems in our ice-POM model instabilities caused by the unstable feedback between ice collision rheology strength parameterization and the sea ice dynamics.

Let assume that the wind flow is in the x direction in 1D test problem, with y direction velocity component $v_i = 0$ and no variation in the y direction as shown in Figure 3-2. The east and west boundaries are closed, with $u_i = 0$ at the boundaries, and

the north and south boundaries are open and periodic. The ocean is an inert slab (Ocean currents are set to zero), but the static ocean exerts a drag on moving ice, and the Coriolis force and sea surface tilt are set to zero. There were no thermodynamic variations in the sea ice and model is on Cartesian coordinate system.

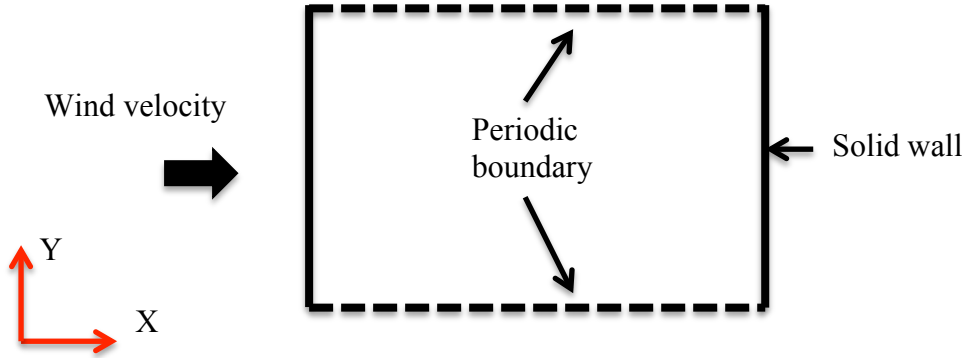


Figure 3-2 Schematic diagram of one dimensional test setup

1D test problem momentum equation on x direction is written as,

$$\frac{\partial \sigma_{11}}{\partial x} + \tau_a + \tau_w = 0 \quad (3-1)$$

where σ_{11} is x direction stress and τ_a is air to ice stress (given in equation 2-36) and τ_w ice to water stress (inert ocean) is modified by

$$\tau_w = \rho_w C_{Diw} (-u_i) \quad (3-2)$$

The strain rates in Cartesian coordinates are

$$\dot{\epsilon}_{xx} = \frac{\partial u_i}{\partial x} = D \quad (3-3)$$

$$\dot{\epsilon}_{yy} = \frac{\partial v_i}{\partial y} = 0 \quad (3-4)$$

$$\dot{\epsilon}_{xy} = \frac{1}{2} \left(\frac{\partial u_i}{\partial y} + \frac{\partial v_i}{\partial x} \right) = 0 \quad (3-5)$$

and strain rate parameter

$$\Delta = |D| \sqrt{1 + e^{-2}} = \alpha |D| \quad (3-6)$$

where α is a constant, whose value is greater than 1. The x direction internal stress σ_{11} is obtained from equations 2-40a to 2-40c

$$\sigma_{11} = \frac{P}{2} \left(\alpha \frac{D}{|D|} - 1 \right) \quad (3-7)$$

and magnitude of stress depends on the sign of strain rates (D)

$$\sigma_{11} = \frac{-P(\alpha+1)}{2}, \quad D < 0 \quad (3-8)$$

$$\sigma_{11} = \frac{P(\alpha-1)}{2}, \quad D > 0 \quad (3-9)$$

Initially ice were converging everywhere due to the eastward wind field and stresses in all grid points updated by according to the equation 3-8. The solution for sea ice velocity field near the eastern boundary was obtained by solving equation 3-1 as follows

$$u = \frac{1}{\rho_w C_w} \left(\tau_a + \left(\frac{\sigma_{11}^{i+1} - \sigma_{11}^i}{\Delta x} \right) \right) = \frac{1}{\rho_w C_w} \left(\tau_a - \frac{(\alpha+1)}{2} \left(\frac{P^{i+1} - P^i}{\Delta x} \right) \right) \quad (3-10)$$

where $i+1$ denoted the cell number at eastern boundary and i denoted the immediately adjacent to the eastern boundary.

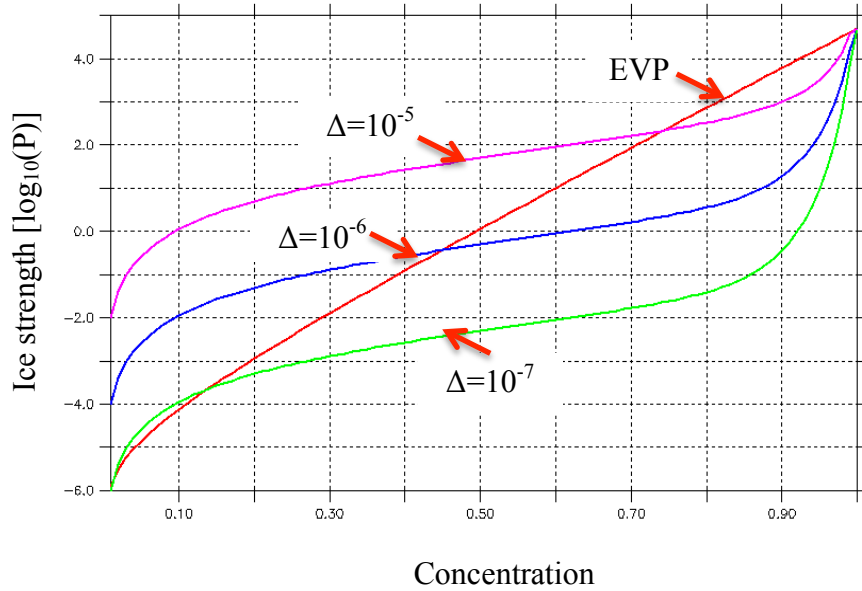


Figure 3-3 Ice strength as a function of ice concentration and strain rate parameter Δ . Old formulation

Earlier formulation of ice-POM model collision rheology ice strength is parameterized as following equations

$$P = \frac{P_{col}^* \alpha^{(1-x)} h A}{\max(A^{-1} - 1, d)} \Delta^{2x} \quad (3-11)$$

$$x = 1 - \exp(-C_{col}(1-A)) \quad (3-12)$$

$$\alpha = \frac{P^*}{P_{col}^*} d \quad (3-13)$$

Figure 3-3 has shown the sea ice strength variation of collision rheology formulation and standard EVP rheology formulation with respect to the sea ice concentration and strain rate parameters. If ice concentrations are near 100%, then ice strength P can increase substantially whatever the strain rates in our collision rheology formulation. Since ice internal stresses are functions of P , the solution for ice velocity loses its accuracy due to the sudden increment of P . Consider in a given time step, the ice strength at east boundary P^{i+1} overshoots and the stress gradient $(P^{i+1} - P^i)/\Delta x$ exceeds the wind stress; according to the equation 3-10 ice flow should be reversed in the grid cell near the east boundary ($i+1$). If the ice flow reverses, the grid $i+1$ become divergence ($D>0$) and the solution for momentum equation changes near eastern boundary grid as follows. Please note that upstream grid cells are converging ($D<0$) due to the wind stress.

$$u = \frac{1}{\rho_w C_w} \left(\tau_a + \frac{1}{2\Delta x} [(\alpha - 1)P^{i+1} + (\alpha + 1)P^i] \right) \quad (3-14)$$

However in next time step the velocity should be positive, as the right-hand side of the equation 3-14 is positive. Therefore ice flow field again become converging and velocities are given in equation 3-10. But during this oscillation process the magnitude of P is not changed therefore once again stress gradient exceeds the wind stress and ice flow has to be reversed and diverging. If this process continues the ice flow field becomes oscillating near the solid boundaries and neighboring grid cells. If the numbers of EVP cycles are large enough (small time steps) the oscillation damps down and is restored toward the true solution. Otherwise oscillations are amplified and model produces the unphysical thick ice and oscillating ice flow fields.

3.1.2. Remedies for instability issue

Instability issue discussed in previous section is fundamentally numerical and triggered due to the sudden increment of ice strength at the 100% concentration. But in real physical process of floe collision, Sagawa (2007) on his bunch collision theory and Shen et al. (1986) on the theory of random fluctuation in ice velocity have shown that floe collision becomes maximum at the ice concentration equivalent with maximum compactness (about 90% concentration). But unfortunately in our old formulation ice floes were collided even at the 100% concentration. Therefore we have changed the old collision rheology formulation equations 3-11 to 3-13 to adopt the maximum floe collision concentration to 90% as follows:

$$P = \frac{P_{col}^* \alpha^{(1-x)} h A}{\max\left(A^{-1} - \frac{2\sqrt{3}}{\pi} \gamma^{-1}, d\right)} \Delta^{2x} \quad (3-15)$$

$$x = 1 - \exp\left(-C_{col} \left(\frac{\pi}{2\sqrt{3}} \gamma - A\right)\right) \quad (3-16)$$

$$\alpha = \frac{P^*}{P_{col}^*} d A_{\max} \exp(-C(1 - A_{\max})) \quad (3-17)$$

The equations 3-15 to 3-17 change the ice strength P with respect to the ice strain rates and ice concentrations as shown in Figure 3-4. This physically realistic modification allows the ice strength to relax when concentrations greater than 90% (ice strength P is equal to EVP formulation ice strength). Not only collision rheology but also we have changed the elastic parameter definition in EVP constitutive relationship to enhance the elastic wave damping as follows.

In standard EVP scheme Hunke and Dukowicz (1997) constitutive relationship is defined according to the,

$$\frac{1}{E} \frac{\partial \sigma_{ij}}{\partial t} + \frac{1}{2\eta} \sigma_{ij} + \frac{\eta - \xi}{4\eta\xi} \sigma_{kk} \delta_{ij} + \frac{P}{4\xi} \delta_{ij} = \dot{\epsilon}_{ij} \quad (3-18)$$

and elastic parameter E is defined as

$$E = \frac{2E_0 \rho_i A h}{\Delta t_e^2} \min(\Delta x^2, \Delta y^2) \quad (3-19)$$

that can vary in time and space. But later Hunke (2001) introduced the new EVP scheme by changing elastic parameter shown in equation 3-20. This new modification can damp the elastic wave more quickly and efficiently compare to the previous method

$$E = \frac{\zeta}{T} \quad (3-20)$$

where ζ is bulk viscosity. In the new EVP scheme the stresses and velocities are sub-cycled 120 times per time step, and elastic waves are damped on a timescale $T = 0.36 \Delta t$, which gives excellent accuracy and stability in ice-POM model under most conditions.

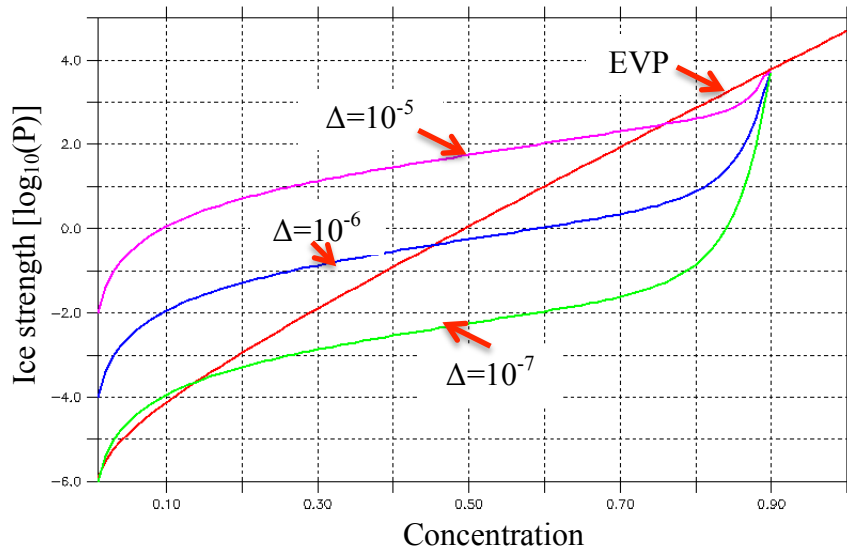


Figure 3-4 Ice strength as a function of ice concentration and strain rate parameter Δ . New formulation

Since the 1D problem is somewhat artificial, we introduce a complementary test problem in two dimensions to test the new modifications. As shown in Figure 3-5 two-dimensional setup has north-south and east-west open boundaries with periodic boundary condition. In the center of the grid, there is an L-shaped Island whose legs are rotated so that the legs open toward the southwest. The ice is forced with a uniform southwesterly wind with components $u = v = 10$ m/s, giving a wind speed of 14.1 m/s. As for initial conditions, homogenies 5m thick ice with 80% concentration is specified.

In Figure 3-6 the left hand side (a to d) has shown the old formulation ice thickness and associated velocity near the L-shape Island. After the first week of old formulation, unstable ice flow develops upwind of the island where the ice pack converges. Later instabilities soon spread over a large region and had produced the thick sea ice and noisy velocity field near the L shape island. On the other hand (e to h) in the modified new version sea ice converged nicely and ice flow field was damped throughout the computation period.

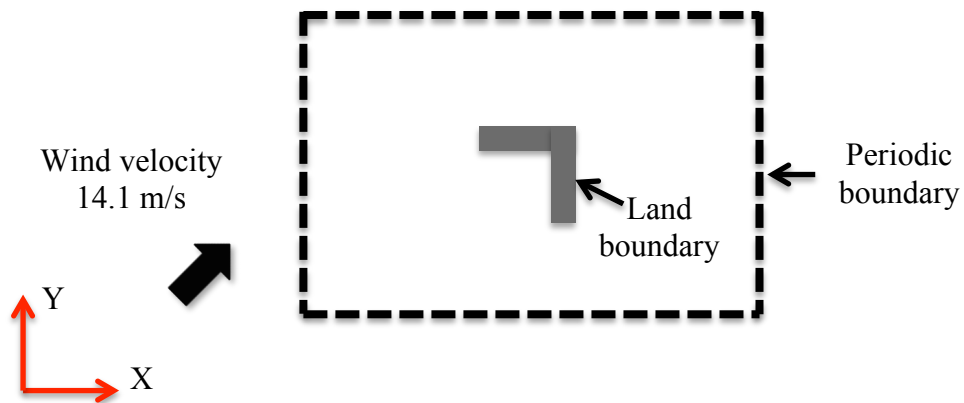


Figure 3-5 Schematic diagram of two-dimensional test setup

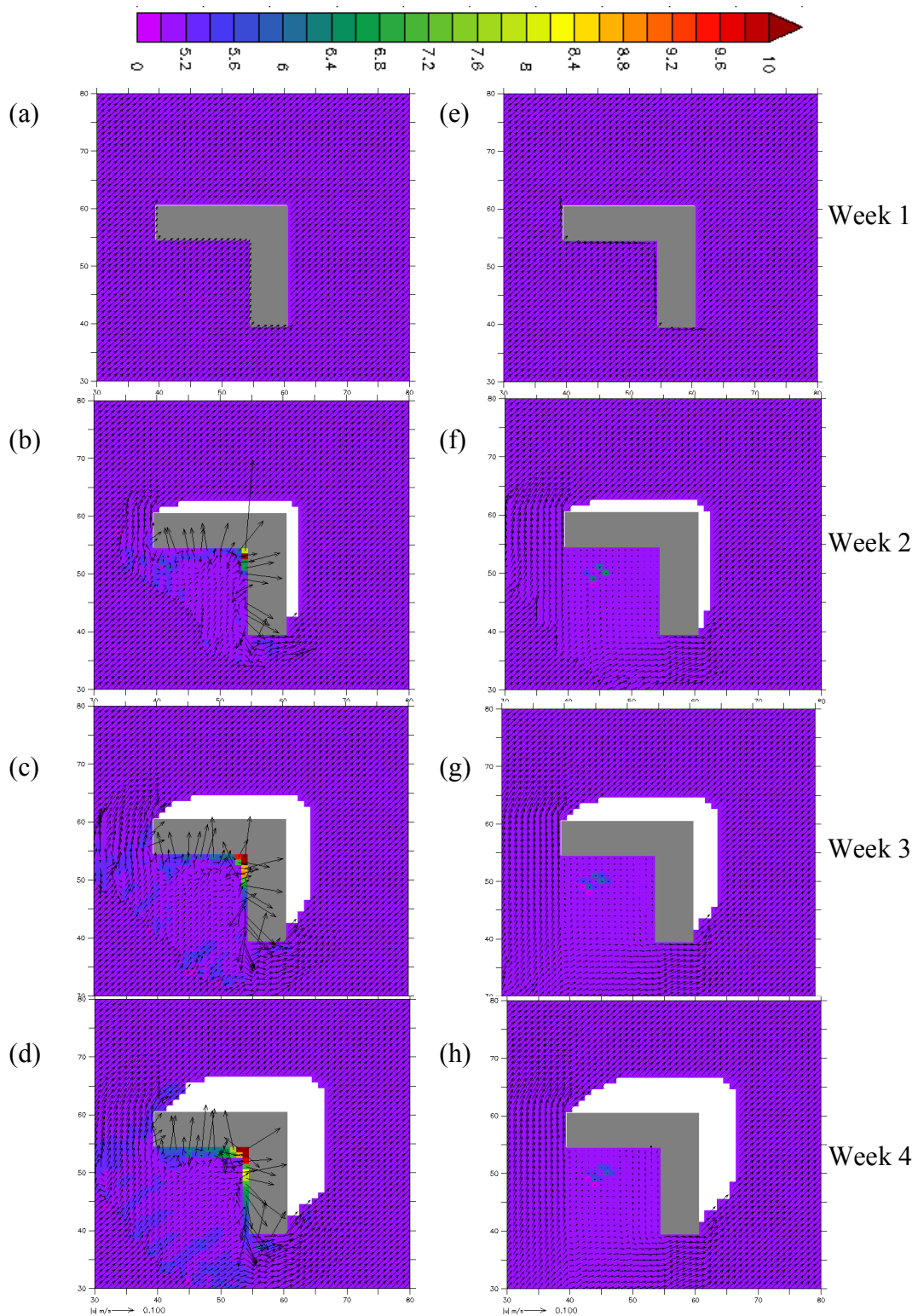


Figure 3-6 Sea ice thickness [m] and associated ice velocity [m/s] variation in two-dimensional test model. (a-d) left-hand side shows the old formulation of ice-POM model ice variation 1st week to 4th week. (e-h) right hand side shows the new formulation of ice-POM model ice variation in the same time duration

3.2. Effect of implicit correction in ice-POM model

Earlier version of the ice-POM model used the forward Euler explicit discretization for time integral of momentum equations. That makes the model produce unrealistic results when dealing with extreme weather events. Because Euler explicit discretization did not properly update the Coriolis force term and ocean drag force term. Equation 3-21 represents the Euler explicit time discretization of sea ice momentum equation.

$$\rho_i h A \left(\frac{u_i^{n+1} - u_i^n}{\Delta t} \right) = \left(\frac{\partial \sigma_{ij}}{\partial x_j} \right)^k + A \tau_{ai}^n + A \tau_{wi}^n + \varepsilon_{ij3} \rho h A f u_j^n - \left(\rho h A g \frac{\partial H_o}{\partial x_i} \right)^n \quad (3-21)$$

where, k , n represent the EVP sub-cycled time step and ice dynamics time step. Only internal stress is sub-cycled (using the small time step k) and other forcing terms were updated by using the value of previous dynamics time step (n) in the Euler explicit method. Because of the explicit discretization there is a limit for the time step in Von Neumann stability criteria as shown in equation 3-22.

$$\Delta t < \frac{2\rho_i h}{C_{Dwi} \rho_w |U_w - u_i^n|} \quad (3-22)$$

If this limiting value is smaller than the model integration time step, updated velocities are highly inaccurate and numerical errors are accumulated with integration. To avoid this time constraint in ice-POM model we have discretized the Coriolis and ocean stress terms using implicit time integral method as follows:

$$\rho_i h A \left(\frac{u_i^{n+1} - u_i^n}{\Delta t} \right) = \left(\frac{\partial \sigma_{ij}}{\partial x_j} \right)^k + A \tau_{ai}^n + A \tau_{wi}^k + \varepsilon_{ij3} \rho h A f u_j^k - \left(\rho h A g \frac{\partial H_o}{\partial x_i} \right)^n \quad (3-23)$$

in the now implicit time discretization equation 3-23 internal ice stress gradient, ocean to ice stress and Coriolis force terms are sub-cycled using the small time step (k) and air to ice and sea surface tilt force are updated using previous ice dynamics time step (n). Even though this implicit correction gives us the additional computational expenses we can increase the model integration time step significantly (3 or 4 times larger) compare to the previous explicit time step. Therefore overall computational cost is compensated.

Figure 3-7(a) shows the old explicit method sea ice concentration on year 2000 August 01st and Figure 3-7(b) shows the new implicit correction method sea ice concentration on the same day. As we have discussed earlier due to the violation of stability time limit in explicit method sea ice has shown the scattered distribution. On the other hand implicit formulation has shown the reasonable distribution with satellite observations as shown in Figure 3-7(c). In the summer time this instability is triggered because of the extreme weather events (cyclones) commonly seen in the Arctic. Because of our old explicit time discretization method velocities were not updated properly (especially in the center of Arctic) compared to the pathfinder observational data as shown in Figure 3-8 (a) and (b). But with our new implicit formulation updated velocities are closer to the observation Figure 3-8(c).

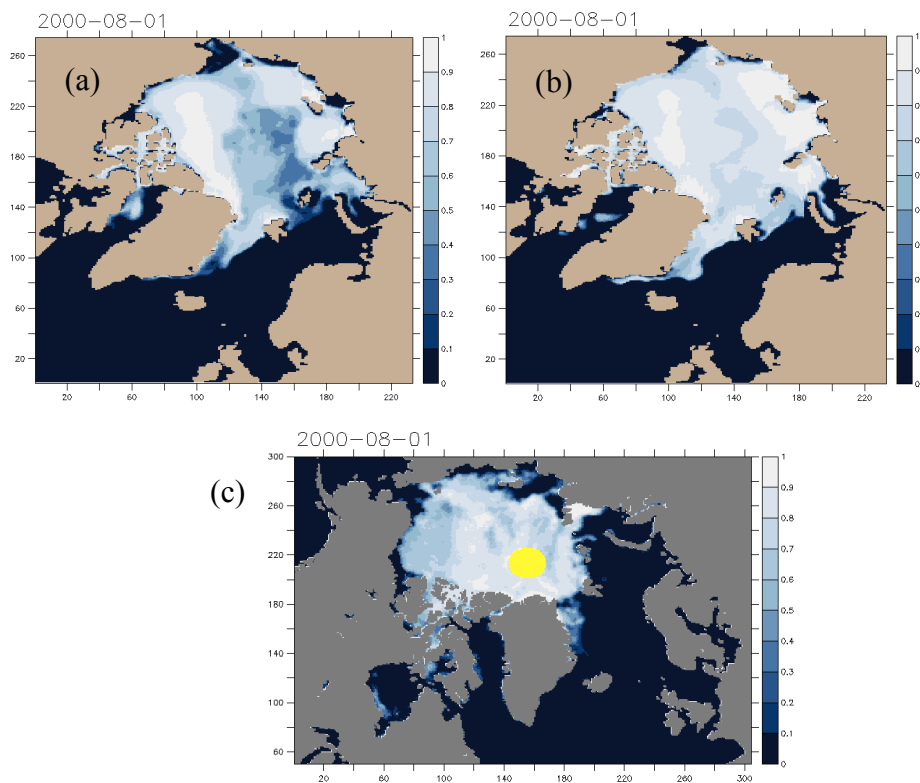


Figure 3-7 Sea ice concentration on 2000-August-01 (a) old explicit time integral formulation (b) new implicit correction formulation (c) satellite derived SSM/I observational

Due to the extreme weather undamped high velocities (because of old explicit discretization) move and converge the sea ice into neighboring grids. If the ice is broken up, the areas of open water between floes absorb a great deal of solar energy

in summer. That energy can be transferred both to the sides of the floes and underneath the floes, promoting further melt. But in wintertime even though ice velocities move into the neighboring cells frozen ocean quickly produce the ice in the open ocean and does not show the scattered nature like in summertime.

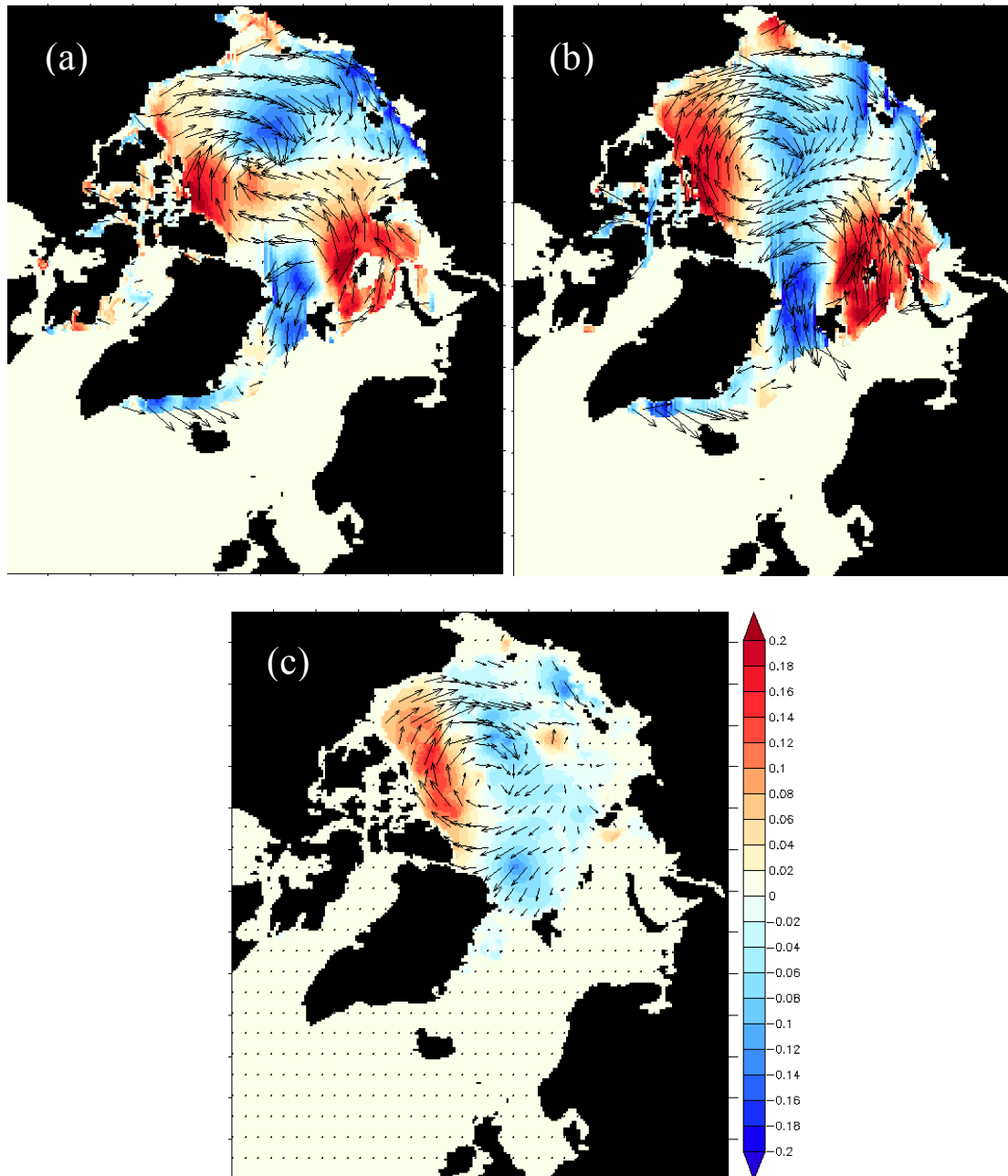


Figure 3-8 Meridional sea ice velocity (v) and sea ice velocity vector on 2000-August-01 (a) old explicit time integral formulation (b) new implicit correction formulation (c) satellite derived Pathfinder observational

4. WHOLE ARCTIC MODEL SIMULATION

Recently profound changes have been occurring in the Arctic. Therefore it's reasonable to check our ice-POM model's reproducibility for those changes. To understand the model reproducibility and recent overall Arctic behavior, we have setup the whole Arctic model simulation. We also planned to use the whole arctic model results for our regional model (ASR regions) as initial and boundary conditions. The whole Arctic model domain contains the entire Arctic Ocean, the Greenland-Iceland-Norwegian (GIN) seas and the North Atlantic Ocean as shown in Figure 4-1. The bathymetry is constructed from Earth Topography one-minute Gridded Elevation Dataset (ETOPO1) Amante and Eakins (2009). The horizontal resolution is about one-fourth degree (about 25km) in the rotated spherical coordinate system. And there are 33 vertical sigma layers as shown in Table 2-2. The atmospheric forcing components are constructed from the ERA-interim project six hourly databases.

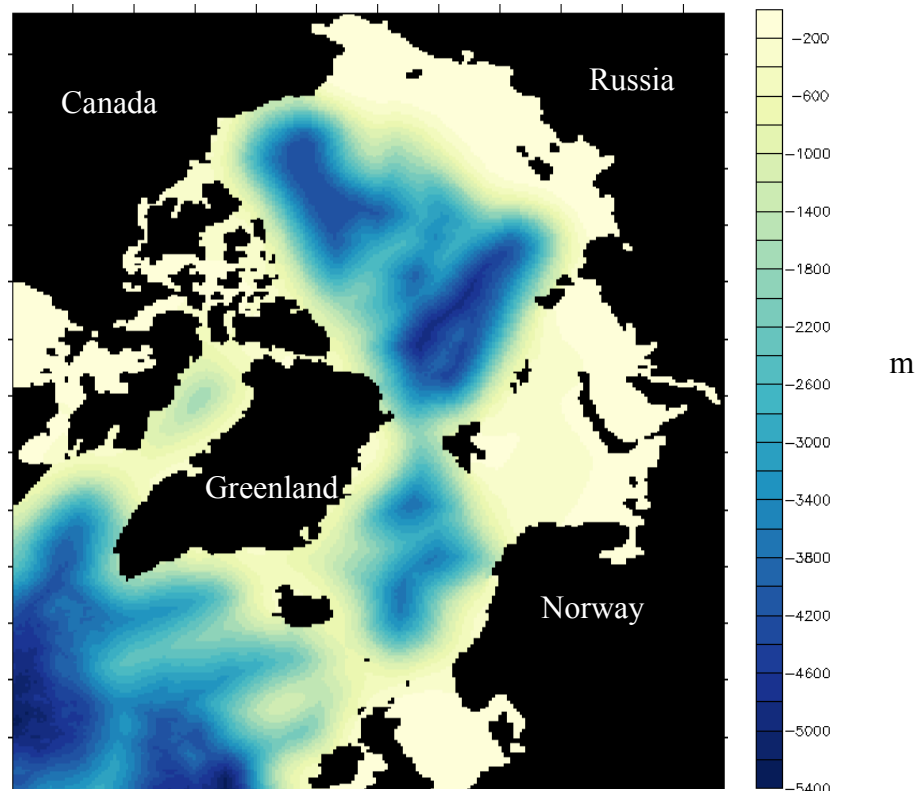


Figure 4-1 Whole arctic model bathymetry in meters

The Pacific water inflow with sinusoidal seasonal cycle is provided at the Bering Strait based on the hydrographic observation of Woodgate (2005). The annual mean inflow and salinity of the Pacific water at the Bering Strait are set to be 0.8 Sv (Sverdrup) and 31 psu, respectively. The inflow reaches maximum in June and minimum in December and its seasonal amplitude is 0.4 Sv. The salinity reaches maximum in March and minimum in September and its seasonal amplitude is 1 psu. The temperature is kept at freezing point from January to June, and reaches maximum (5°C) in September. Note that in the present version of ice-POM model we have not yet included the river runoff into the model. In the marginal regions of model domain radiation boundary condition is applied and at the costal regions and around islands no-slip boundary condition is adopted.

The time integration started from the steady state with a climatological temperature and salinity field provided by Polar science center Hydrographic Climatology (PHC3.0) Steele et al. (2001). First, model was spun up for 15 years by providing the year 2000 atmospheric data cyclically. Entire model domain reached the equilibrium after the 15 years spin up. Then the model is integrated from year 2000 to 2012 with ERA-interim realistic atmospheric forcing.

After simulating this 11 years experiment we have compared our simulated sea ice concentrations, ice thickness, sea ice velocities and ocean structure with available observations. The results are shown in the following subsections.

4.1. Comparison of sea ice concentration and extent reproducibility with satellite derived observations

Sea ice concentration is a fundamental property of the Arctic ice-ocean-atmosphere system reflecting both dynamics and thermodynamics. Arctic sea ice underwent profound changes in recent years; The annual mean sea ice extent decreased by $-3.7\% \pm 0.2\%$ /decade between 1979 and 2007 with an enhanced negative trend of $-10.1\% \pm 0.7\%$ /decade between 1996–2007 Comiso et al. (2008). To understand the better interannual behavior of the observed and computed sea ice, we have analyzed the year 2001 to 2012 sea ice extents. For the comparison we have disregarded the grid cells that has concentration less than 15%. Also to be consistent with model data, satellite derived Advanced Microwave Scanning Radiometer for Earth Observing System (AMSR-E) data sets are interpolated into the same numerical model domain. For the interpolation inverse distance method is used. Figure 4-2 has shown the daily sea ice extent comparisons with observations. It seems that our model captures the major features of observed sea ice concentration properties including larger decreases in the years of 2007 and 2011. The model and observation correlation coefficient is 0.98, although our model slightly underestimates the sea ice extents in summer seasons. Finally we can conclude that the overall agreement is quantitatively reasonable with the satellite observations.

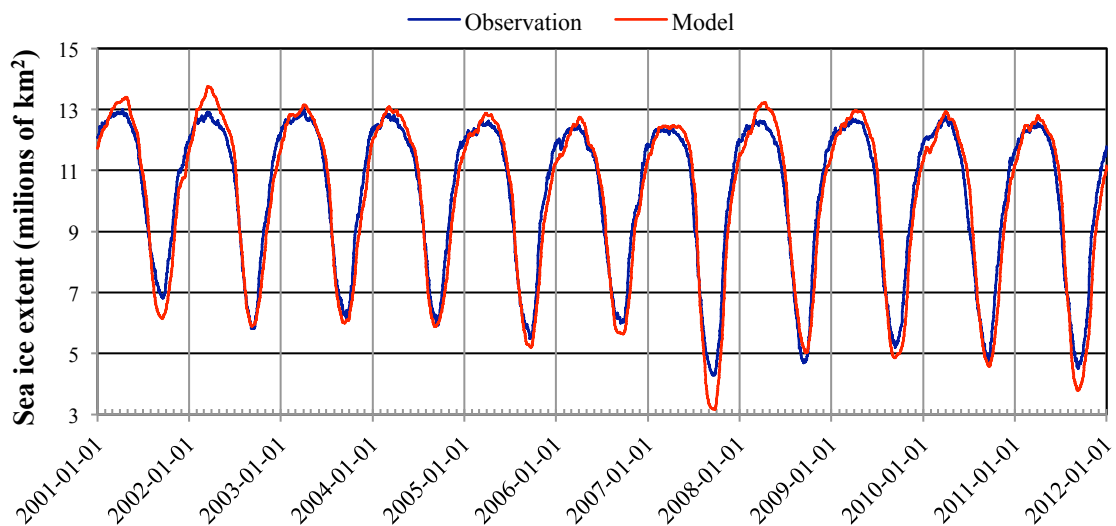


Figure 4-2 Daily time series of model and satellite observation ice extent from year 2001 to 2012

Figure 4-3 (a) and (b) show the September mean model sea ice concentration comparison with corresponding months observational sea ice concentrations obtained from Hadley Centre Sea Ice and Sea Surface Temperature data set (HadISST). By looking at the qualitative comparison shown in Figure 4-3 following observations are made. Overall agreement of model simulated and observational September Arctic sea ice concentrations are quantitatively reasonable. The negative trend of September Arctic sea ice extents, year 2007 minimum sea ice concentrations, and year 2005 opening of the Northeastern Passage are well captured with simulated results.

However we have believed that the reason for discrepancy of the model and the observation sea ice extent is due to the simplified thermodynamics model (especially constant albedos and disregards of melt pond), coarseness of model grids and lack of reproducibility of multi year high thickness ice in our model (will be discussed in section 4.2). However overall agreement in concentrations and extents are reasonable with observations.

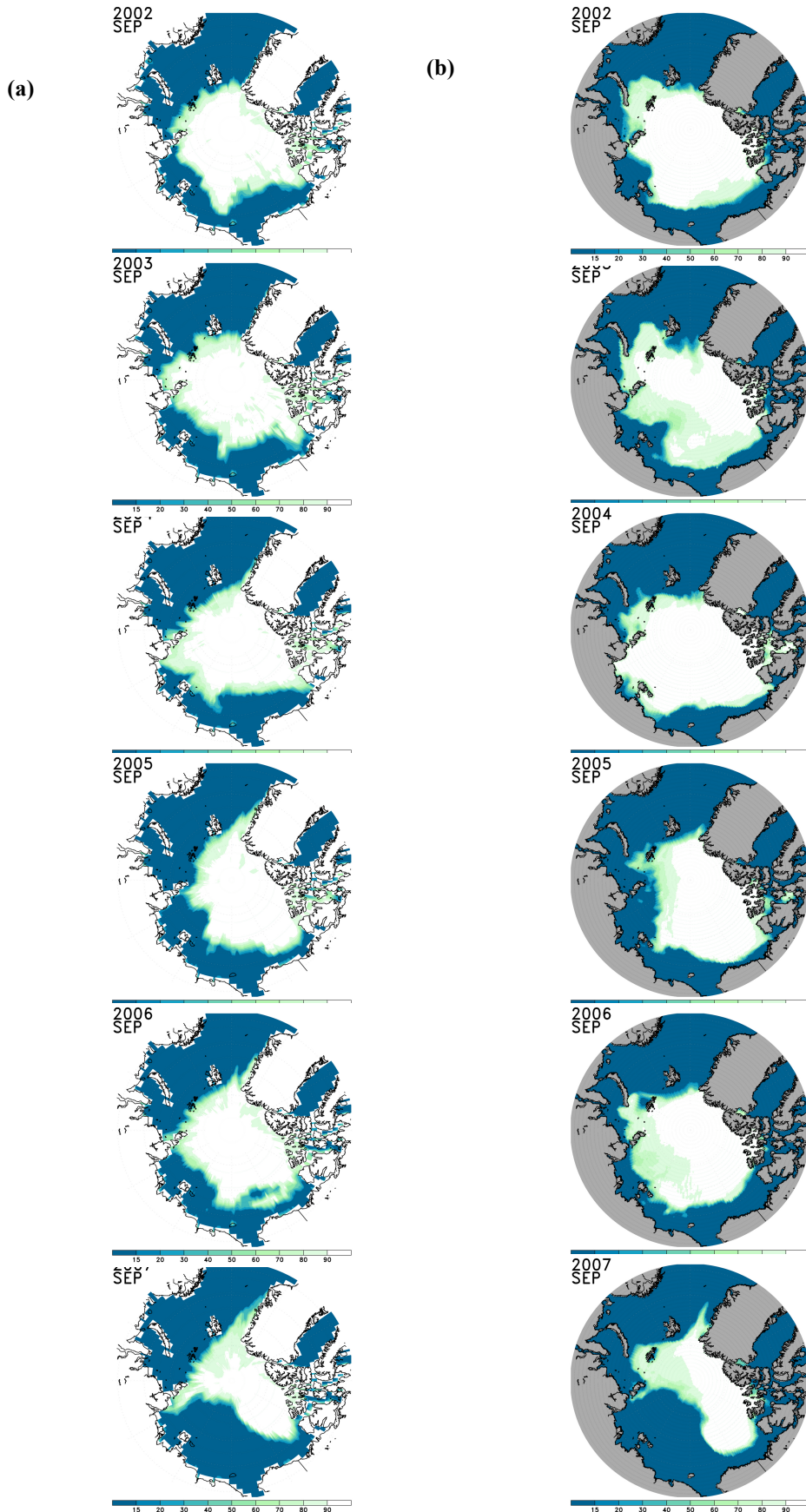


Figure 4-3 September mean sea ice concentration from year 2002 to 2007. (a) HadISST observational concentration. (b) Numerical model predicted concentration

4.2. Comparison of sea ice thickness between model computations and observations

The annual mean sea ice extent is decreasing rapidly as seen in previous sections. Sea ice thickness is also decreased by 1.6 m or 53% for the ICESat satellite period (2003–2008) compared to early submarine measurements between 1958–1976 Kwok and Rothrock (2009). During the 2003–2008 period, Arctic sea ice volume decreased by 42% and 21% for fall (Oct/Nov) and winter (Feb/Mar), respectively Kwok et al. (2009).

The focus of this section is the ability of ice-POM model to simulate sea ice thickness and to identify trends and differences with observations. The observational data is derived from freeboard (ICESat), indirect measurements of thickness (airborne electromagnetic), thickness computed from ice draft (moorings and submarines), and thickness measured directly (drill holes). The ICESat retrieval algorithm measures ice freeboard thickness by comparing the satellite distance from the snow or ice surface to that of ice-free areas. Freeboard measurements are then converted to ice thickness using a sequence of processing steps discussed in Kwok et al. (2009). The data used in this study is available from the new Unified Sea Ice Thickness Climate Data Record Lindsay (2010). There are currently over 3000 samples in the archive, which can be accessed along with documentation. Figure 4-4 has shown the thickness data locations in the Arctic Ocean.

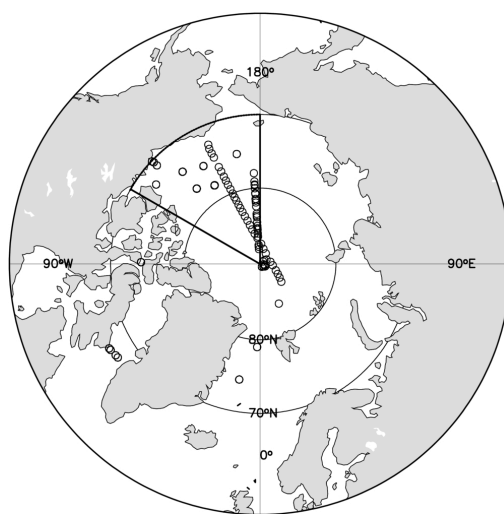


Figure 4-4 Observed ice draft locations Lindsay (2010) from year 2001 to 2011

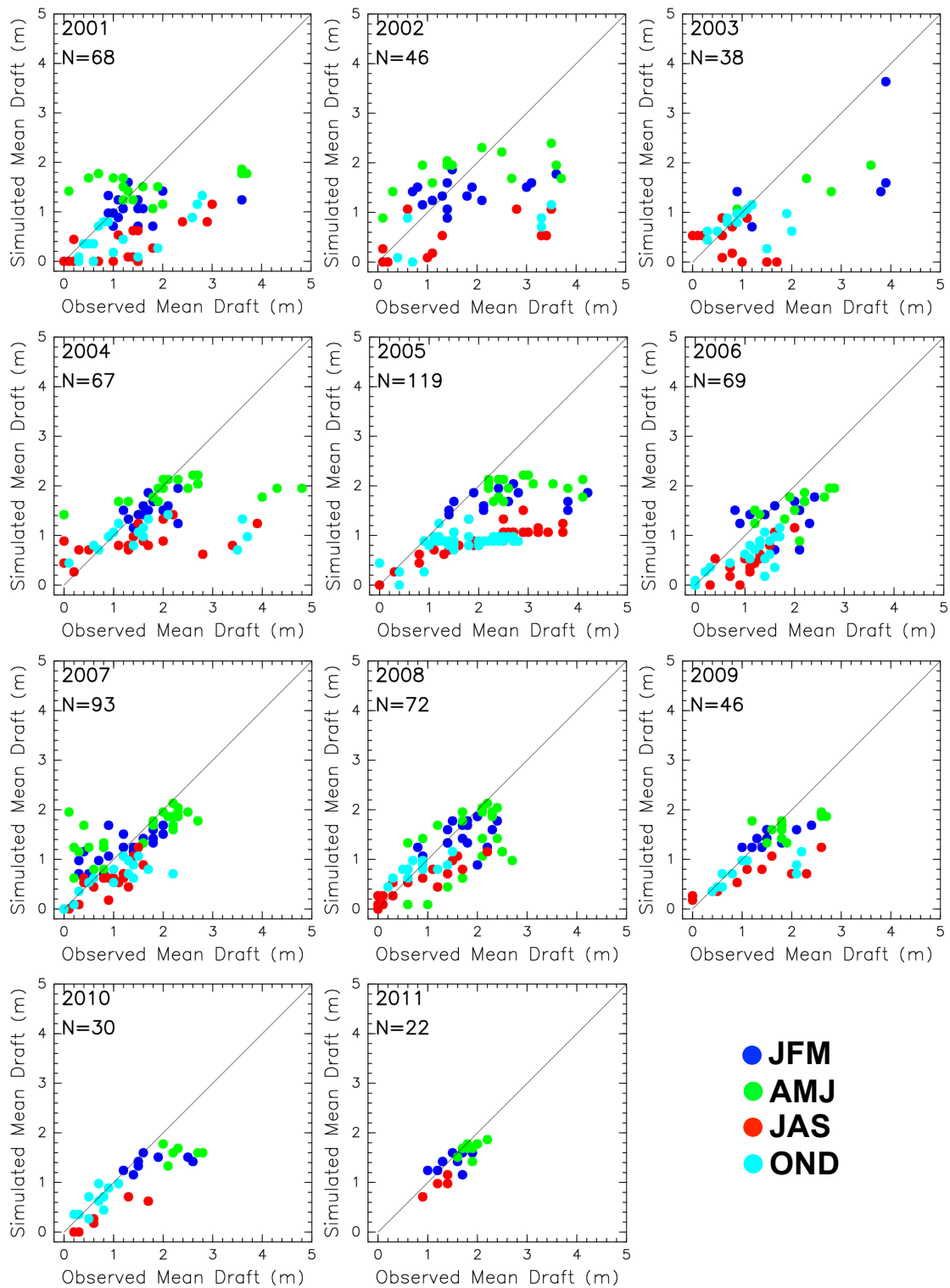


Figure 4-5 Inter-annual and seasonal comparisons between observed Lindsay (2010) mean ice draft and computed model ice draft in all four seasons; Winter (JFM), Spring (AMJ), Summer (JAS), Fall (OND) of year 2001-2011.

The scatter diagram between modeled and observed thickness is shown in Figure 4-5 from year 2001 to 2011. The blue dots denote the winter data points (JFM), green dots denote the spring (AMJ), red dots denote the summer (JAS) and light blue dots denote the fall (OND) respectively. As shown in Figure 4-5 the uncertainty between the model and observation thickness data has become significant in summer and fall. On the other hand in winter and spring the correlation between modeled and observed thicknesses is fairly reasonable with each other. On the other hand by looking at the figures we can clearly see that after the year 2006 our model and observations reasonably reproduced the sea ice thickness with high correlations. Also it can be seen that our model significantly underestimated the thick ice, where ice thickness (>2m). Next we have compared the overall and seasonal variation between observations and simulated thicknesses from year 2001 to 2011. As shown in Figure 4-6 the overall agreement between the model and simulation is reasonable. As for the conclusion of this qualitative analysis, we can conclude that our model is reasonably predicting the thin ice (<2m) and somewhat underpredict the thick ice (>2m).

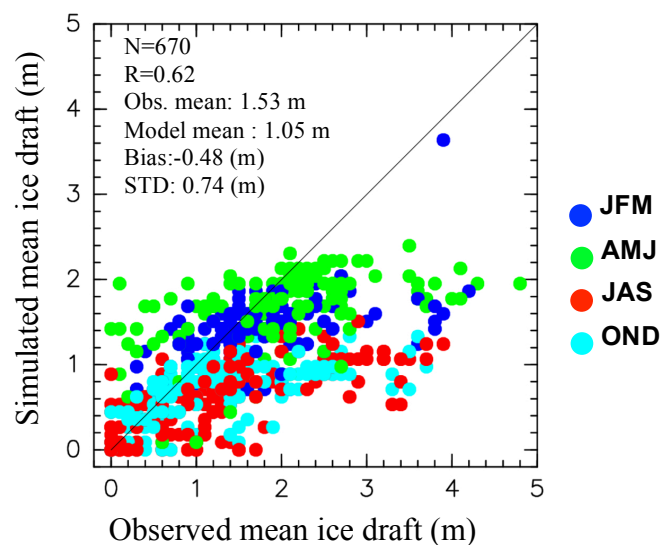


Figure 4-6 Overall comparisons between observed mean ice draft Lindsay (2010) and computed mean ice draft in all four seasons Winter (JFM), Spring (AMJ), Summer (JAS), Fall (OND) of year 2001-2011.

Our quantitative comparison has revealed that ice-POM model cannot be used to reproduce the thick ice (>2m). But in the quantitative analysis data points are rather biased to the Canada basin and couldn't represent the overall Arctic sea ice thickness behaviors. Therefore we have compared the observational ICESat gridded data with our ice-POM model results. These observational ice thickness fields are generated from ten ICESat campaigns during October-November 2003-2007 and March-February 2004-2008. In this study for direct comparison with ice-POM thickness, observational ICESat ice thicknesses were regridded to the ice-POM grid using the nearest neighbor inverse distance interpolation method as shown in equation 4-1. Different maps were computed for spring and fall as shown in Figure 4-7.

$$F(i, j) = \frac{\sum_{k=1}^4 \frac{1}{d(l, m, k)} F_0(l, m, k)}{\sum_{k=1}^4 \frac{1}{d(l, m, k)}} \quad (4-1)$$

where, $F(i, j)$ is a interpolated value on 2D space, $d(l, m, k)$ is shortest distance between interpolated point and sample point, $F_0(l, m, k)$ is a sample value at the shortest distance. In the inverse distance interpolation first calculate the distances between interpolated (arbitrary) point and sample points. Then chose the 4 nearest neighbors among the sample points. Finally those 4 points are weighted with inverse distance as shown in equation 4-1.

According to the Figure 4-7 (a,b,c,d) ICESat and model ice thickness fields show a close agreement with the overall pattern of ice thickness. Ice-POM model largest under predictions of ice thickness and meridional gradients occurs in a narrow band along the northern coast of Greenland and the Canadian Archipelago. As we have already discussed at the current configuration with two-thickness category, coarser resolution grid, ice-POM model seems to have trouble reproducing the thick ice along the Canadian coast, contributing to the negative bias results. However, if we can increase the grid resolution and subgrid-scale thickness categories we can obtain the better results in future.

Interestingly in the areas of both Arctic sea routes (Northeast and Northwest Passages) the sea ice thickness error compared to the ICESat observational is small (about 0.5m). This thickness error is almost equal with the ICESat observational

uncertainties Kwok et al. (2009). Therefore, considering all the in situ Lindsay (2010) and gridded (ICESat) sea ice thickness comparisons, we can conclude that our coarser resolution whole Arctic model ice thickness results can be used as initial and boundary conditions for our regional high-resolution models.

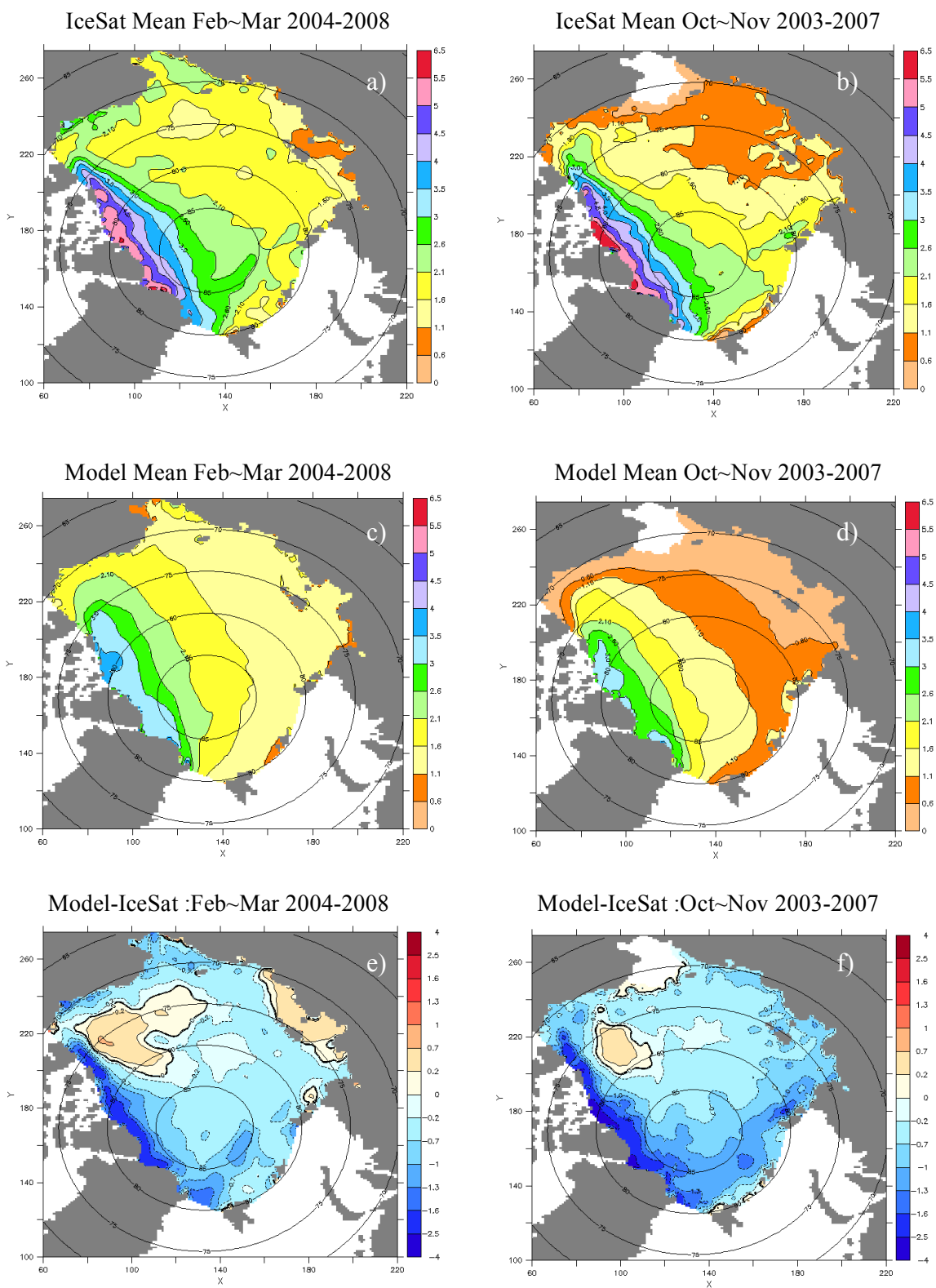


Figure 4-7 Mean 2003-2008 (a,b) ICESat and (c,d) Model thickness for February-March (a,c) and October-November (b,d). (e,f) Differences of thickness maps are shown. The scale is given in [m].

4.3. Sea ice drift variability in the Arctic Ocean model and observation

In the above sections we have discussed about the recent changes of sea ice concentration and thickness in the Arctic Ocean. Many researchers believe those changes are accompanied by an increase in the sea ice drift speeds, as seen in drifting buoys results. Rampal et al. (2009) reported an overall increase of the mean Arctic drift speed of 0.6 cm/s/decade for the 1979–2007 period. The winter buoy speed has increased by 17% per decade and the summer speed by 8.5% per decade. Meantime Hakkinen et al. (2008) observed an increase in Central Arctic drift speed since 1950 using combined buoys and drifting ice stations datasets.

The spatial distribution of sea ice is an important process in climate system. The formation of leads, ridges and polynyas are mostly due to the movement of sea ice. Moreover the position of ice edge that depends on the supply of sea ice from the interior ice pack is also highly influenced by the ice motion. Ice edge position is very impotent parameter for navigation in Arctic sea routes. Therefore ice drift is an important parameter that should be reproduced correctly in sea ice modeling. In this section we compare and analyze the model-derived and observed sea ice velocities.

Emery et al. (1997) has developed a method to derive the ice drift speed from successive satellite imagers. We use the daily sea ice drift computed by Kimura and Wakatsuchi (2000), from AMSR-E satellite imagers using the above method and buoy velocity data from International Arctic Buoy Program (IABP). Satellite product has the spatial resolution of 37.5km in winter months from December to April and 75km in summer months from May to November for period of 2003 to 2011.

The satellite-derived data are not direct observations and are afflicted with considerable uncertainty. Therefore in our statistical analysis we have additionally included raw position data of buoy of the IABP. Although the buoys data set has rather poor spatial coverage, 30 to 40 buoys with a spacing 300-600 km are available each year; it represents the most accurate drift measurements that are accessible at the moment. The spatial coverage of the buoys is most dense in the central Arctic Ocean and in the Beaufort Sea areas but sparse in the Eurasian marginal seas.

To characterize the sea ice drift properties in the numerical model we rely on histograms of sea ice drift speed and maps of sea ice drift for certain situations. The seasonal histograms for the period 2004 - 2010 are shown in Figure 4-8, drift speeds below 0.5 cm s^{-1} have been discarded.

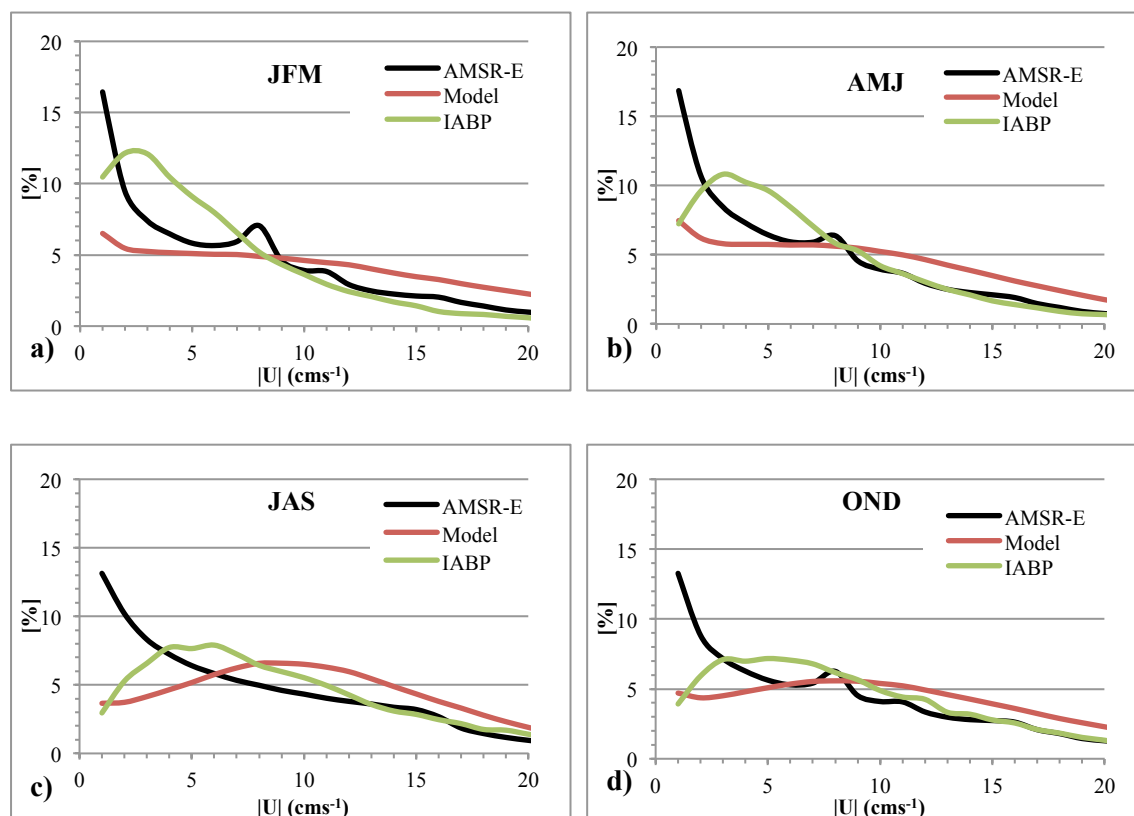


Figure 4-8 Seasonal histograms (a) January – March, (b) April – June, (c) July - September, and (d) October–December of sea ice drift speed of the Arctic for the period 2004–2010. Corresponding distribution of observation drift speed computed from daily AMSR-E satellite products and IABP program have been included. Bin width is 1 cms^{-1} . Bin start from 0.5 cms^{-1}

In all four seasons model has a much higher frequency of occurrence at speed between 8 and 20 cm s^{-1} compared to the satellite derived velocities and IABP buoys observations. This overprediction is rather obvious that our model has underpredicted the thicker ice along the Canadian coast (discussed in chapter 4.2).

Ice motion is mainly forced by the wind and, to a lesser degree, the ocean currents and the internal ice stresses. These factors are controlled by the thickness, deformation, and compactness of the ice cover and numerical parameters such as ice

strength parameter P^* and lead closing parameter h_0 . In the Hibler's formulation of ice strength, which is an exponential function of concentration, is sensitive to the ice concentrations (specially concentrations greater than 90%). We have found that our model average concentration is not larger than 97% even in winter. This low concentration highly influenced the underprediction of sea ice strengths and ultimately affected the overprediction of sea ice speed in our model.

AMSR-E derived data has shown high frequency of occurrence compared to the ice-POM model in low speeds (less than 4 cm s^{-1}) and the velocity distribution is rather flat in the range of $4 - 8 \text{ cm s}^{-1}$ and well agreed with model results. In the summer season model histogram has shown the Gaussian distribution with the mean of 10 cm s^{-1} . Furthermore, in summer and fall buoy data and model data has shown a similar trend with each other but in winter and spring the model underpredicted the small velocities considerably. Reason for this discrepancy is due to the spatial distribution of buoy locations. Most of the buoys are located in the Canada basin and has shown the more bias towards low velocities in the winter. Therefore we believe the discrepancy is due to the bias of the location than model errors. However the model reproduces the trend of histograms reasonably with the observations.

To evaluate the velocity errors in our numerical model, we further compared the model-derived ice velocity with buoy position data from the IABP. Figure 4-9 shows some of buoy trajectories from 2004 January 01 to 2004 December 31. Yellow arrows denote the buoy trajectories that we have compared with our model results in this study. To cover the whole Arctic areas we have chosen the buoys that are situated all over the Arctic as seen in Figure 4-9. Figure 4-10 shows the scatterplots of daily model-derived ice speed versus buoy speed for zonal (U) and meridional (V) components, respectively. For this comparison, ice-POM model ice velocities at each buoy positions are evaluated by using the weighted average Gaussian interpolation method as shown in equation 4-2.

$$F(i, j) = \frac{\sum_{k=1}^K F_0(l, m, k) \exp\left(-\frac{d^2(i, j, k)}{D_c}\right)}{\sum_{k=1}^K \exp\left(-\frac{d^2(i, j, k)}{D_c}\right)} \quad (4-2)$$

where, $F(i,j)$ is a interpolated value on 2D space, $d(i,j,k)$ is distance between interpolated (arbitrary) point and sample point, D_c is a Gaussian radius being set to 50km in this study, $F_0(l,m,k)$ is a sample value at the evaluated point. In the Gaussian interpolation first search the sample points which inside the given circle of radius D_c . Then those points are weighted with the Gaussian weighting function as shown in equation 4-2.

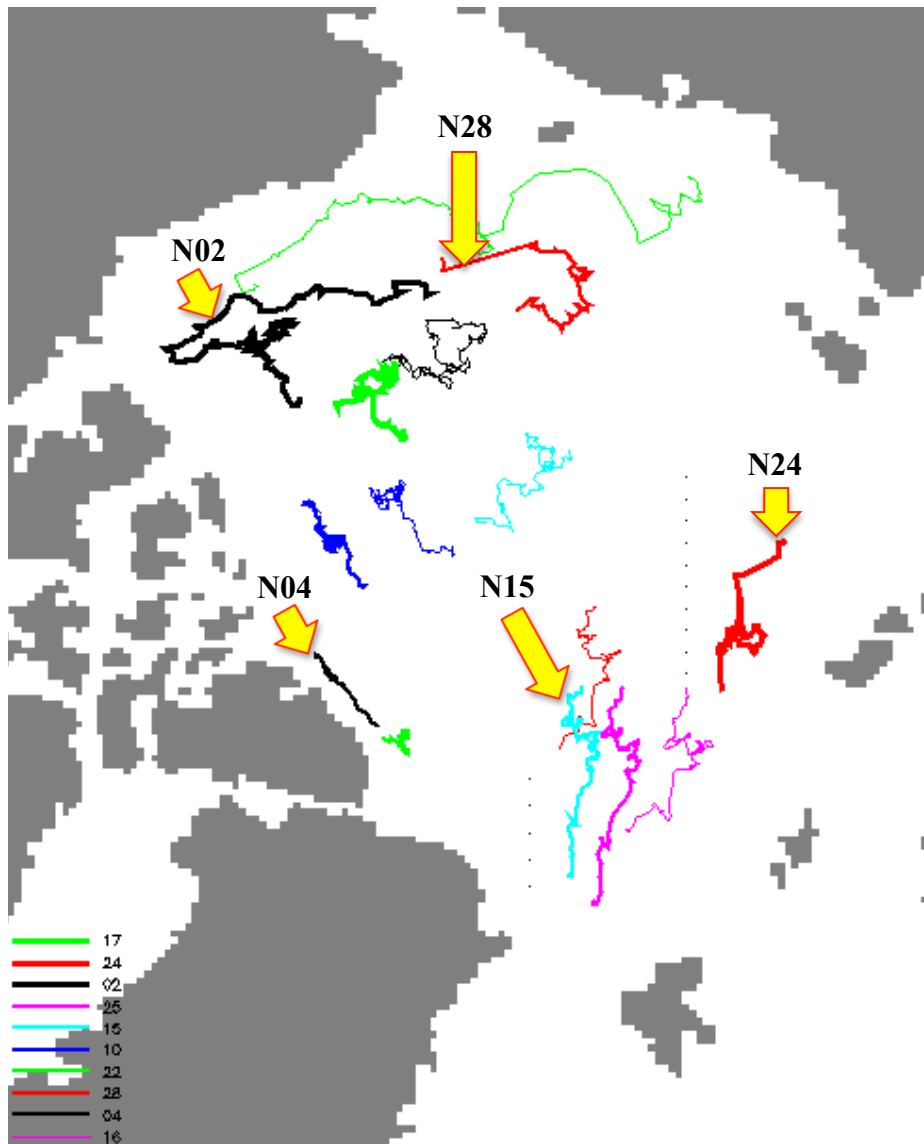
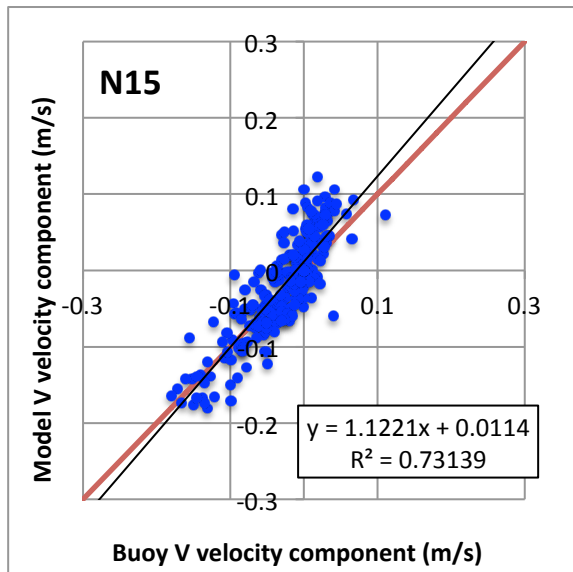
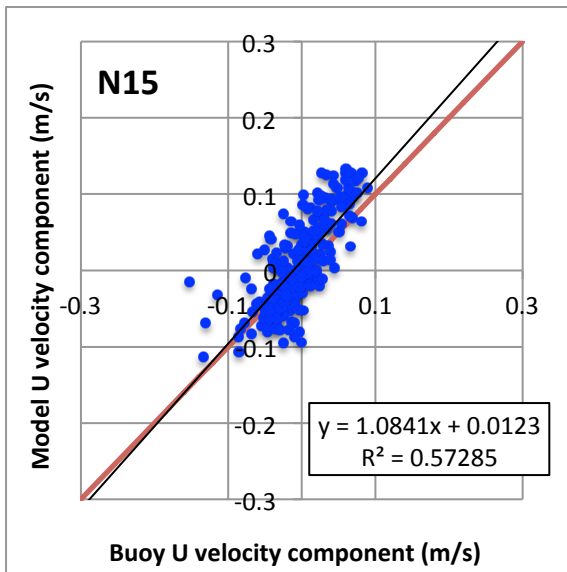
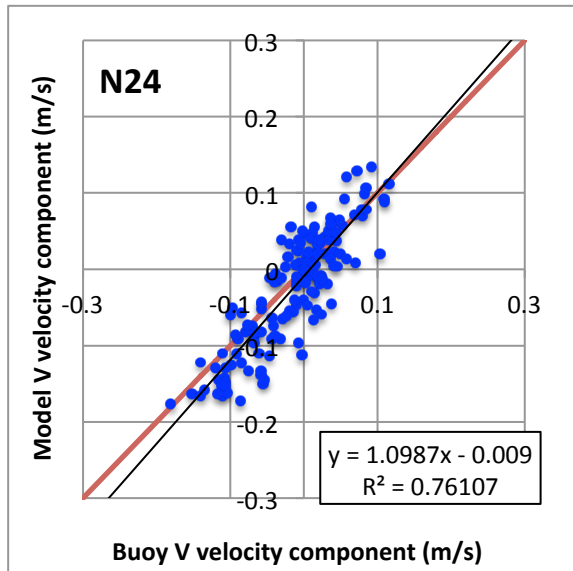
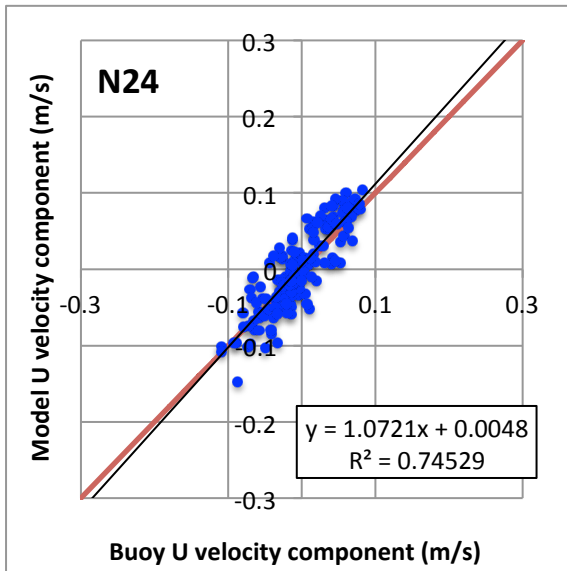
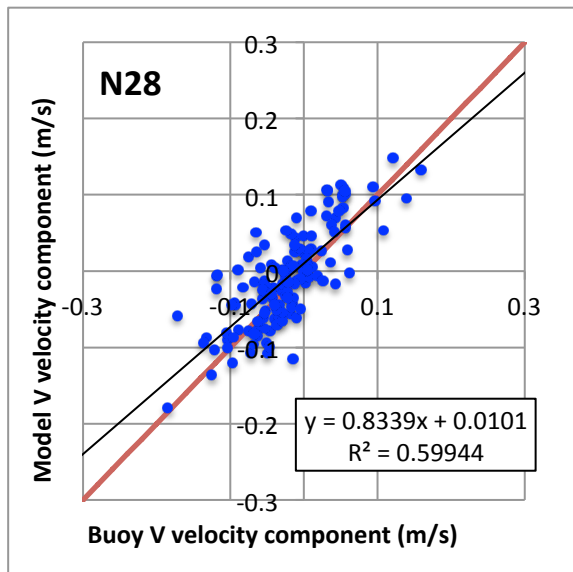
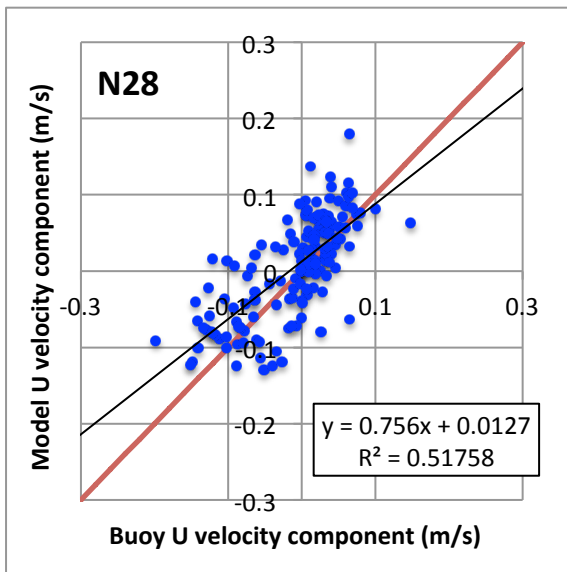


Figure 4-9 Some of the IABP buoy trajectories from 2004 January 01 to 2004 December 31. Yellow arrows show the buoy trajectories that used in scatterplots comparison.

The comparisons of buoy and model velocities during 2004 Jan 01st to 2004 Dec 31st have shown the high correlation coefficient in both velocity components. However the correlation coefficients vary with the buoy initial locations and show a minimum correlation (0.45) near the Canadian Archipelago (N04), where the ice thickness in our model and observation had shown the maximum difference. Model has shown the best correlation coefficients of 0.87 in the transpolar drift areas (N24) and near the Fram strait areas (N15), because our model reproduces the ice thickness to some extent in both regions. However, most of the buoys are situated in the single ice floe and not represent the correct continuum dynamics of the Arctic therefore in the present analysis our ice-POM model has shown the little underpredicted results. By considering the overall comparisons of sea ice velocities we can conclude that our ice-POM model is reasonably reproduce the sea ice circulation in the Arctic Ocean.



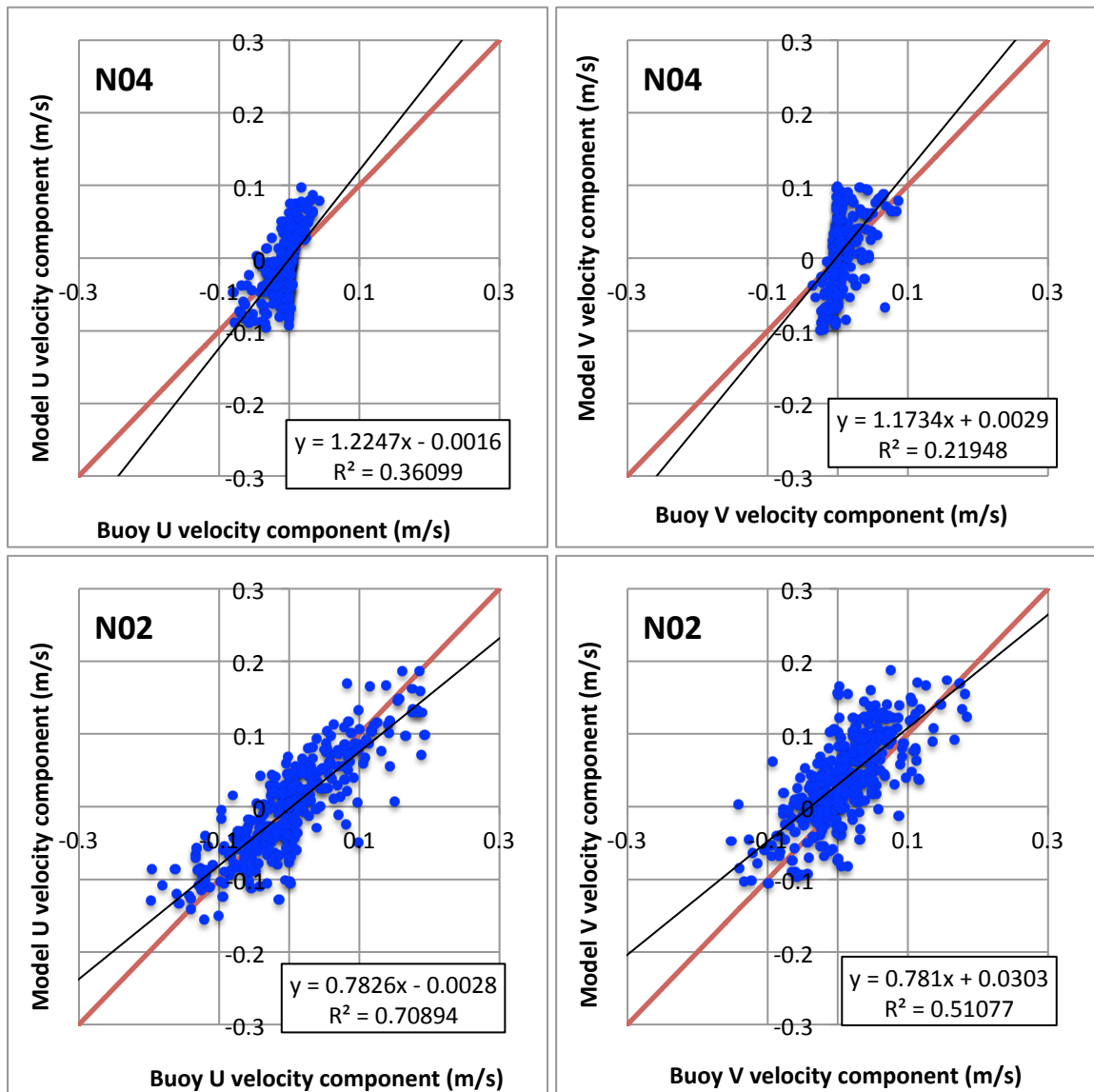


Figure 4-10 Comparison of drifting buoy motion and model derived ice motion. Left figures show scatterplot of zonal (U) velocity component and right side shows the meridional (V) component of velocities. The black line denotes the linear fit of data set

4.4. Evaluation of fresh water distribution in the Arctic Ocean

Fresh water plays a significant role in the Arctic Ocean. The vertical stratification in the halocline between cold fresh surface layer and warm salty bottom layer prevents the upward transfer of heat. Therefore it ultimately affects the formation and melting of sea ice in the region. In this section we have checked the reproducibility of fresh water content and distribution in the Arctic Ocean.

As mentioned before riverine input is not included in the present version of ice-POM model. Therefore effect of rivers cannot be reproduced with the present version. Also as mentioned before there is no interannual variation or real observation of the Bering Strait inputs only seasonal cycle is provided in the model.

To obtain a measurement of fresh water in the Arctic Ocean we have adopted the method proposed by Rabe et al. (2011). Fresh water content (FW_s) is calculated between the surface and the depth of the 34 isohaline, $h=z(s=34)$ as shown in the equation 4-1.

$$FW_s = \int_{depth} \frac{S_{ref} - S}{S_{ref}} dz \quad (4-3)$$

where S is the simulated salinity S_{ref} (=35 psu) is the reference salinity.

Fresh water content in summer (July - September) from 2001 to 2012 is shown in Figure 4-11. Two main observations can be made, first our model fresh water in Canadian basin has moved towards the Alaskan coast with time. Second, the amount of fresh water has shown a decreasing trend especially in Canadian basin compare to the observational data from Rabe et al. (2011) as shown in Figure 4-12. Those discrepancies can be explained as follows. This decreasing trend of fresh water is probably due to the salinity increment of upper layers. Because our ice-POM model does not have any riverine inputs and salinity restoring in the mixed layer, amount of salt release due to the formation of sea ice increased the salinity in upper layers. The unrealistic salinity bias of the Canadian basin is probably due to the poor resolution of model grid (about 25km). The coarseness of the model grid cannot capture the meso-scale and small-scale eddies that are very important for distribution of Pacific water into the Canada basin Watanabe and Hasumi (2009).

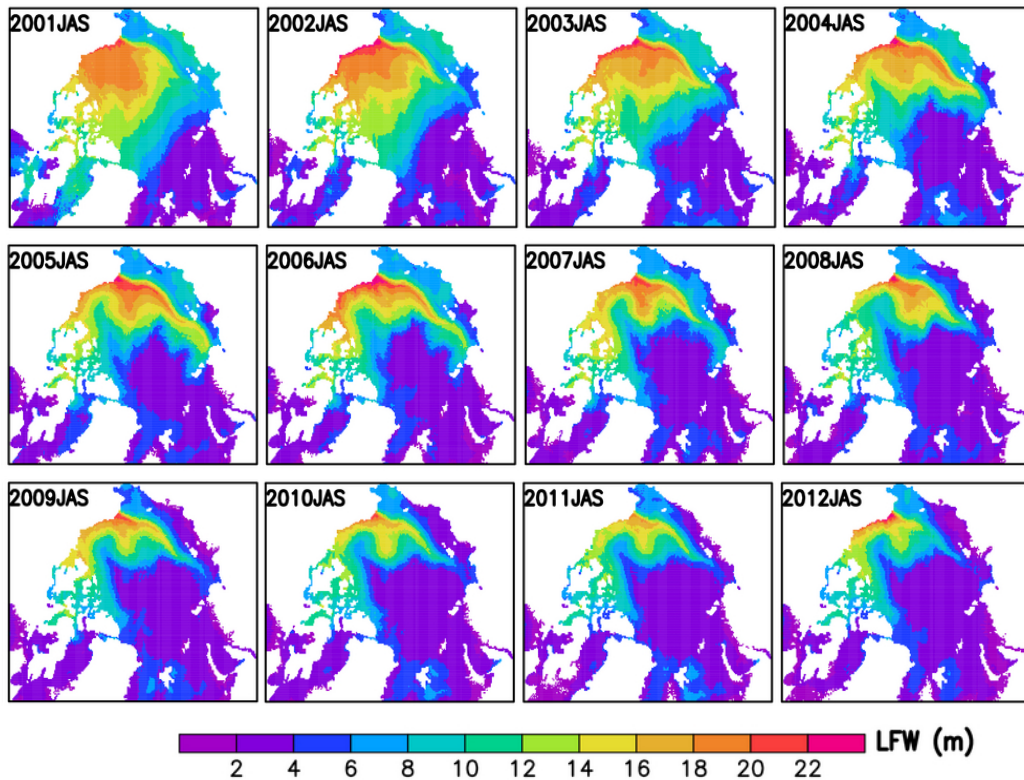


Figure 4-11 Liquid freshwater content 2001-2012 in summer (JAS)

We have discussed the significant difference of sea ice thickness along the Canadian coast in our model due to lack of thickness categories (section 4.2). The unusual westward movement of fresh water can be explained as follows: In our model we can observe that multiyear thick ice along the Canadian coast is moving towards the Alaskan side (with a positive support of anticyclonic Beaufort gyre) and melted down along the Alaskan coast throughout the computation period. Due to this unusual volume of ice transport and meltdown in the Alaskan coast, it increases the fresh water than usual climatology. In contrast to this unusual movement increase the new ice generation along the Canadian coast to fulfill the reduction. Ultimately generated new ice releases the salt into the Canadian coast and increases the salinity bias in Canadian basin further.

With the present resolution (about 25km) the reproducibility of fresh water in the whole Arctic Ocean simulation is still unclear and further analysis is needed. But it can be said that this discrepancy of fresh water does not significantly affect the Arctic sea routes predictions, particularly for the Northeast Passage.

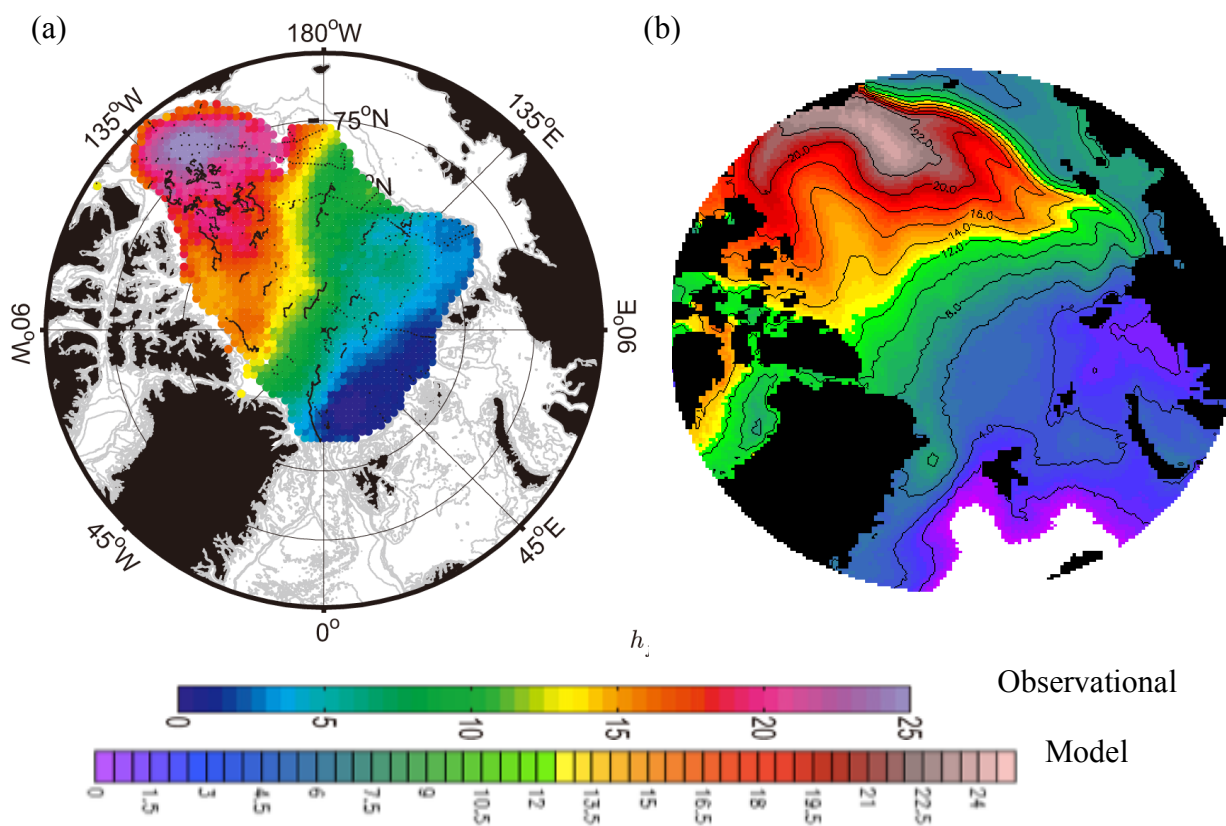


Figure 4-12 Average liquid freshwater content from 2006-2008 (JAS) (a) observational data from Rabe et al. (2011) (b) model derived

5. SIMULATION BY HIGH-RESOLUTION REGIONAL MODELS

As shown in section 4, our whole Arctic model was able to capture the long-term trend of sea ice conditions accurately. But later we have revealed that the whole Arctic coarser resolution model cannot be used to investigate the fine details of sea ice dynamics like ice edge positions and extents accurately for short-term predictions. For the applications like ASRs utilization, we have to investigate the sea ice parameters in more detailed manner. Therefore, to analyze the fine details of sea ice dynamics and accurate ice predictions in the Northeastern Passage of ASR, we have chosen 2 main regions for high resolution modeling as shown in Figure 5-1. Figure 5-1(a) red rectangles show the high-resolution domains in the whole Arctic model and color bar denotes the model bathymetries in meters. Figure 5-1(b) covers the region with 50E:165E longitude and 68N:85.5N latitudes. That consists of Laptev Sea, part of Kara and East Siberian Seas; hereafter we call this region as Laptev Sea region (LS). On the other hand, Figure 5-1(c) covers the region with 154W:151E longitudes and 64N:73.5N latitudes. That consists of Chukchi Sea and part of East Siberian Sea, hereafter we call this region as Chukchi Sea region (CS).

The basic components of the model used in these high-resolution computations are same as those used in whole Arctic computation. The resolution of zonal and meridional directions are set to be about 2.5km×2.5km in horizontal plane and 33 sigma layers in the vertical direction. Initial conditions (except sea ice concentration) and lateral boundary conditions are given by the output of the whole Arctic coarser resolution model simulations. Initial concentration is given by the satellite derived AMSR-E sea ice concentration data. The atmospheric forcing and Pacific water inflow with seasonal cycle are unchanged and same as whole Arctic model. In the marginal regions of model domain, radiation boundary condition is applied and in costal regions no-slip boundary condition is adopted. In all regional models, time integrations start from beginning of summer season and most of the regional models ran till the end of fall season.

Comparison of model results with observations, importance of high-resolution computations and sensitivity of collision rheology are discussed in the following sections.

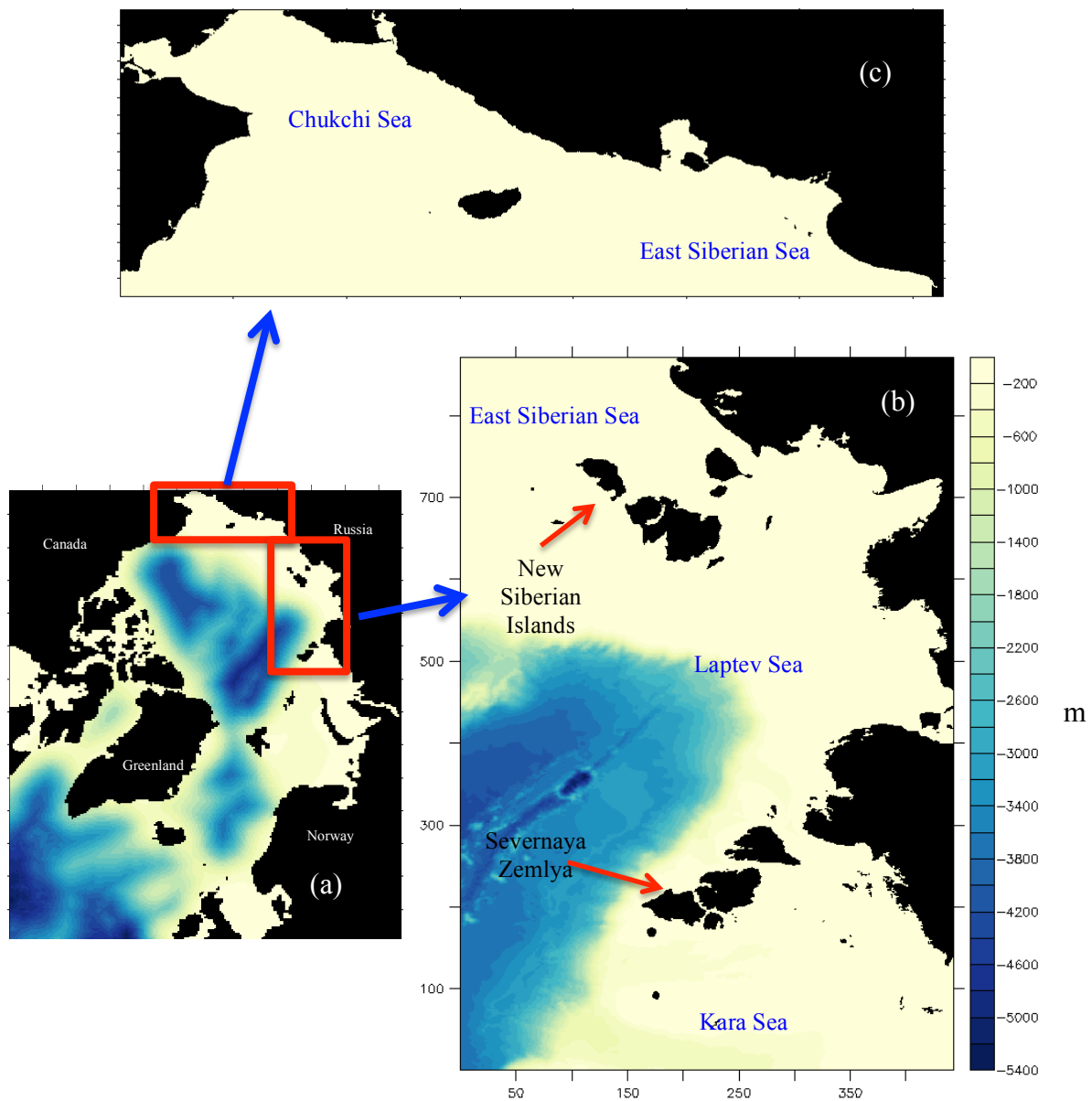


Figure 5-1 Model bathymetries. (a) Whole Arctic model and red rectangles denote the corresponding high resolution domains (b) high resolution regional model consist of part of East Siberian sea Kara sea and Laptev sea (LS) (c) high resolution regional model consisting of part of east Siberian sea and Chukchi sea (CS)

5.1. Sea ice extents and concentrations comparison with observations

Figures 5-2 and 5-3 have shown the LS region and CS region short-term (4 weeks) sea ice predictions in year 2004 and 2005 respectively. The choice of these two years is because year 2005 is one of the opening years in Northeast Passage and year 2004 is closed year for Northeast Passage. Variation of sea ice extent among coarse grid computation (Whole Arctic model), high-resolution grid computation (regional model) and satellite remote sensing observation (AMSR-E) are compared in the both figures. For the comparison, grid cells that have concentrations less than 15% are omitted.

In both LS and CS regions computations are performed from July 20 to August 17 each year. As shown in Figure 5-2 (a) LS regional model sea ice extent is varied from 1.7 millions of square kilometers to 1.3 millions of square kilometers within the 4 week time period due to the thermodynamics and dynamics activities. In first two weeks the computation has shown a similar reduction pattern with observations. In the third week, the observational sea ice extents have shown a dramatic reduction but model couldn't capture that exact dramatic reduction behavior, instead it has shown a smooth reduction. At the end of third week model sea ice extent is almost equal with observational results and similar behavior is continued in the fourth week. On the other hand Figure 5-2 (b) has shown the sea ice extent variation from 1.5 millions of square kilometers to 0.9 millions of square kilometers in year 2005. Unlike the Northeast Passage closed year 2004, the opening year 2005 high-resolution regional model overpredict the sea ice extents compare to the observations. On the other hand the coarse grid whole Arctic computation cannot reproduce the ice extent variations in both years. In year 2004 whole Arctic model sea ice extent has almost unchanged and in year 2005 it has shown a small reduction trend throughout the computations.

As shown in Figure 5-3(a) and (b), year 2004 and 2005 CS region sea ice extent has varied from 0.5 millions of square kilometers to 0.05 millions of square kilometers within the 4 weeks time period. But in year 2004 observation and regional simulation difference is much larger (about 0.1 million of km²) compared to the year 2005. Unlike the LS region of whole Arctic simulations, CS region of the whole Arctic

simulations has shown the similar reduction trend of sea ice extents to the satellite observations.

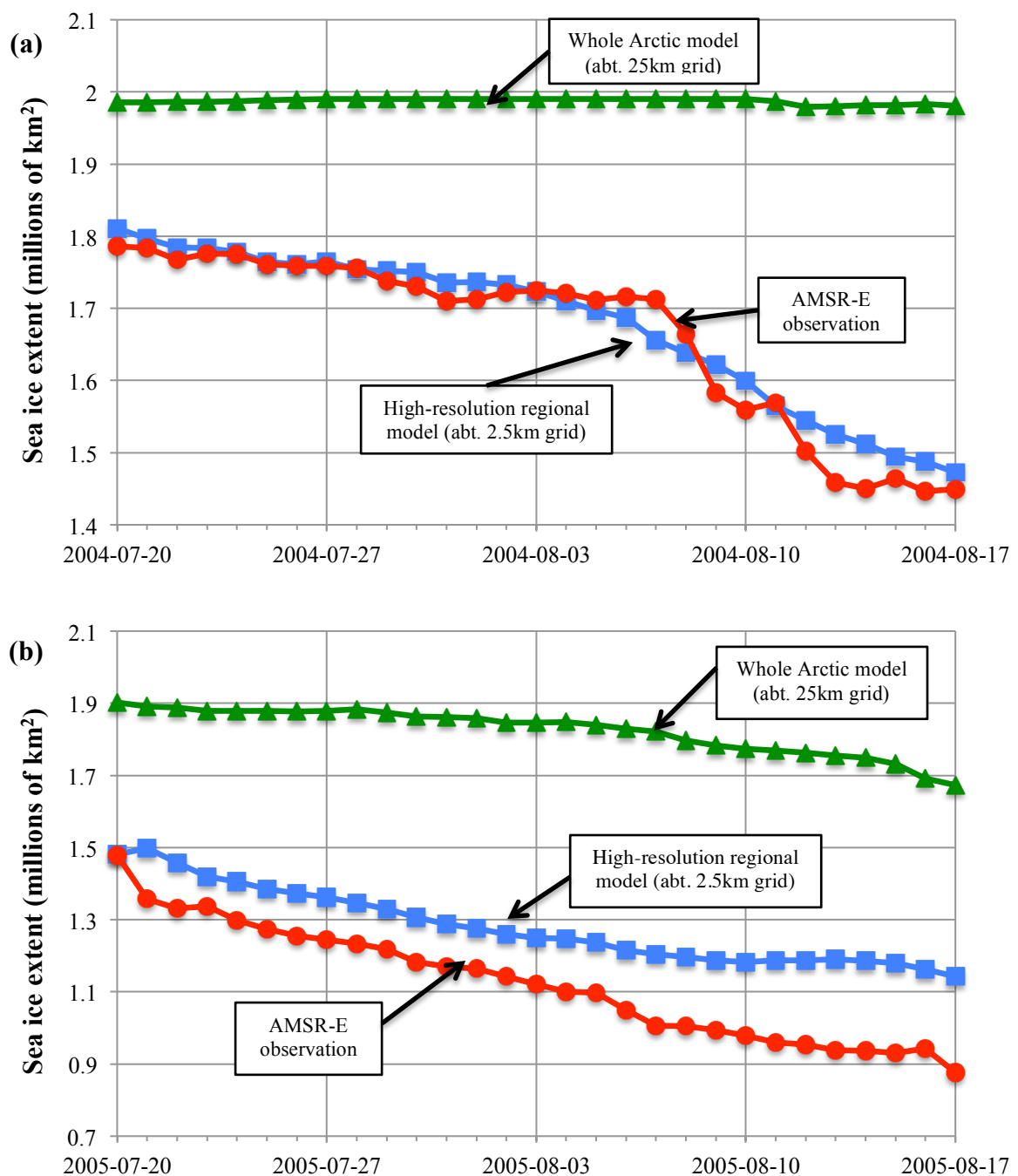
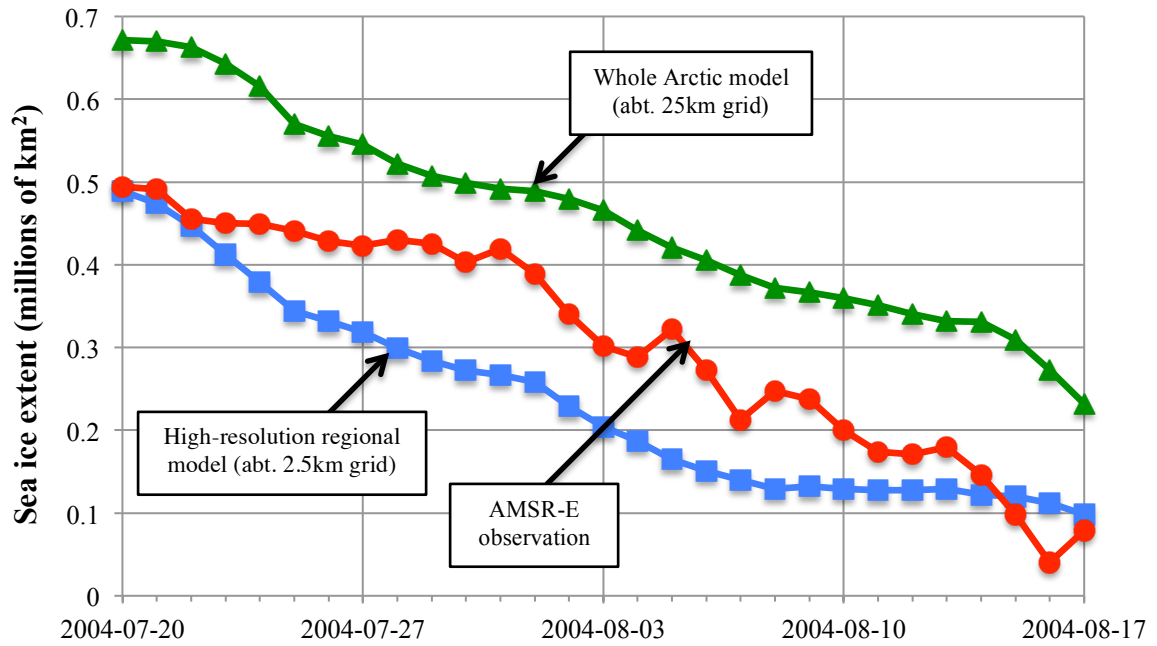


Figure 5-2 Comparison of sea ice extents between coarse grid computation (Whole Arctic model), fine grid regional computation (LS) and satellite observation (AMSR-E) (a) during 2004-Jul-20 to 2004-Aug-17 (b) during 2005-Jul-20 to 2005-Aug-17. Area covered with more than 15% ice concentration is taken into comparison.

(a)



(b)

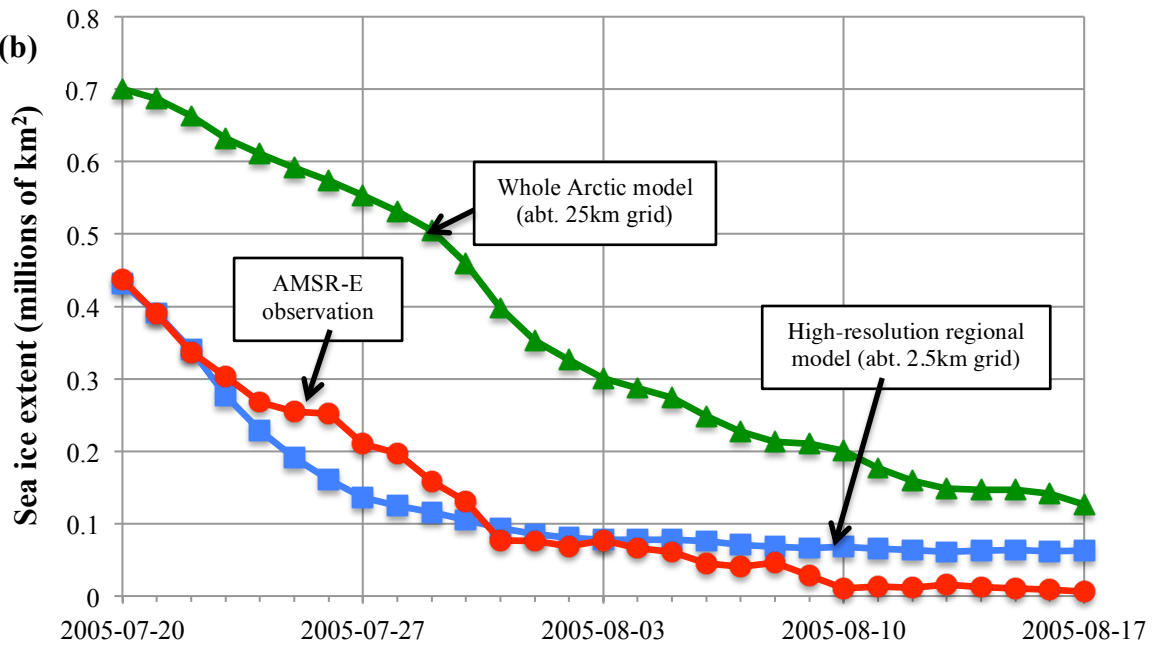


Figure 5-3 Comparison of sea ice extents between coarse grid computation (Whole Arctic model), fine grid regional computation (CS) and satellite observation (AMSR-E) (a) during 2004-Jul-20 to 2004-Aug-17 (b) during 2005-Jul-20 to 2005-Aug-17. Area covered with more than 15% ice concentration is taken into comparison.

In addition to the quantitative comparisons of sea ice extent we have compared the sea ice concentrations qualitatively. Figure 5-4 shows the comparison of sea ice concentration between numerical modeled and satellite derived AMSR-E sea ice concentrations over the period from 2004-Jul-20 to 2004-Aug-17. The overall agreement between simulated sea ice concentrations and observations is reasonable. In the north of the New Siberian islands, it is seen that the model somewhat overpredicts the concentrations. Probably this discrepancy is due to the uncertainties in the model initial conditions. Meanwhile the southwestern part of the regional model and observation are shown the similar concentration variation and ice edge location. This similar ice edge is likely subjected to the thermal front of sea surface temperature, which is made by the warmer water inflow from the Atlantic side (seen in Figure 5-5). Therefore, this invariance of the ice edge position could be due to the melting caused by the ocean heat flux at the ice edges.

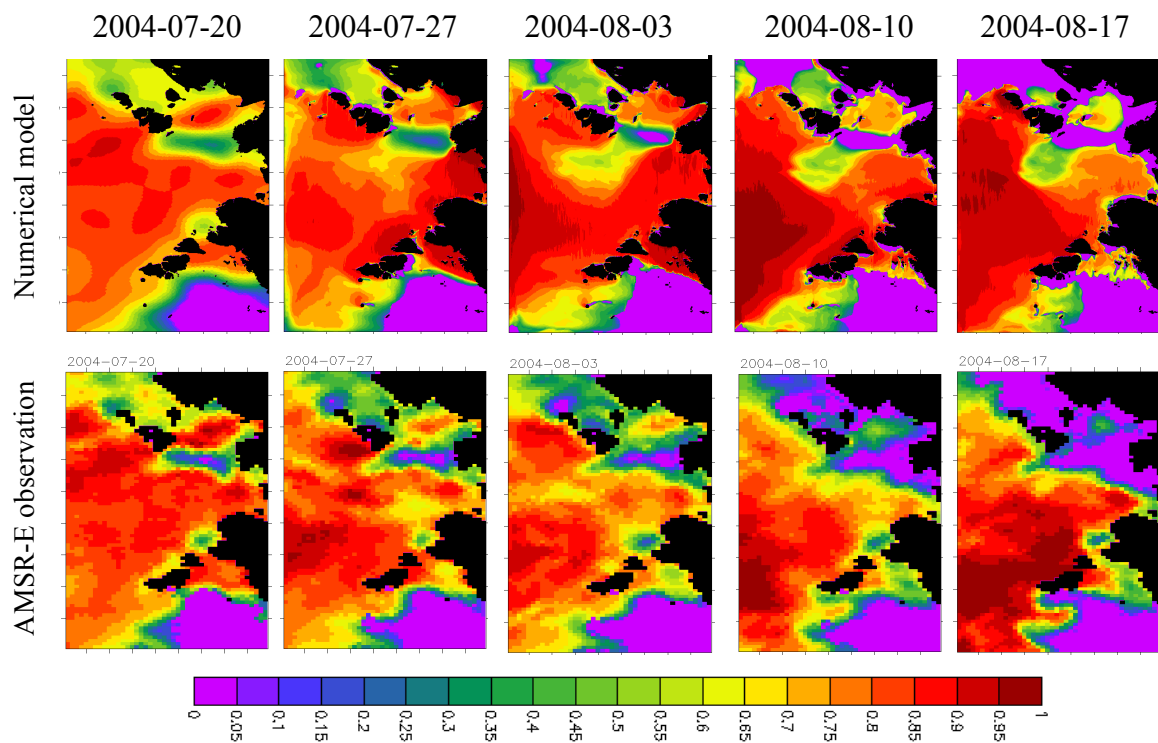


Figure 5-4 Sea ice concentration distribution from 2004-Jul-20 to 2004-Aug-17; upper figures have shown the model derived concentration and lower figures have shown the satellite observation AMSR-E sea ice concentration in the LS region

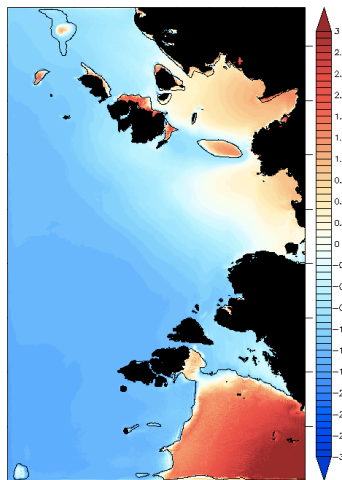


Figure 5-5 Snapshots of ocean surface temperature in LS region on 2004-Aug-03. Color bar denotes the sea ice temperate [$^{\circ}\text{C}$] and black contour denotes the 15% sea ice concentration

By considering all the qualitative and quantitative comparisons of regional model results we have come up with following conclusions. The coarse grid computation cannot be used to predict the sea ice variations in summer seasons accurately. But fine grid computation can predict the sea ice variation accurately with satellite observations. However, even the high-resolution computations cannot follow the high-frequency variations yet.

There are several possible reasons for this discrepancy results between coarser and high-resolution grid computations. First, the high-resolution grid computation well expresses the ice-albedo feedback process, which accelerates the ice melting in spring and summer seasons. If the ice is broken up, the areas of open water between floes absorb a great deal of solar energy in warm months. That energy can be transferred both to the sides of the floes and underneath the floes, promoting further melt.

The next one is small-scale sea ice dynamics was correctly captured with high-resolution models compared to the coarser grid models. The wind or ocean on sea ice either push the ice together, resulting in a smaller extent, or spread it out, resulting in larger expanses of sea ice at a lower density. These processes are known as convergence and divergence, respectively. Correctly resolved converging and diverging process of sea ice have improved the sea ice edge locations and extents.

The third reason is ice-ocean interaction. As shown in Figure 5-6 the high-resolution grid computation reproduces the meso-scale eddies in the ocean. On the other hand

coarser resolution whole Arctic computation cannot reproduce the meso-scale eddies. The meso-scale eddies in the ocean draws out the ice from its main body and enhances the melting.

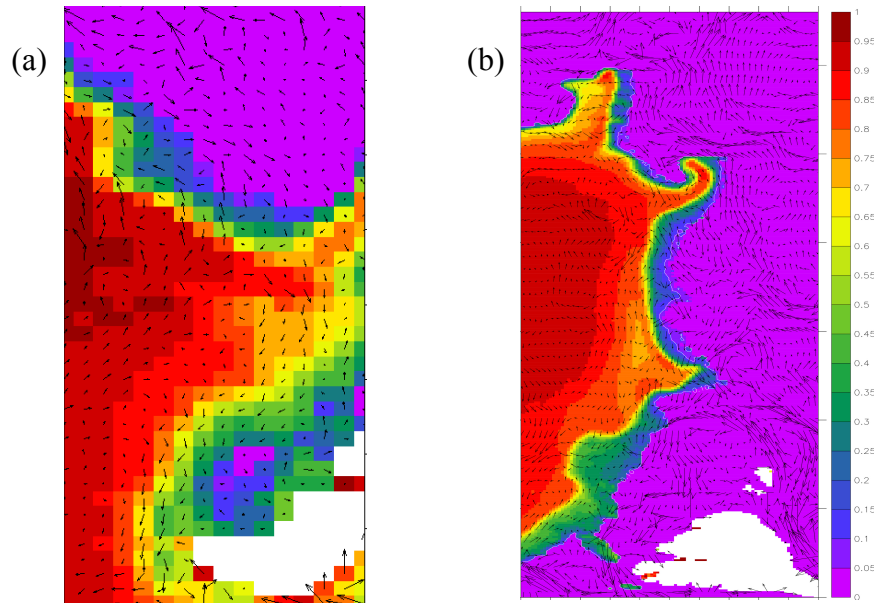


Figure 5-6 Snapshots of ice-eddy interaction: 2005-Oct-01. Color bar denotes the sea ice concentration and vectors denote the surface ocean current, location-North of Sevelnaya Zemlya Islands. (a) Whole arctic coarser grid model (b) High-resolution regional model

The mechanism for the generation of the meso-scale eddies that influence the correct reproducibility of ice extent during late summer and early autumn is investigated using the simulation result in the LS region. The mean kinetic energy (MKE) and the eddy kinetic energy (EKE) are evaluated as $\rho_0(\bar{u}^2 + \bar{v}^2)/2$ and $\rho_0(\overline{u'^2} + \overline{v'^2})/2$, respectively where bars indicate monthly means and primes denote deviations from the monthly means. To specify the EKE source, the energy conversion rates are calculated by following formulations of Eden and Böning (2002). The conversion rate from the available potential energy (APE) to the EKE induced by baroclinic instability is given by equation 5-1

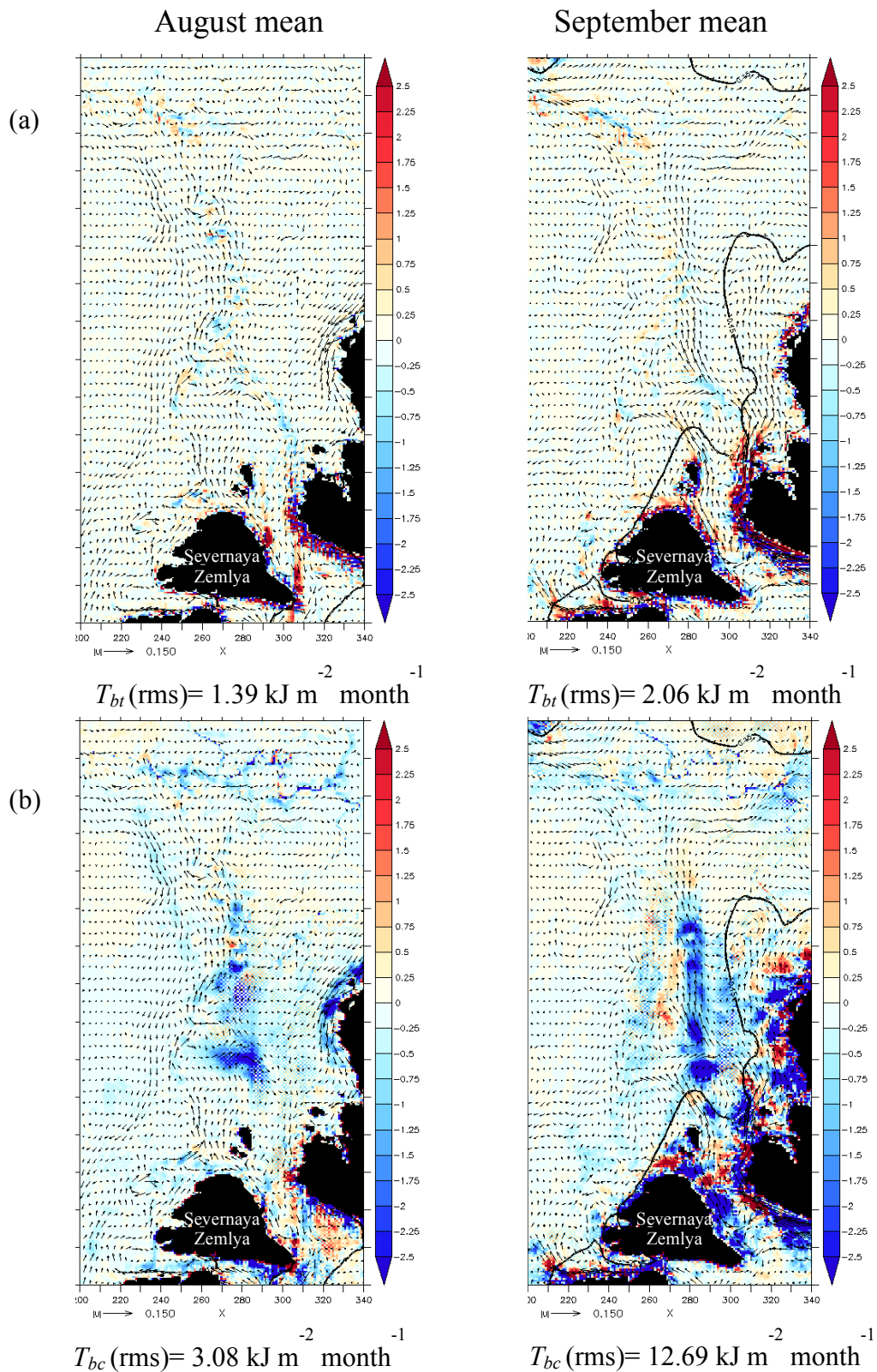


Figure 5-7 Energy conversion rates from (a) MKE T_{bt} and (b) APE T_{bc} to EKE in August and September. Root mean square value is shown in the bottom of each figure. Vectors denote the surface ocean current average in the top 100m, Average ice edge location (at 15% concentration) shown in black contour, Region North of Sevnaya Zemlya Islands.

$$T_{bc} = g \int \frac{\left(\overline{u' \rho'} \frac{\partial \bar{\rho}}{\partial x} + \overline{v' \rho'} \frac{\partial \bar{\rho}}{\partial y} \right)}{\left(\frac{\partial \bar{\sigma}_\theta}{\partial z} \right)} dz \quad (5-1)$$

and the conversion rate from the MKE to the EKE due to the horizontal velocity shear is given by equation 5-2

$$T_{bt} = -\rho_0 \int \left[\overline{u'u'} \frac{\partial \bar{u}}{\partial x} + \overline{u'v'} \left(\frac{\partial \bar{v}}{\partial x} + \frac{\partial \bar{u}}{\partial y} \right) + \overline{v'v'} \frac{\partial \bar{v}}{\partial y} \right] dz \quad (5-2)$$

where, ρ_0 is reference sea water density, ρ is in situ sea water density, and σ_θ is the horizontally averaged potential density.

These conversion rates suggest that the baroclinic instability is dominant in the vicinity of the Zemlya Islands, and T_{bt} is also significantly large there Figure 5-7. It also seen that in September T_{bc} is 4times larger than August T_{bc} and 6 times larger than T_{bt} instabilities. This instability can be explained as melted ice supplies the low-salinity cold water into the ocean surface, which activating the eddy production due to baroclinic instability. This positive feedback process increases the ice melting in high-resolution models compared to the coarser grid model. However the detailed investigation of eddy generation mechanism and its influence on sea ice are yet to be done.

Even though our main purpose is evaluating the short-term sea ice prediction for Arctic sea routes utilization in summer seasons; we have extended our computations up to the beginning of winter seasons. Figure 5-8 and Figure 5-9 have shown the both LS and CS regions sea ice extents variations from July 20 to Nov 23 on year 2004 and 2005, respectively. The high-resolution regional models have reasonably reproduced the sea ice extents in summer seasons (melting seasons) compared with the observations. However, in early fall (freezing season) our model has significantly underpredicted the sea ice extents. This delay of freezing in our model can be explained by the exclusion of riverine inputs and uncertainties of atmospheric forcing in the present version of the ice-POM model.

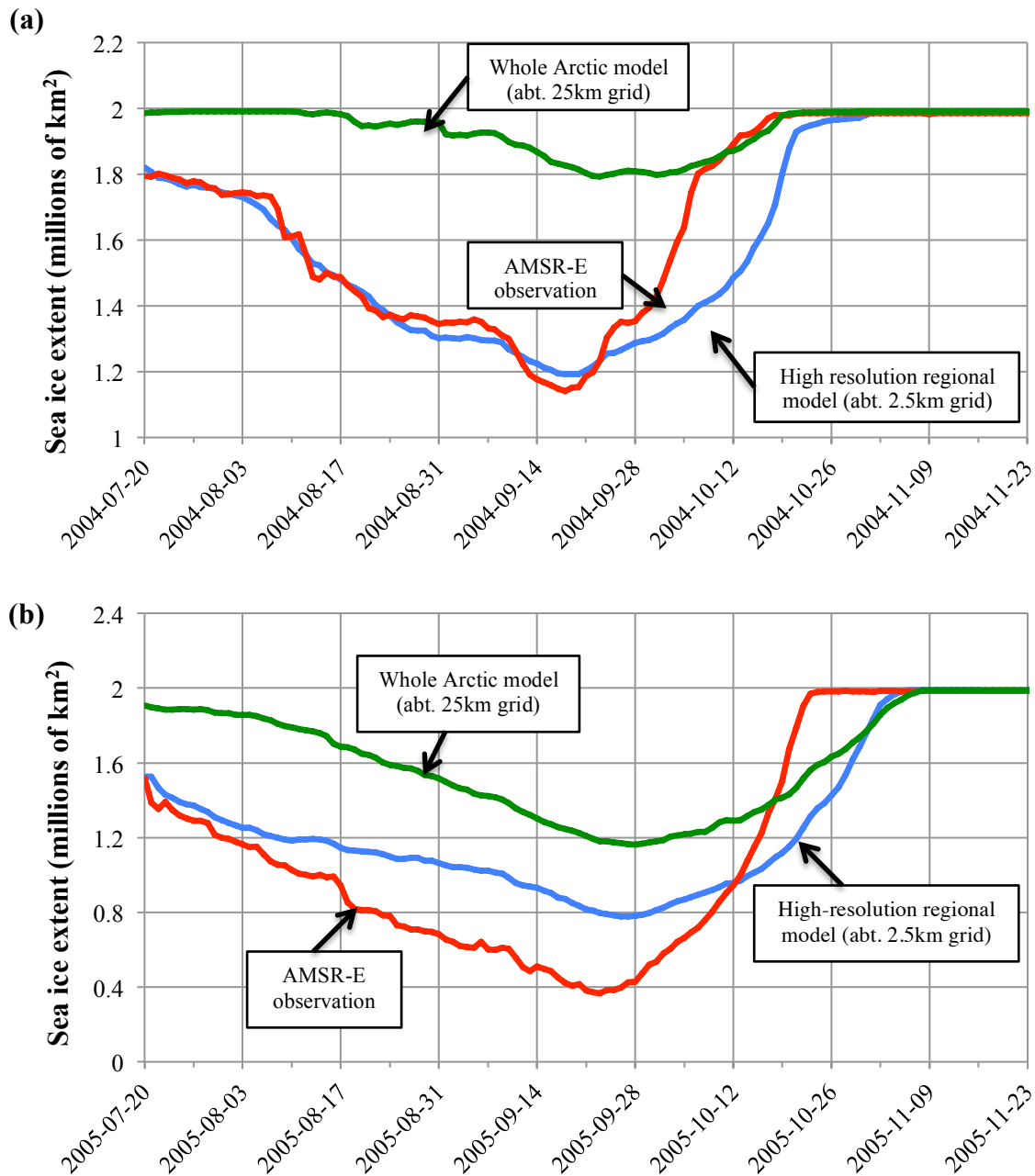


Figure 5-8 Comparison of sea ice extents between coarse grid computation (Whole Arctic model), fine grid regional computation (LS) and satellite observation (AMSR-E) (a) during 2004-Jul-20 to 2004-Nov-23 (b) during 2005-Jul-20 to 2005-Nov-23. Area covered with more than 15% ice concentration is taken into comparison.

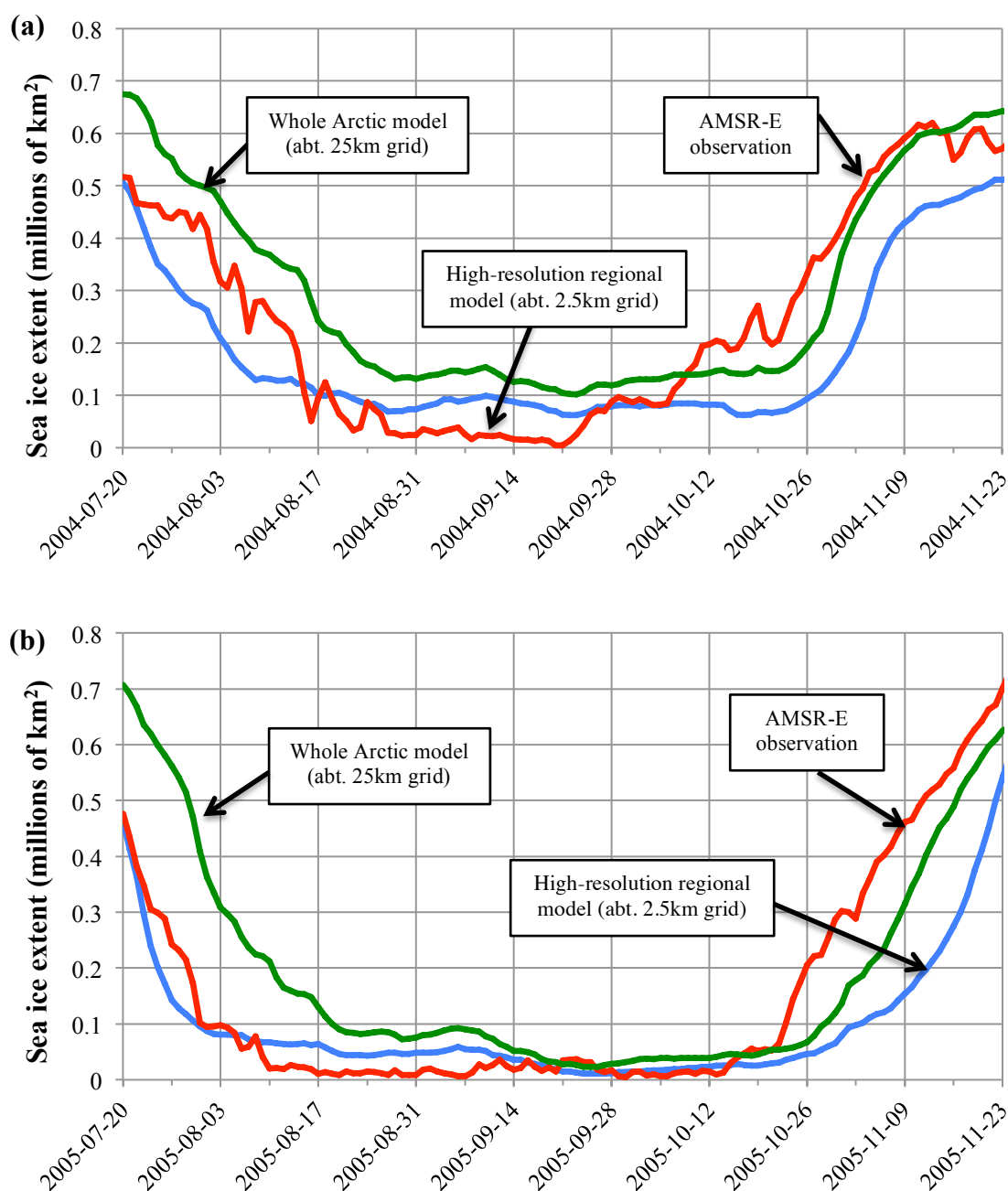


Figure 5-9 Comparison of sea ice extents between coarse grid computation (Whole Arctic model), fine grid regional computation (CS) and satellite observation (AMSR-E) (a) during 2004-Jul-20 to 2004-Nov-23 (b) during 2005-Jul-20 to 2005-Nov-23. Area covered with more than 15% ice concentration is taken into comparison.

Shelf waters of the Northeastern Passage of Arctic have observed to be stratified in summer as opposed to the well-mixed water of winter. In summer and early fall, shallow shelf seas received large fresh warm water fluxes from river runoff and cold fresh water from melted sea ice. This freshened sea surface water causes a stratification of low salinity water overlaying the higher salinity water. This stratification suppresses convection during the fall and winter cooling periods as shown in

Figure 5-10. As a result, amount of heat brought to the surface is reduced and ice growth increases. In late spring and summer, this low salinity layer again inhibits mixing. The heat absorbed by the increase in the solar radiation is confined to the surface and speedup the melting of ice. In addition, the temperature of river outflow is warmer than that of sea ice, thus causing increase in ice melting. This explanation clearly matches the discrepancy in Figure 5-8(a) in both melting and freezing delays.

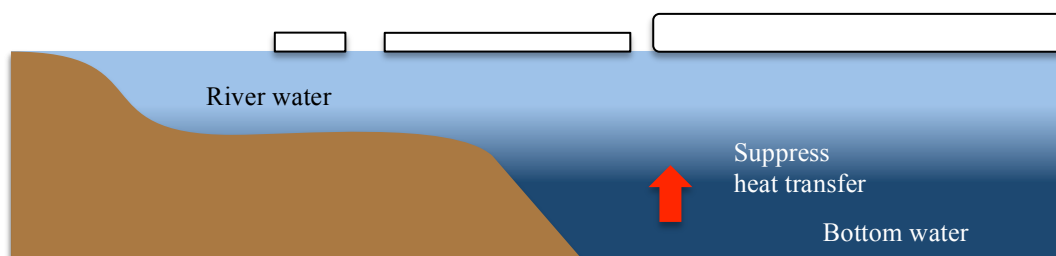


Figure 5-10 A schematic diagram of process near river mouth (fall and winter), strong stratification and suppression of convective mixing under the ice cover

To further analyze the above argument we have shown the sea ice concentration variation on 2004-Nov-12 in Figure 5-11(a and b). This particular day the maximum discrepancy occurred between AMSR-E observational sea ice extents and model extents as shown in Figure 5-8(a). Both figures clearly shown that around the Lena Riva mouth there were no sea ice in our model compared to the observations. Later we have checked the underline salinity profiles of observational PHC3.0 and model derived across the Lena River mouth as shown in Figure 5-11(c and d). In the figures it can be clearly seen that lack of river water in our model suppress the stratification considerably compared with the observation and support positive evidence to the above argument.

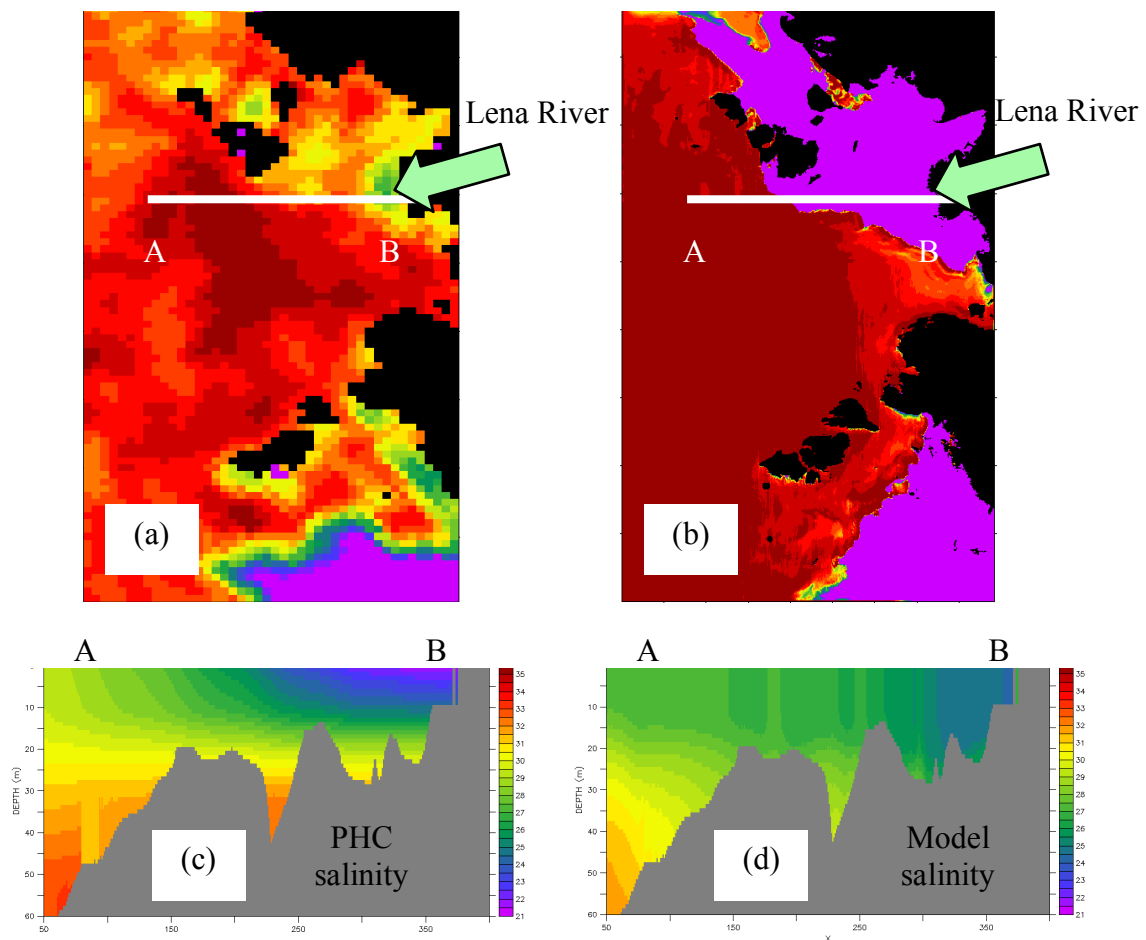


Figure 5-11 Snapshots of sea ice concentration and vertical salinity profile across the Lena River mouth (A-B) in LS region: 2004-Nov-12. (a) Satellite observation AMSR-E concentration, (b) Model derived sea ice concentration, (c) PHC3.0 observational vertical salinity profile under the line A-B and (d) Model derived vertical salinity profile under the line A-B.

Surface albedos also play the significant role in sea ice melting and formation. But in the present version seasonal variation of surface albedos are not taking into account, instead simple constant values are used. This simplification also affects the discrepancy in Figure 5-8. Wind pattern magnitude and direction and atmospheric temperature are also important factors for melting and freezing of sea ice. Warm southerly winds can promote melt because they bring warm air. Also, southerly winds move ice northward away from the coast. In summer season storms and their associated sea spray can work to reduce the albedo of the ice, further increasing melting. On the other hand cold northerly winds can enhance the freezing in the Arctic Ocean. But in the above simulations we have used the ERA-interim 0.75degree

spatial resolution data for our 2.5km resolution model. Therefore the uncertainty of forcing data could have influenced the discrepancies of sea ice extents compare to the satellite derived observations.

5.2. Sensitivity of ice-ocean coupling in high-resolution modeling

Sea ice prediction models can be categorized into two groups in terms of ice ocean interactions. Uncoupled ice-ocean models: Japan Meteorological Agency (1993); Fujisaki et al. (2007) and ice-ocean coupled models: ice-POM, COCO model Watanabe and Hasumi (2009). As shown in Figure 5-12(a) ice-ocean coupled models simulate both lateral and vertical ocean circulations in combine with sea ice dynamics and thermodynamics. Further in ice-ocean coupled models; ocean part provides the sea surface salinity, temperature, sea surface elevation and ocean velocities to the ice model and in return it received the ice velocities, evaporation, precipitation, heat flux and fresh water input from ice dynamics and thermodynamics models. On the other hand, as shown in Figure 5-12(b), uncoupled models have used the available sea surface salinity, temperature, surface elevation and ocean surface circulation data as boundary conditions to force the sea ice dynamics.

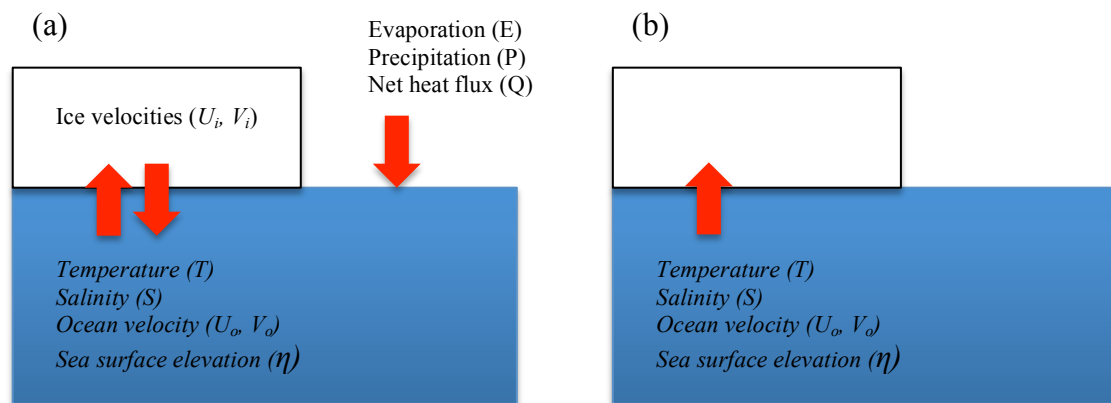


Figure 5-12 Schematic diagrams of (a) ice-ocean coupled model (fully ice and ocean dynamics are included) (b) uncoupled model (ocean variables are given to the ice model as a boundary conditions)

Many researchers have used the uncoupled sea ice models to predict the sea ice in Arctic and other ice-covered areas due to the inexpensive computational cost, simplicity and robustness of the model codes. However the accuracy of predicted results in uncoupled models are questionable even in short-term predictions. Therefore in this section we have investigated the sensitivity of ice-ocean coupling in the ice-POM model for high-resolution short-term ice perditions.

For the comparison, we have simulated the LS region with the ERA-interim atmospheric condition from 2004-Jul-20 to 2004-Aug-17. To obtain the ocean boundary conditions for uncoupled model, first the ice-POM model was run without sea ice dynamics (if the ocean temperature become super cooled we have artificially added the heat until the ocean temperature bring back to freezing temperature). After completing the ocean run, then we have started the uncoupled model simulation from 2004-Jul-17 to 2004-Aug-17 by specifying the ocean inputs as daily boundary conditions.

The sea ice extent comparison is shown in Figure 5-13. In uncoupled model sea ice extent decreases rapidly compared to the observation and ice-ocean coupled model. In the end of the 4th week, the difference of sea ice extents between uncoupled model and observation is 0.5 million square kilometers, while the discrepancy between ice-ocean coupled model and observation is about 0.2 million square kilometers.

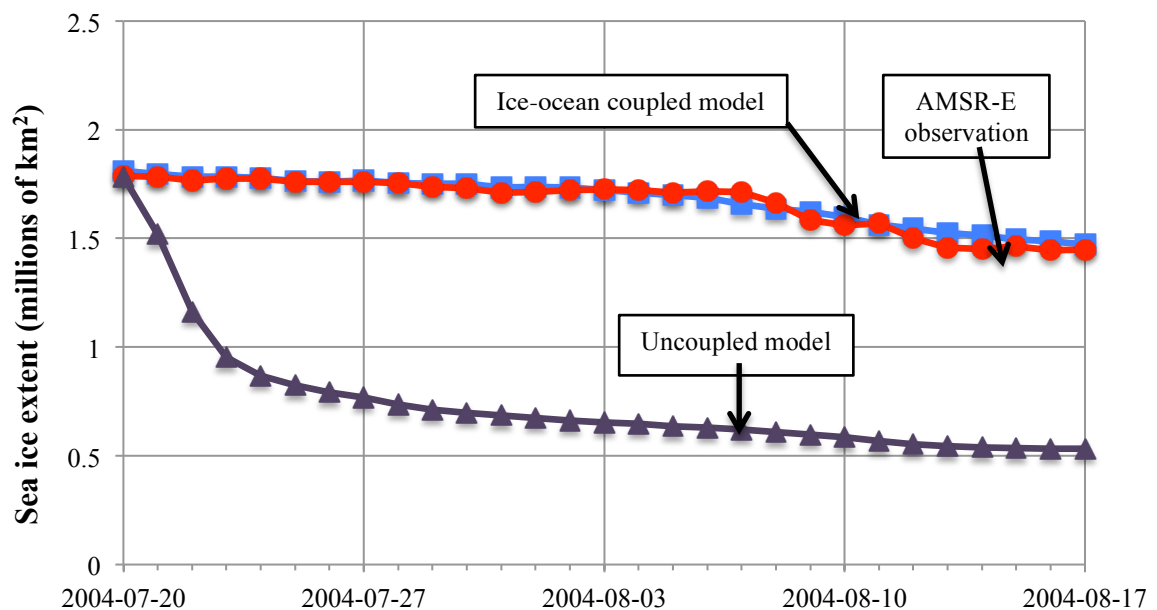


Figure 5-13 Comparison of sea ice extents between finer grid ice-ocean coupled model, fine grid uncoupled and satellite observation (AMSR-E) during 2005-Jul-20 to 2005-Aug-17. Area covered with more than 10% ice concentration is taken into comparison

The decreasing trend of ice extent in uncoupled model is about 0.25 km² per week while 0.1 km² per week in ice-ocean coupled model. On the other hand qualitative

comparison of sea ice concentrations (Figure 5-14) have shown a rapid decrease of sea ice in uncoupled model compared to the observations and coupled model.

On the other hand ice-ocean coupled model ice concentrations are overpredicted compared to the observation even though the extents are reasonable. We believe this discrepancy is mainly due to the uncertainty of initial conditions as we have used the coarser resolution model outputs for initial conditions. By looking at the results of this sensitivity study we came into the conclusion that ice-ocean coupling is important for the Arctic Ocean sea ice predictions despite the computational expenses.

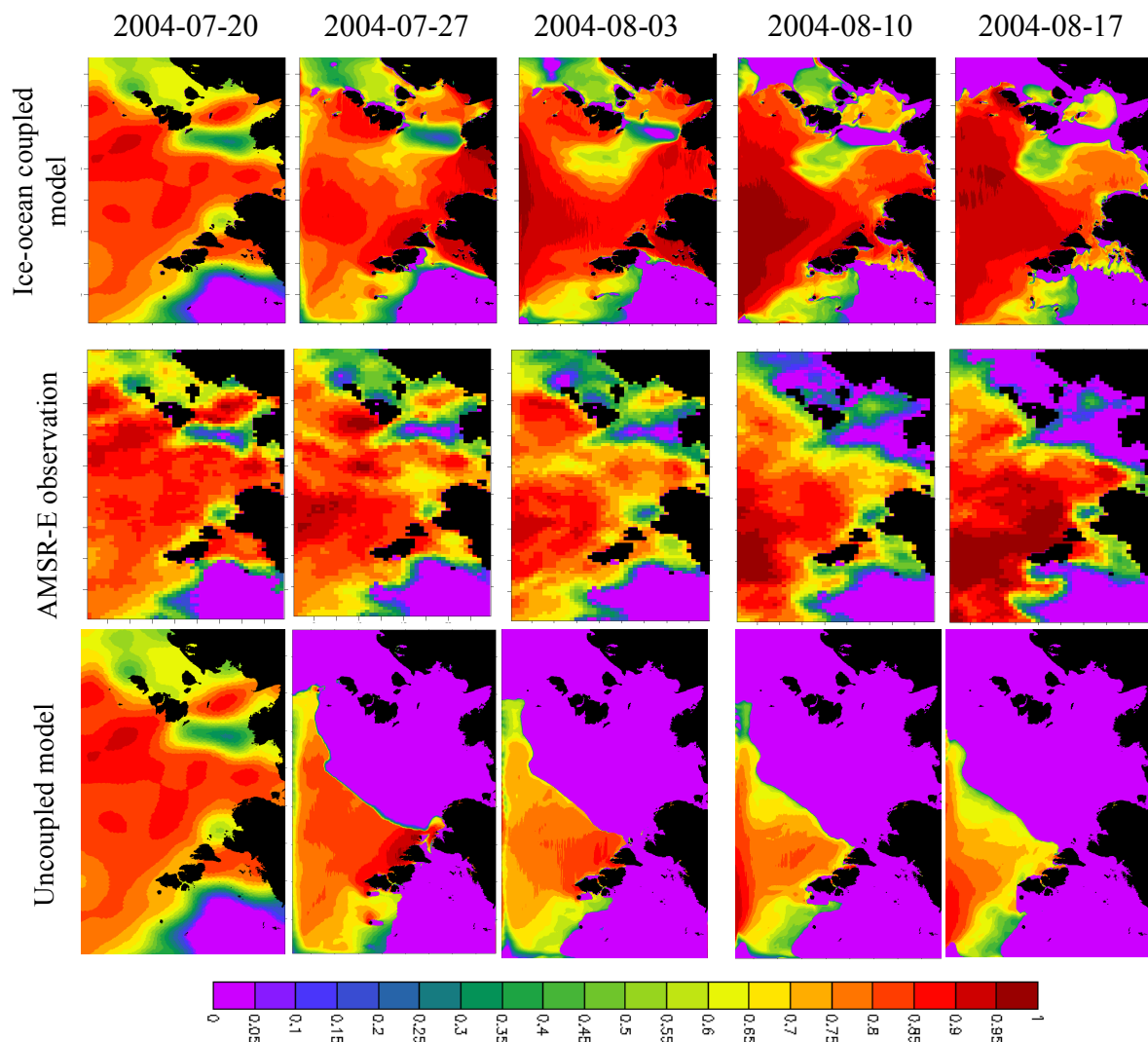


Figure 5-14 Sea ice concentration distribution from 2004-Jul-20 to 2004-Aug-17; upper figures have shown the ice-ocean coupled model derived concentrations, middle figures have shown the satellite observation AMSR-E sea ice concentration and lower figures have shown the uncoupled model sea ice concentrations in the region of LS.

5.3. Sensitivity study of ice collision rheology

As we have discussed in section 2.2.2, most of the sea ice models use the Hibler's Hibler (1979) parameterization for ice strength formulation. In Hibler's formulation sea ice strength is an exponential function of ice concentration and independent of the strain rates as shown in equation 2-49. This formulation is reasonable when the ice concentrations are greater than 90% where the ice behaves in compact condition and smaller than 50% where the ice drifts freely. But in between those concentrations there should be a region where the ice floe collision should dominant. But in Hibler's ice strength parameterization this ice floe collision has not been taken into account. Therefore to introduce the floe collision into the ice-POM model; we have customized the Hibler's strength equation using the Sagawa's method as shown in equations 2-50 to 2-52.

Sensitivity study of our collision rheology is an essential need for validating the model results and further development of the ice-POM model. Fujisaki et al. (2010) also discussed the some aspects of collision rheology using her sea of Okhotsk model (earlier version of the ice-POM). But in the present study we have used the modified version of collision rheology (discussed in section 3) therefore analyzing the new version collision rheology sensitivity is needed. To analyze the collision rheology we have used the LS region as a model domain. One simulation was performed with collision rheology (EVP and collision theories) and another simulation was performed without collision rheology (only EVP rheology). Please note that other modeling conditions and model parameters are kept equal and same with previous regional model computations (discussed in section 5-1).

Figure 5-15 and Figure 5-16 show the sea ice area and extent variation in 2004-Aug-15th to 2004-Oct-10th. The model with collision rheology has not shown the significant difference of sea ice area or extent between with and without collision rheology in early summer. But beginning of fall the model with collision rheology shows small increment (about 0.5million square kilometers) of both sea ice extent and sea ice area computations. Even though this difference is small, this difference could be significant when we discuss the Arctic sea routes near the ice edges. Spatial

distributions of differences in the ice concentration, thicknesses and ice strength are shown in

Figure 5-17.

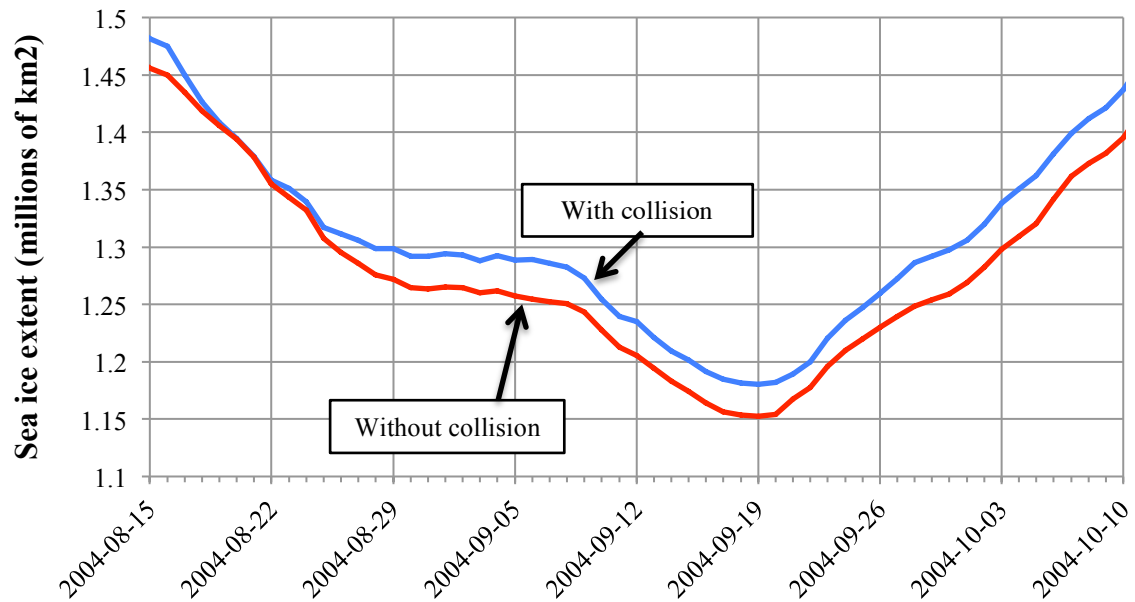


Figure 5-15 Comparison of regional model (area LS) derived sea ice extent with and without collision rheology. Area covered with more than 15% concentration is taken into comparison.

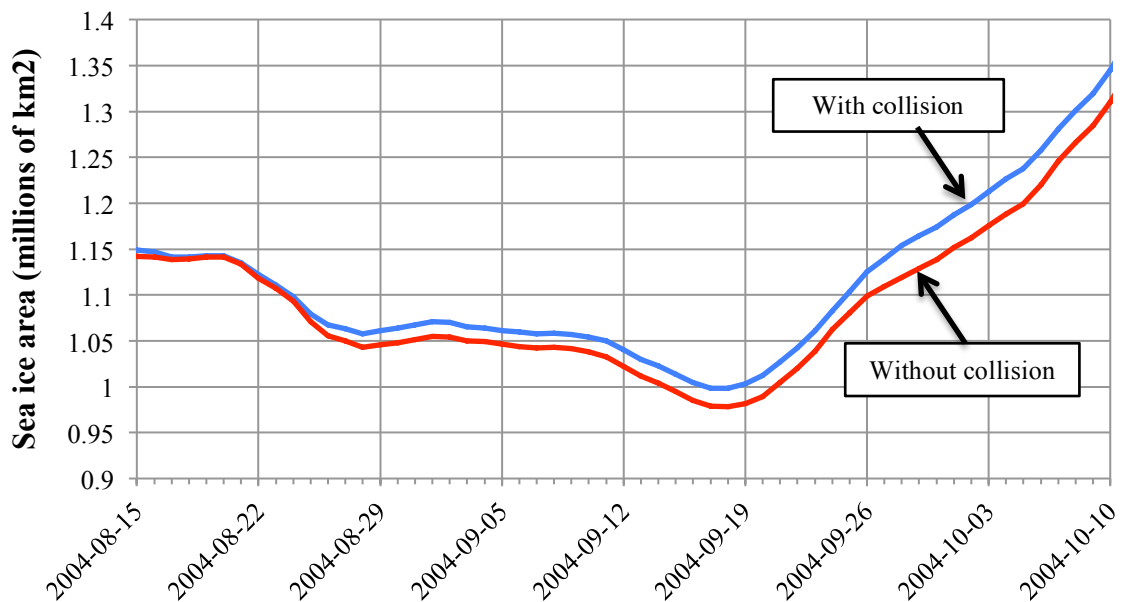


Figure 5-16 Comparison of regional model (area LS) derived sea ice area with and without collision rheology. Area covered with more than 15% concentration is taken into comparison.

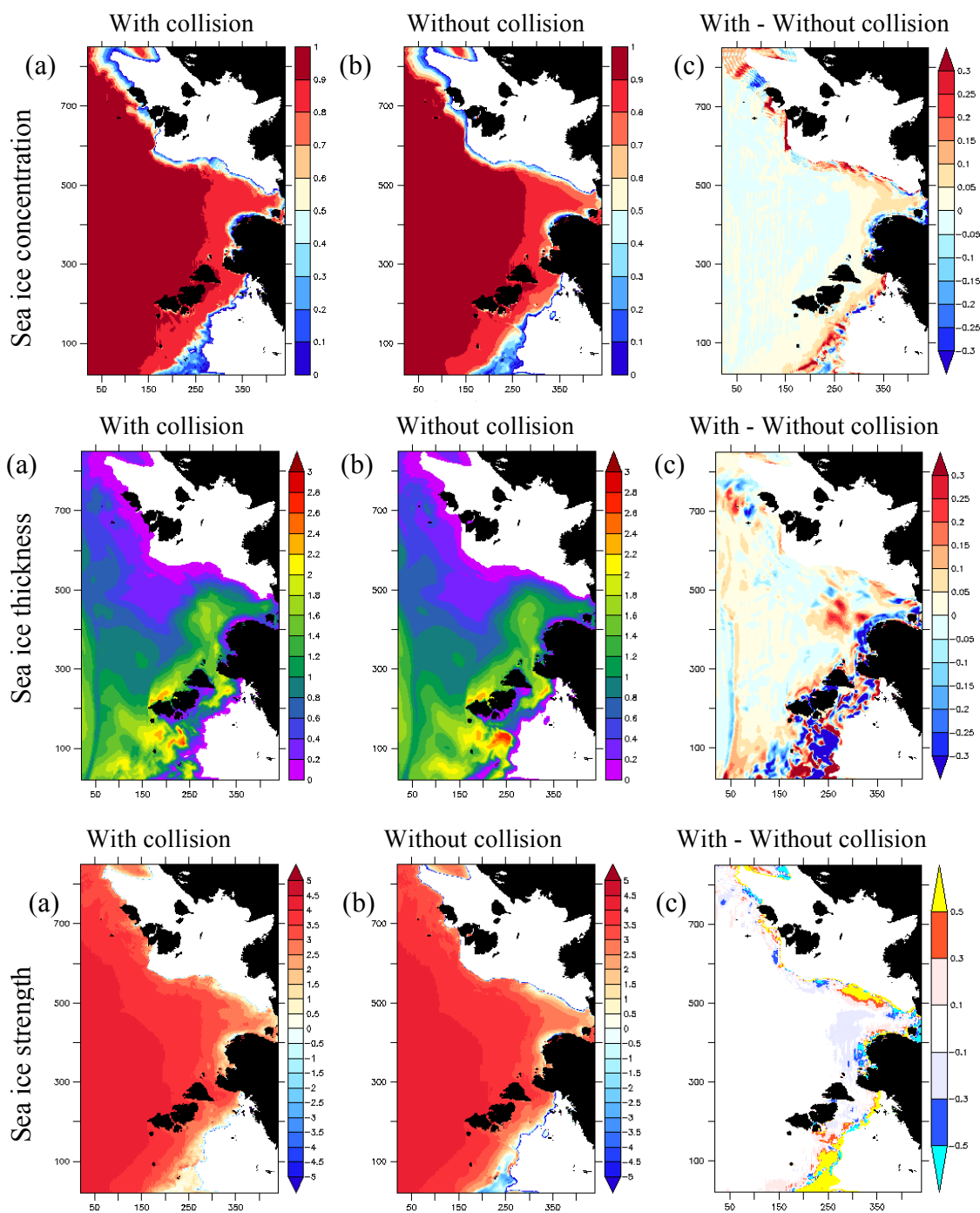


Figure 5-17 Upper figures show sea ice concentration, middle figures sea ice thickness [m], lower figures sea ice strength in logarithmic scale [N/m²] (a) with ice collision rheology (b) without ice collision rheology and (c) difference between with and without collision rheology. All variables are average over the period of 2004-Oct-01 to 2004-Oct-07

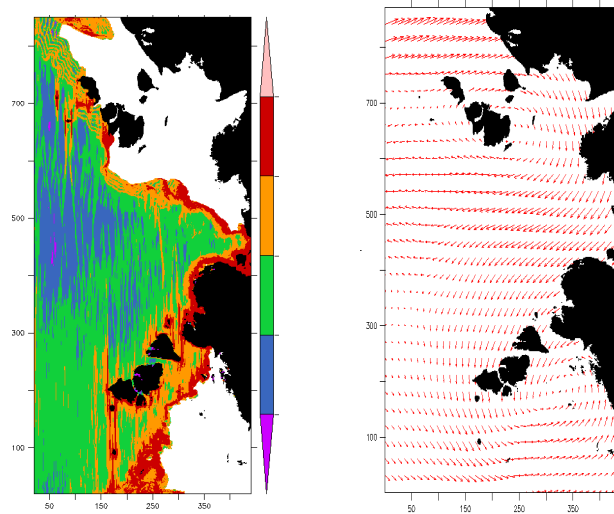


Figure 5-18 Strain rate parameter Δ in the ice collision rheology and wind velocity. All variables are averaged over the period of 2004-Oct-01 to 2004-Oct-07

High ice concentration in the ice collision model along the ice edge is supported by floe collision theories. When ice floes collide each other, it will strengthen the interaction force among floes and thereby increases the concentration and diffusivity along the ice edges. Ice strength variation along the edge also supports the above statement favorably. But along the Russian coastline; with collision rheological model has shown the low ice strength compared to the without collision rheological model. This discrepancy can be explained by the low ice thickness in the ice collision model. For example in the southern part of the Severnaya Zemlya islands, sea ice thickness shows the scattered nature (Figure 5-17(a) and (c)). As shown in Figure 5-18, strain rate and wind velocity have clearly shown the reasons for this scattered behavior of sea ice in southern part of Zemlya islands. The wind is blowing off the ice edge and drifts the ice away from its main body and thereby strain rates get increased. When the strain rate increases, the collision rheology ice strength also increases due to the floe collision and shows the real world scattered nature (as shown in Figure 5-19) in the numerical model reasonably.

By looking at the basic results of sensitivity study we can conclude that our collision rheology plays a significant role in sea ice prediction along the Arctic sea routes.

However, lacks of high-resolution and accurate observation data are one of the key problems to conduct the in-depth sensitivity analysis about collision rheology.

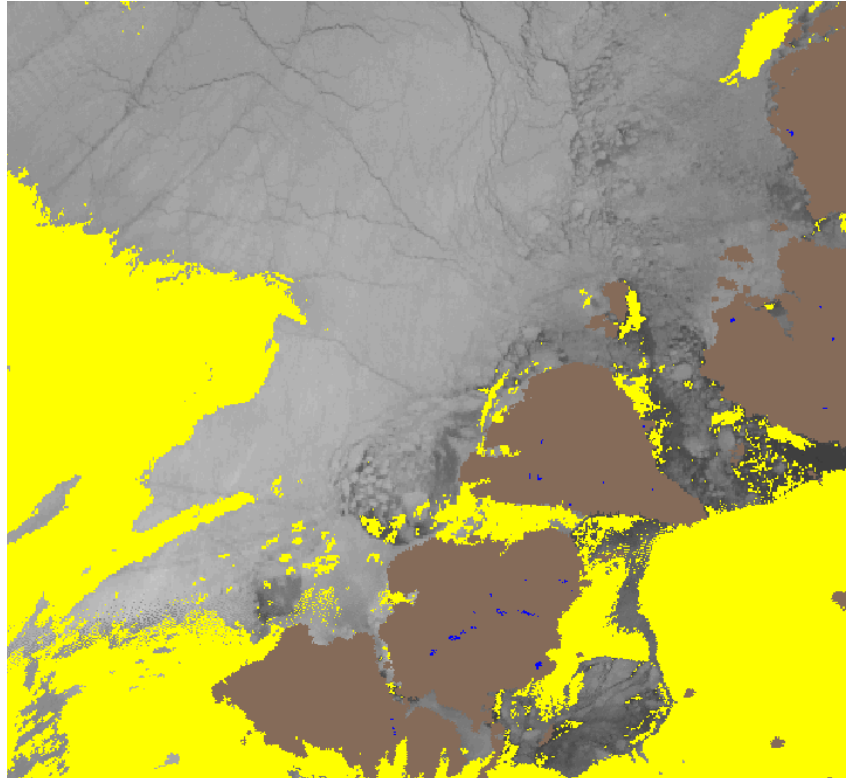


Figure 5-19 Satellite observation (MODIS) sea surface temperature distribution at South of Sevelnaya Zemlya Islands on 2004-Oct-01

6. GENERAL CONCLUSIONS AND FUTURE WORKS

Summer sea ice in the Arctic Ocean is retreating further away from most Arctic landmasses, opening new shipping routes and extending the navigation season in the ASRs. The passages through the Arctic Ocean are the shortest sea route from North American and European harbors to Southeast Asian harbors. However to navigate in the Arctic prediction of sea ice condition is crucial, especially in marginal sea ice zones. Many numerical models have been used to predict the overall Arctic sea ice conditions successfully. However, the model results have shown high uncertainties in the marginal ice zones. Therefore accurate prediction method for marginal sea ice condition is an urgent need for cruising ASRs. Therefore, in this study we have used the high-resolution ice-ocean coupled model with explicitly treating the ice floe collision using ice collision rheology to predict the sea ice condition in marginal ice zones for short-term (about 1 to 2 weeks). The development and application of the meso-scale eddy resolving ice-POM model have been described. It is encouraging that the ice-POM model reproduces many of the dynamical and thermodynamical features of the Arctic ice-ocean coupled system accurately. Based on the investigation in previous sections, results can be summarized as follows.

Numerical difficulties in high-resolution ice-POM model were discussed. We have shown that abrupt changes in the ice strength P (due to the earlier version floe collision rheology) can cause the instability in the high-resolution ice-POM sea ice model. The symptoms of the instability are noisy and unrealistic sea ice thickness, ice concentration, strength, velocity, and strain rates. Unstable flow typically arises near islands and coastlines where convergence and shear are large. The instability is made possible by the large changes in ice stress that occur as the floe collided each other with the maximum compactness. However, the instability is fundamentally numerical, not physical. The model gives realistic behavior with small time steps (about 10 second), becoming unstable only when time step exceeds the timescale for large changes in P . But small time steps like 10seconds are not practical in the sense of computational economy. Modification of floe collision near the maximum compactness (about 90% concentration) and new method of proper damping of elastic waves in EVP rheology successfully resolved the instability issues in the ice-

POM model without reduction of time step interval. This modification leads to a stable numerical scheme that further improves the model's computational efficiency and accuracy.

Then, coarser resolution (about 25km) whole Arctic model was performed to investigate the reproducibility of basic features in the ice-POM model. The model has reproduced the seasonal and interannual sea ice extents variation and record minimum sea ice years (2007, 2011) in the Arctic Ocean reasonably. The overall sea ice thickness distribution is reasonably reproduced. And except the Canadian Archipelago and northern Greenland the other areas sea ice thickness is quantitatively consistent with available observations. However, the ice-POM model can be used to reproduce the thin first year ice reasonably and can be used to predict the sea ice in Northeastern Passage of Arctic sea routes. General feature of Arctic circulation patterns, anticyclonic Beaufort gyre and transpolar drift were reproduced accurately. Salient features of Arctic sea ice circulations were also reproduced reasonably with observational Arctic buoy data sets. On the other hand coarser resolution whole Arctic ice-POM model cannot be used to reproduce the correct fresh water transport and accumulation in the Arctic Ocean. Because as many researchers suggested that the Pacific water is transported into the Canada Basin by meso-scale eddy activities, which are hardly resolved in the coarser resolution models.

Next high-resolution ice-ocean coupled system was investigated with a meso-scale eddy resolving model forced by realistic ERA-interim atmospheric data. Numerical codes for the Northeast Passage of Arctic sea routes have been developed by hindcast computations. Even though the whole Arctic model well reproduced the overall trends of long-term changes of the Arctic sea ice, it cannot be used to predict the sea ice in short-terms. On the other hand the high-resolution regional model has reproduced the reasonable sea ice extents and concentrations compared with the observational data.

As a final conclusion, in terms of accurate forecasting sea ice using high-resolution ice-ocean coupled model we have to input the appropriate initial conditions and realistic forcing data. At this point lack of observational sea ice data and coarseness of the reanalysis forcing data are the key bottleneck for making accurate forecasting and validating the model results in Arctic area. However, the present result has shown that

our model can be used to predict the short-term sea ice fairly accurately despite those limitations.

FUTURE WORKS

It seems present version of the ice-POM model in the whole Arctic model cannot be used to reproduce the multiyear thick ice without having the subgrid-scale thickness categories. Reproducibility of thick ice is very important in the sea ice prediction in Northwestern Passage. Thus, sea ice distribution for describing thickness features should be applied in the near future. In the coarser grid (about 25km) whole Arctic model simulation couldn't reproduce the correct fresh water distribution and accumulation in the Arctic Ocean. Ocean structure reproducibility of whole Arctic model is important for initial conditions of high-resolution computations. Therefore in the future we have to improve the model resolution (at least 10km) for correctly resolve the Neptune effects Holloway (1992) and small-scale eddy formations.

The high-resolution model results are also suggested that the ice-ocean heat transfer may be a dominant factor in determining the ice edge especially in the boundary of southeast part of Arctic Ocean (Kara Sea and Barents Sea areas), where the warm Atlantic current is mixed with cold Arctic. However, analysis of this ocean thermal front interaction with ice edge positions are needed in the future studies.

Then, the high-resolution regional model for short-term predictions revealed the significant importance of ice-albedo feedback and ice-ocean interaction for precise ice predictions. Importance of riverine inputs in short-term prediction in Northeastern Passage is also revealed in high-resolution regional model. In addition to the above, it has revealed the meso-scale eddy formation and movement behavior of marginal ice zones. Those fine details of sea ice motion weren't revealed in the previous coarser resolution experiments. This finding may assist to investigate more details about sea ice characteristic in future studies.

So far we have performed the hindcast computations to evaluate the ice-POM model performance in the Arctic sea routes. Once we extent our computations into the short-term predictions, we have to think about the accurate and reliable atmospheric forcing data to drive the ice-POM model in the future. In this point we can suggest three possible method to obtained the atmospheric forcing data to force our ice-POM model: some global atmospheric-ice-ocean coupled model results, ensemble model

predictions, or commercially available Japan metrological agency atmospheric forcing data.

We have discussed the forecast accuracy with the sea ice extent. However, ultimately, it is difficult to evaluate the forecast accuracy perfectly using only one index. Therefore, in the future we are planning to evaluate our model results using the ice edge error location method and forecast verification matrix method proposed by Japan meteorological agency CHIKASAWA et al. (2008). Even if realistic sea ice index is applied, this does not directly lead to the improvement of evaluation method because of the coarseness and uncertainties in the observational data. Therefore we have to demand for accurate and high-resolution observations in the future. But ultimately, what is important is not just to reduce the ice edge error or improvement of sea ice extent, but use this model results as a diagnostic tool for further improvement of the model parameterizations and safe navigation in the Arctic sea routes.

7. REFERENCES

- Amante, C., and B. W. Eakins, 2009: ETOPO1 1 Arc-Minute Global Relief Model: Procedures, Data Sources and Analysis. *NOAA Technical Memorandum NESDIS NGDC-24*, 19.
- CHIKASAWA, M., T. IMAIZUMI, and K. HAMADA, 2008: A numerical experiment of sea ice distribution forecast using MOVE/MRI.COM system in the southern part of the Sea of Okhotsk. *The 23rd international symposium on Okhotsk sea & sea ice*, Mombetsu, The Okhotsk Sea & Cold Ocean Research Association, 91–98.
- Comiso, J. C., C. L. Parkinson, R. Gersten, and L. Stock, 2008: Accelerated decline in the Arctic sea ice cover. *Geophysical Research Letters*, **35**, L01703, doi:10.1029/2007GL031972.
- Coon, M. D., G. A. Maykut, R. S. Pritchard, D. A. Rothrock, and A. S. Thorndike, 1974: Modeling the Pack Ice as an Elastic-Plastic Material. *AIDJEX Bulletin*, **24**, 1–105.
- Curry, J. A., J. L. Schramm, and E. E. Ebert, 1995: Sea Ice-Albedo Climate Feedback Mechanism. *Journal of Climate*, **8**, 240–247, doi:10.1175/1520-0442(1995)008<0240:SIACFM>2.0.CO;2.
- Dee, D. P. and Coauthors, 2011: The ERA-Interim reanalysis: configuration and performance of the data assimilation system. *Quarterly Journal of the Royal Meteorological Society*, **137**, 553–597, doi:10.1002/qj.828.
- Eden, C., and C. Böning, 2002: Sources of Eddy Kinetic Energy in the Labrador Sea. *Journal of Physical Oceanography*, **32**, 3346–3363, doi:10.1175/1520-0485(2002)032<3346:SOEKEI>2.0.CO;2.
- Efimova, N. A., 1961: On methods of calculating monthly values of net longwave radiation (in Russian). *Meteorol. Gidrol.*, **10**, 28–33.
- Emery, W. J., C. W. Fowler, and J. A. Maslanik, 1997: Satellite-derived maps of Arctic and Antarctic sea ice motion: 1988 to 1994. *Geophysical Research Letters*, **24**, 897–900, doi:10.1029/97GL00755.
- Fujisaki, A., H. Yamaguchi, F. Duan, and G. Sagawa, 2007: Improvement of short-term sea ice forecast in the southern Okhotsk Sea. *Journal of Oceanography*, **63**, 775–790, doi:10.1007/s10872-007-0066-x.
- Fujisaki, A., H. Yamaguchi, and H. Mitsudera, 2010: Numerical experiments of air–ice drag coefficient and its impact on ice–ocean coupled system in the Sea of Okhotsk. *Ocean Dynamics*, **60**, 377–394, doi:10.1007/s10236-010-0265-7.

- Hakkinen, S., A. Proshutinsky, and I. Ashik, 2008: Sea ice drift in the Arctic since the 1950s. *Geophysical Research Letters*, **35**, L19704, doi:10.1029/2008GL034791.
- Haltiner, G. J., and F. L. Martin, 1957: *Dynamical and Physical Meteorology*. McGraw-Hill,.
- Haney, R. L., 1991: On the Pressure Gradient Force over Steep Topography in Sigma Coordinate Ocean Models. *Journal of Physical Oceanography*, **21**, 610–619, doi:10.1175/1520-0485(1991)021<0610:OTPGFO>2.0.CO;2.
- Hibler, W. D., 1979: A Dynamic Thermodynamic Sea Ice Model. *Journal of Physical Oceanography*, **9**, 815–846, doi:10.1175/1520-0485(1979)009<0815:ADTSIM>2.0.CO;2.
- Holloway, G., 1992: Representing Topographic Stress for Large-Scale Ocean Models. *Journal of Physical Oceanography*, **22**, 1033–1046, doi:10.1175/1520-0485(1992)022<1033:RTSFLS>2.0.CO;2.
- Holloway, G. and Coauthors, 2007: Water properties and circulation in Arctic Ocean models. *Journal of Geophysical Research*, **112**, C04S03, doi:10.1029/2006JC003642.
- Hopkins, M. A., W. D. Hibler, and G. M. Flato, 1991: On the numerical simulation of the sea ice ridging process. *Journal of Geophysical Research*, **96**, 4809, doi:10.1029/90JC02375.
- Hunke, E. C., 2001: Viscous–Plastic Sea Ice Dynamics with the EVP Model: Linearization Issues. *Journal of Computational Physics*, **170**, 18–38, doi:10.1006/jcph.2001.6710.
- Hunke, E. C., and J. K. Dukowicz, 1997: An elastic-viscous-plastic model for sea ice dynamics. *Journal of Physical Oceanography*, **27**, 1849–1867.
- Ikeda, M., 2009: Mechanisms of the recent sea ice decay in the Arctic Ocean related to the Pacific-to-Atlantic pathway. *Influence of Climate Change on the Changing Arctic and Sub-Arctic Conditions*, Springer Netherlands, 161–169.
- Ikeda, M., J. Wang, and A. Makshtas, 2003: Importance of Clouds to the Decaying Trend and Decadal Variability in the Arctic Ice Cover. *J Meteorol Soc Jpn*, **81**, 179–189.
- Japan Meteorological Agency, 1993: A numerical sea ice prediction in the southern part of the Okhotsk. *Geophys Magazine*.
- Kimura, N., and M. Wakatsuchi, 2000: Relationship between sea-ice motion and geostrophic wind in the northern hemisphere. *Geophysical Research Letters*, **27**, 3735–3738, doi:10.1029/2000GL011495.

- Kitagawa, H., N. Ono, H. Yamaguchi, K. Izumiyama, and K. Kamesaki, 2001: *Northern Sea Route. Shortest Sea Route Linking East Asia and Europe.*
- Köberle, C., and R. Gerdes, 2003: Mechanisms Determining the Variability of Arctic Sea Ice Conditions and Export. *Journal of Climate*, **16**, 2843–2858, doi:10.1175/1520-0442(2003)016<2843:MDTVOA>2.0.CO;2.
- Kwok, R., and D. A. Rothrock, 2009: Decline in Arctic sea ice thickness from submarine and ICESat records: 1958–2008. *Geophys. Res. Lett.*, **36**, 1958 – 2008.
- Kwok, R., G. F. Cunningham, M. Wensnahan, I. Rigor, H. J. Zwally, and D. Yi, 2009: Thinning and volume loss of the Arctic Ocean sea ice cover: 2003–2008. *Journal of Geophysical Research*, **114**, C07005, doi:10.1029/2009JC005312.
- Laevastu, T., 1960: *Factors affecting the temperature of the surface layer of the sea: A study of the heat exchange between the sea and the atmosphere, the factors affecting temperature structure in the sea and its forecasting.* Helsingfors.,
- Large, W. G., and S. Pond, 1981: Open Ocean Momentum Flux Measurements in Moderate to Strong Winds. *Journal of Physical Oceanography*, **11**, 324–336, doi:http://dx.doi.org/10.1175/1520-0485(1981)011<0324:OOMFMI>2.0.CO;2.
- Leppäranta, M., 2005: *The Drift of Sea Ice (Springer Praxis Books / Geophysical Sciences).* Springer,.
- Leppäranta, M., and W. D. Hibler III, 1985: The role of plastic ice interaction in marginal ice zone dynamics. *Journal of Geophysical Research*, **90**, 11899–11909.
- Lindsay, R. W., 2010: Unified Sea Ice Thickness Climate Data Record, Polar Science Center, Applied Physics Laboratory, University of Washington,.
- Lipscomb, W. H., E. C. Hunke, W. Maslowski, and J. Jakacki, 2007: Ridging, strength, and stability in high-resolution sea ice models. *Journal of Geophysical Research*, **112**, C03S91, doi:10.1029/2005JC003355.
- Lu, Q., J. Larsen, and P. Tryde, 1989: On the role of ice interaction due to floe collisions in marginal ice zone dynamics. *Journal of Geophysical Research*, **94**, 14525, doi:10.1029/JC094iC10p14525.
- McPhee, M. G., J. H. Morison, and F. Nilsen, 2008: Revisiting heat and salt exchange at the ice-ocean interface: Ocean flux and modeling considerations. *Journal of Geophysical Research*, **113**, C06014, doi:10.1029/2007JC004383.
- Mellor, G., and A. Blumberg, 2004: Wave Breaking and Ocean Surface Layer Thermal Response. *Journal of Physical Oceanography*, **34**, 693–698, doi:10.1175/2517.1.

- Mellor, G. L., 2003a: Users guide for a three-dimensional, primitive equation, numerical ocean model (June 2003 version). *Prog. in Atmos. and Ocean. Sci*, Princeton University, 53.
- Mellor, G. L., 2003b: Users guide for a three-dimensional, primitive equation, numerical ocean model (June 2003 version). *Prog. in Atmos. and Ocean. Sci*, Princeton University,.
- Mellor, G. L., and T. Yamada, 1982: Development of a turbulence closure model for geophysical fluid problems. *Reviews of Geophysics*, **20**, 851, doi:10.1029/RG020i004p00851.
- Mellor, G. L., and A. F. Blumberg, 1985: Modeling Vertical and Horizontal Diffusivities with the Sigma Coordinate System. *Monthly Weather Review*, **113**, 1380–1383.
- Mellor, G. L., T. Ezer, and L.-Y. Oey, 1994: The Pressure Gradient Conundrum of Sigma Coordinate Ocean Models. *Journal of Atmospheric and Oceanic Technology*, **11**, 1126–1134, doi:10.1175/1520-0426(1994)011<1126:TPGCOS>2.0.CO;2.
- Mellor, G. L., S. Hakkinen, T. Ezer, and R. Patchen, 2002: A generalization of a sigma coordinate ocean model and an intercomparison of model vertical grids. 55 – 72.
- Murray, F. W., 1967: On the Computation of Saturation Vapor Pressure. *Journal of Applied Meteorology*, **6**, 203–204, doi:10.1175/1520-0450(1967)006<0203:OTCOSV>2.0.CO;2.
- Parkinson, C. L., and W. M. Washington, 1979: A large-scale numerical model of sea ice. *Journal of Geophysical Research*, **84**, 311, doi:10.1029/JC084iC01p00311.
- Proshutinsky, A. and Coauthors, 2011: Recent Advances in Arctic Ocean Studies Employing Models from the Arctic Ocean Model Intercomparison Project. *Oceanography*, **24**, 102–113, doi:10.5670/oceanog.2011.61.
- Rabe, B. and Coauthors, 2011: An assessment of Arctic Ocean freshwater content changes from the 1990s to the 2006–2008 period. *Deep Sea Research Part I: Oceanographic Research Papers*, **58**, 173–185, doi:10.1016/j.dsr.2010.12.002.
- Rampal, P., J. Weiss, and D. Marsan, 2009: Positive trend in the mean speed and deformation rate of Arctic sea ice, 1979–2007. *Journal of Geophysical Research*, **114**, C05013, doi:10.1029/2008JC005066.
- Rothrock, D. A., 1975: The energetics of the plastic deformation of pack ice by ridging. *Journal of Geophysical Research*, **80**, 4514–4519, doi:10.1029/JC080i033p04514.

- Rothrock, D. A., 2005: Arctic Ocean sea ice volume: What explains its recent depletion? *Journal of Geophysical Research*, **110**, C01002, doi:10.1029/2004JC002282.
- Sagawa, G., 2007: Development of ice dynamic model that takes account of floe collision and its validation in numerical sea ice forecast in the Sea of Okhotsk. The University of Tokyo, .
- Semtner, A. J., 1976: A Model for the Thermodynamic Growth of Sea Ice in Numerical Investigations of Climate. *Journal of Physical Oceanography*, **6**, 379–389, doi:10.1175/1520-0485(1976)006<0379:AMFTTG>2.0.CO;2.
- Shen, H. H., W. D. Hibler, and M. Leppäranta, 1986: On applying granular flow theory to a deforming broken ice field. *Acta Mechanica*, **63**, 143–160, doi:10.1007/BF01182545.
- Shimada, K., T. Kamoshida, M. Itoh, S. Nishino, E. Carmack, F. McLaughlin, S. Zimmermann, and A. Proshutinsky, 2006: Pacific Ocean inflow: Influence on catastrophic reduction of sea ice cover in the Arctic Ocean. *Geophysical Research Letters*, **33**, L08605, doi:10.1029/2005GL025624.
- Simizu, D., and K. I. Ohshima, 2006: A model simulation on the circulation in the Sea of Okhotsk and the East Sakhalin Current. *Journal of Geophysical Research*, **111**, C05016, doi:10.1029/2005JC002980.
- SMAGORINSKY, J., 1963: GENERAL CIRCULATION EXPERIMENTS WITH THE PRIMITIVE EQUATIONS. *Monthly Weather Review*, **91**, 99–164, doi:10.1175/1520-0493(1963)091<0099:GCEWTP>2.3.CO;2.
- Steele, M., R. Morley, and W. Ermold, 2001: PHC: A Global Ocean Hydrography with a High-Quality Arctic Ocean. *Journal of Climate*, **14**, 2079–2087, doi:10.1175/1520-0442(2001)014<2079:PAGOHW>2.0.CO;2.
- Steele, M., W. Ermold, and J. Zhang, 2008: Arctic Ocean surface warming trends over the past 100 years. *Geophysical Research Letters*, **35**, L02614, doi:10.1029/2007GL031651.
- Stroeve, J. C., 2005: Tracking the Arctic's shrinking ice cover: Another extreme September minimum in 2004. *Geophysical Research Letters*, **32**, L04501, doi:10.1029/2004GL021810.
- Thorndike, A. S., D. A. Rothrock, G. A. Maykut, and R. Colony, 1975: The thickness distribution of sea ice. *Journal of Geophysical Research*, **80**, 4501–4513, doi:10.1029/JC080i033p04501.

- Uchimoto, K., H. Mitsudera, N. Ebuchi, and Y. Miyazawa, 2007: Anticyclonic eddy caused by the Soya Warm Current in an Okhotsk OGCM. *Journal of Oceanography*, **63**, 379–391, doi:10.1007/s10872-007-0036-3.
- Wang, J., Q. Liu, M. Jin, M. Ikeda, and F. J. Saucier, 2005: A coupled ice-ocean model in the pan-Arctic and North Atlantic Ocean: Simulation of seasonal cycles. *Journal of oceanography*, **61**, 213–233.
- Watanabe, E., 2013: Linkages among halocline variability, shelf-basin interaction, and wind regimes in the Beaufort Sea demonstrated in pan-Arctic Ocean modeling framework. *Ocean Modelling*, **null**, doi:10.1016/j.ocemod.2012.12.010.
- Watanabe, E., and H. Hasumi, 2009: Pacific Water Transport in the Western Arctic Ocean Simulated by an Eddy-Resolving Coupled Sea Ice–Ocean Model. *Journal of Physical Oceanography*, **39**, 2194–2211, doi:10.1175/2009JPO4010.1.
- Woodgate, R. A., 2005: Monthly temperature, salinity, and transport variability of the Bering Strait through flow. *Geophysical Research Letters*, **32**, L04601, doi:10.1029/2004GL021880.
- Zhang, J., and W. D. Hibler, 1997: On an efficient numerical method for modeling sea ice dynamics. *Journal of Geophysical Research*, **102**, 8691, doi:10.1029/96JC03744.
- Zhang, J., D. A. Rothrock, and M. Steele, 1998: Warming of the Arctic Ocean by a strengthened Atlantic Inflow: Model results. *Geophysical Research Letters*, **25**, 1745–1748, doi:10.1029/98GL01299.
- Zillman, J. W., 1972: *A study of some aspects of the radiation and heat budgets of the southern hemisphere oceans*. Meteorolog. Australian Government Publishing Service,.